Leveraging oxygen redox chemistry to enhance the energy density of lithium-ion batteries

Zur Erlangung des akademischen Grades eines
DOKTORS DER NATURWISSENSCHAFTEN
(Dr. rer. nat.)

von der KIT-Fakultät für Chemie und Biowissenschaften
des Karlsruher Instituts für Technologie (KIT)
genehmigte

DISSERTATION

von
M. Sc. Hao Liu
aus Sichuan, China

KIT-Dekan: Prof. Dr. Martin Bastmeyer
Referent: Prof. Dr. Helmut Ehrenberg
Korreferent: Prof. Dr. Annie Powell
Tag der mündlichen Prüfung: 09.12.2024

Contents

Symbols and Abbreviations

LIBs	Lithium-ion batteries
XRD	X-ray powder diffraction
SXRD	Synchrotron X-ray powder diffraction
NPD	Neutron powder diffraction
PDF	Pair distribution function
SEM	Scanning electron microscopy
TEM	Transmission electron microscopy
STEM	Scanning transmission electron microscopy
HAADF	High-angle annular dark-field
EDS	Energy dispersive X-ray spectroscopy
EELS	Electron energy loss spectroscopy
ICP–OES	Inductively coupled plasma-optical emission spectroscopy
XPS	X-ray photoelectron spectroscopy
HAXPES	High-energy X-ray photoelectron spectroscopy
XAS	X-ray absorption spectroscopy
XANES	X-ray absorption near-edge structure
EXAFS	Extended X-ray absorption fine structure
SXAS	Soft X-ray absorption spectroscopy
TEY	Total electron yield
FY	Fluorescence yield
iFY	Inverse partial fluorescence yield
RIXS	Resonant inelastic X-ray scattering

MAS	Magic-angle spinning
NMR	Nuclear magnetic resonance
DEMS	Differential electrochemical mass spectroscopy
VASP	Vienna ab-initio simulation package
PBE	Perdew-Burke-Ernzerhof
DFT	Density functional theory
DOS	Density of states
C65	Carbon black
PVDF	Polyvinylidene fluoride
NMP	N-methyl-2-pyrrolidone
EC	Ethylene carbonate
EMC	Ethyl methyl carbonate
DMC	Dimethyl carbonate
GITT	Galvanostatic intermittent titration technique
E_B	Binding energy
E_K	Kinetic energy
WF	Work function

List of Figures and Tables

Abstract

Oxygen redox chemistry has driven the development of high-energy-density layered cathode materials for lithium-ion batteries, enabling additional capacity beyond traditional transition metal (TM) redox contributions. However, despite its potential, the inherent instability and irreversibility of oxygen redox processes during electrochemical reactions present significant challenges for battery performance. Moreover, the complex relationship between local structure and oxygen redox activity in layered cathodes remains insufficiently understood. To fully leverage the advantages of oxygen redox chemistry in enhancing the energy density of lithium-ion batteries, it is essential to acquire deeper insights into the underlying mechanisms and to develop effective strategies for ensuring stable oxygen redox activity. This Ph.D. thesis presents new insights into the correlation between oxygen redox activity and honeycomb superstructure units in these layered structures, thereby enhancing our comprehension of the oxygen redox mechanisms. Additionally, it demonstrates that modifications to the local honeycomb structure within layered cathodes can promote stable oxygen redox processes. The investigation of oxygen redox is organized into two sections, as outlined below:

(1) Tailoring superstructure units for enhanced oxygen redox in Li-rich layered oxides

We reveal a direct correlation between oxygen redox activity and honeycomb superstructure units in Li-rich layered oxides, specifically the fractions of $LiMn_6$ and Ni^{4+}-stabilized $LiNiMn_5$ within the TM layer. An excess of $LiNiMn_5$ impedes the extraction/insertion of lithium ions during charging/discharging, resulting in incomplete oxygen redox activity (retention of molecular O_2) at low potential (~3.3 V). We further demonstrate that lithium content adjustment is a potential solution to tailor the superstructure units. The optimized cathode, with fewer $LiNiMn_5$ units, demonstrates enhanced oxygen redox reversibility and structural stability, achieving a remarkable capacity of 231.1 mAh g^{-1} at C/10 (20 mA g^{-1}).

(2) Stable oxygen redox chemistry for high-performance lithium-ion layered oxides

We present a lithium-ion layered oxide ($Li_{1.05}Ni_{0.43}Mn_{0.52}O_2$) that achieves both high discharge capacity and stable cycle life, with capacity and energy retention of 96.3% and 93.3%, respectively, after 200 cycles at 2.5-4.55 V and a C/3 rate. These performance metrics surpass $LiNi_{0.5}Mn_{0.5}O_2$ and are comparable to the commercial $LiNi_{0.8}Co_{0.1}Mn_{0.1}O_2$ cathode. This cathode features 12.7(6) wt.% Ni-pinned honeycomb Li_2MnO_3-like domains, where Ni ions occupy Li layers, through optimized chemical composition. Advanced characterization and theoretical calculations reveal that these Ni-pinned honeycombs facilitate stable oxygen redox activity without releasing oxygen gas and enhance structural stability during extended cycling.

Zusammenfassung

Die Sauerstoff-Redoxchemie hat die Entwicklung von schichtstrukturierten Kathodenmaterialien mit hoher Energiedichte für Lithium-Ionen-Batterien vorangetrieben und ermöglicht zusätzliche Kapazitäten über die Redoxbeiträge traditioneller Übergangsmetalle (TM) hinaus. Trotz ihres Potenzials stellen die inhärente Instabilität und Irreversibilität von Sauerstoff-Redoxprozessen während elektrochemischer Reaktionen jedoch erhebliche Herausforderungen für die Batterieleistung dar. Darüber hinaus ist die komplexe Beziehung zwischen lokaler Struktur und Sauerstoff-Redoxaktivität in schichtstrukturierten Kathoden noch unzureichend verstanden. Um die Vorteile der Sauerstoff-Redoxchemie bei der Verbesserung der Energiedichte von Lithium-Ionen-Batterien voll auszuschöpfen, ist es wichtig, tiefere Einblicke in die zugrunde liegenden Mechanismen zu gewinnen und wirksame Strategien zur Sicherstellung stabiler Sauerstoff-Redox-Beiträge zu entwickeln. Diese Doktorarbeit präsentiert neue Einblicke in die Korrelation zwischen Sauerstoff-Redoxaktivität und Honigwaben-Überstruktureinheiten und verbessert damit unser Verständnis der Sauerstoff-Redoxmechanismen. Darüber hinaus zeigt sie, dass Modifikationen der lokalen Wabenstruktur innerhalb schichtstrukturierter Kathoden stabile Sauerstoff-Redoxprozesse fördern können. Die Untersuchung des Sauerstoffredox-Prozesses ist in zwei Abschnitte unterteilt, wie unten beschrieben:

(1) Optimierung von Überstruktureinheiten für verbesserte Sauerstoffredox-Beiträge in Li-reichen Schichtoxiden

Wir zeigen eine direkte Korrelation zwischen Sauerstoff-Redoxaktivität und wabenförmigen Überstruktureinheiten in Li-reichen Schichtoxiden, insbesondere den Anteilen von $LiMn_6$ und Ni^{4+}-stabilisiertem $LiNiMn_5$ innerhalb der TM-Schicht. Ein Überschuss an $LiNiMn_5$ behindert die Extraktion/Insertion von Lithiumionen während des Ladens/Entladens, was zu einer unvollständigen Sauerstoff-Redoxaktivität (Beibehalt von molekularem O_2) bei niedrigem Potential (~3.3 V) führt. Außerdem zeigen wir, dass die Anpassung des Lithiumgehalts eine mögliche Lösung ist, um die Überstruktureinheiten anzupassen. Die optimierte Kathode mit weniger $LiNiMn_5$-Einheiten weist eine verbesserte Sauerstoff-Redox-Reversibilität und strukturelle Stabilität auf und erreicht eine bemerkenswerte Kapazität von 231.1 mAh g^{-1} bei C/10 (20 mA g^{-1}).

(2) Stabile Sauerstoff-Redoxchemie für leistungsstarke Lithium-Ionen-Schichtoxide

Wir präsentieren ein Lithium-Ionen-Schichtoxid ($Li_{1.05}Ni_{0.43}Mn_{0.52}O_2$), das sowohl eine hohe Entladekapazität als auch eine stabile Zyklenlebensdauer erreicht, mit einer verbleibenden Kapazitä- und Energie von 96.3 % bzw. 93.3 % nach 200 Zyklen bei 2.5–4.55 V und einer C/3-

Rate. Diese Leistungskennzahlen übertreffen $LiNi_{0.5}Mn_{0.5}O_2$ und sind mit der kommerziellen $LiNi_{0.8}Co_{0.1}Mn_{0.1}O_2$-Kathode vergleichbar. Durch eine optimierte chemische Zusammensetzung weist diese Kathode 12.7(6) Gew.-% wabenförmige Li_2MnO_3-ähnliche Domänen auf, in denen Ni-Ionen die Li-Schichten besetzen. Fortgeschrittene CharakterisierungsTechniken und theoretische Berechnungen zeigen, dass diese Ni-stabilisierten Waben eine stabile Sauerstoff-Redox-Aktivität ohne Freisetzung von Sauerstoffgas ermöglichen und die strukturelle Stabilität während längerer Zyklen verbess

Chapter 1 Fundamentals of lithium-ion batteries

Since the Industrial Revolution, fossil fuels have been the primary energy sources driving industrial development. However, as we progress into the 21st century, the drawbacks of reliance on fossil fuels have become increasingly evident, contributing to significant environmental challenges such as haze and the greenhouse effect[1–3]. In response to the urgent need to mitigate environmental pollution, the concept of clean energy has emerged and is gradually being integrated across various sectors. The principal sources of clean energy include wind, solar, and geothermal energy. These energy sources are classified as primary because they require conversion and storage before direct utilization. Currently, the predominant method of harnessing clean energy involves converting it into electrical energy, which is then used to power industrial processes and residential electricity. When this energy is not immediately consumed, it must be converted into chemical energy for effective storage. Batteries[4], which are electrochemical devices, were first developed in the early 19th century. Since then, they have evolved into highly efficient energy storage solutions that play a crucial role in the global energy landscape.

In recent years, nickel-hydrogen batteries, lead-acid batteries, nickel-cadmium batteries, and lithium-ion batteries (LIBs) have all emerged as commercially viable technologies for energy storage. Among these, LIBs are particularly notable for their capacity to store the most electrical energy per unit mass, thereby providing the highest energy density[5–8]. Additionally, LIBs offer several advantages, including long cycle life, the absence of memory effects, and environmentally friendly characteristics. Since the introduction of the first commercial LIBs by Sony Corporation in 1990, advancements in this technology have facilitated widespread adoption across a range of portable electronic devices[9]. This progress has resulted in significant reductions in weight while enhancing battery life and overall portability. With the rapid expansion of large electric appliances, including electric vehicles, LIBs are positioned to continue evolving. The next generation of LIBs aims to achieve even higher energy densities, extend cycle life, and improve safety features, thereby addressing the increasing demand for efficient and sustainable energy solutions.

A lithium-ion battery is an electrochemical device that converts chemical energy into electrical energy. In rechargeable LIBs, this energy conversion process is reversible. The operation of LIBs involves the movement of lithium ions between the positive electrode (cathode) and the negative electrode (anode), facilitating the storage and release of energy. LIBs are composed of several essential components: the cathode, anode, electrolyte, and separator, each of which is critical to the battery's functionality. The cathode is typically made from lithium-containing transition metal oxides, such as $LiCoO_2$, and releases lithium ions during the charge process.

These ions then migrate through the electrolyte to the anode. The anode is commonly made of graphite or other carbon-based and silicon-based materials. The electrolyte is designed to enable the flow of lithium ions between the electrodes while simultaneously preventing the passage of electrons. It often consists of an organic solution containing lithium salts, such as $LiPF_6$, or a solid-state electrolyte used in next-generation batteries. Finally, the separator, fabricated from microporous polymers such as polyethylene or polypropylene, is located between the cathode and anode to prevent electronic short circuits. It allows lithium ions to pass through while blocking the transfer of electrons, thereby maintaining the battery's integrity and performance.

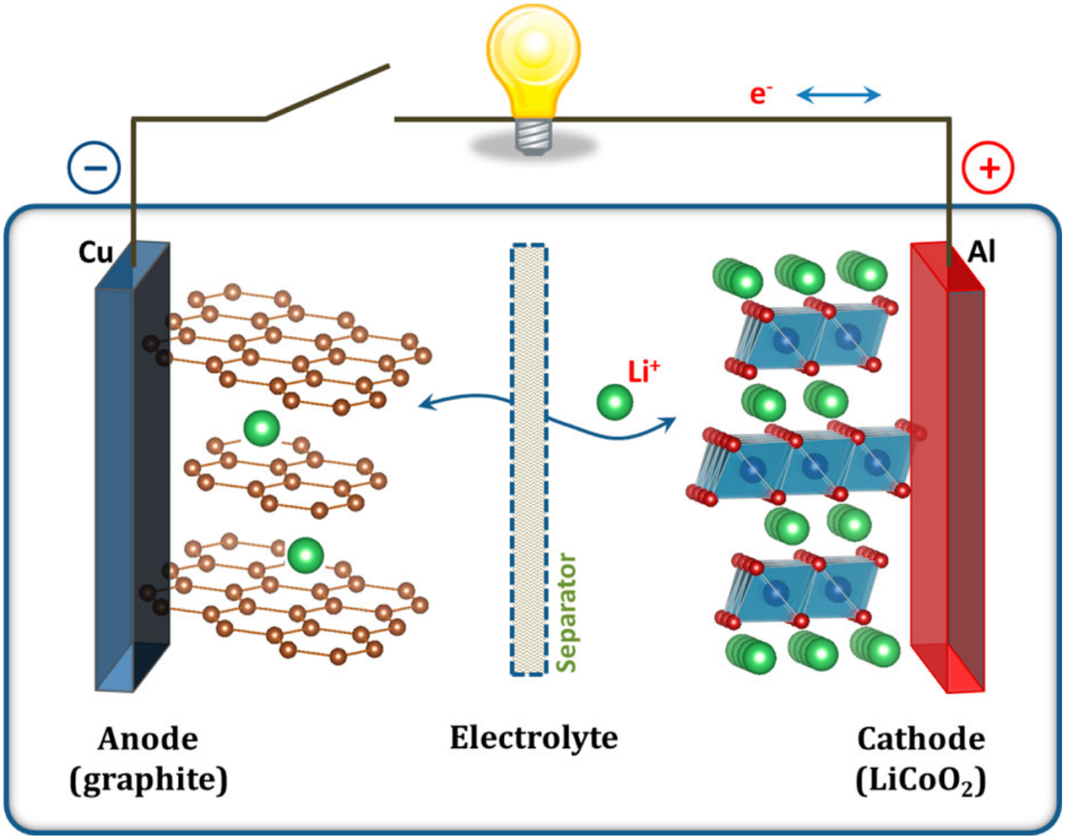

Figure 1.1 Schematic illustration of the first Li-ion battery ($LiCoO_2$/Li^+ electrolyte/graphite). Adapted from reference[10].

1.1 Operating principles of lithium-ion batteries

Figure 1.1 illustrates the fundamental operating principles of modern LIBs, specifically utilizing $LiCoO_2$ as the cathode and graphite as the anode[10]. The battery is partitioned into two distinct regions—cathode and anode—by a separator that selectively permits the flow of lithium ions while preventing the flow of electrons. During the charging process, lithium ions are extracted from the $LiCoO_2$ lattice, leading to an increase in the cathode's potential. These lithium ions then migrate through the electrolyte to the anode, where they are intercalated into the anode graphite, while electrons flow through an external circuit toward the anode. In contrast, during discharge, lithium ions are released from the graphite, travel through the electrolyte, and reinsert into the $LiCoO_2$ lattice. Concurrently, electrons flow from the anode to the cathode via the external circuit. This process continues, enabling the efficient storage and release of electrical energy.

1.2 Cathode materials for lithium-ion batteries

The cathode is a fundamental component that plays a critical role in modern LIBs systems. Lithium ions used for intercalation must be pre-stored within the lattice structure of the cathode material, meaning that the lithium storage capacity of this material directly affects the theoretical capacity limit of LIBs. Furthermore, the electrochemical performance of LIBs is primarily determined by the structure and composition of the cathode material. An ideal cathode material for LIBs should possess several key characteristics: high lithium storage capacity per unit mass, efficient ionic and electronic conductivity, high intercalation reversibility, environmental sustainability, and low production costs. Based on these criteria, the predominant cathode materials available in the market over the past three decades can be categorized into three main types based on their structural differences: olivine-type, spinel-type, and layered cathode materials. A brief overview of each of these categories is provided below.

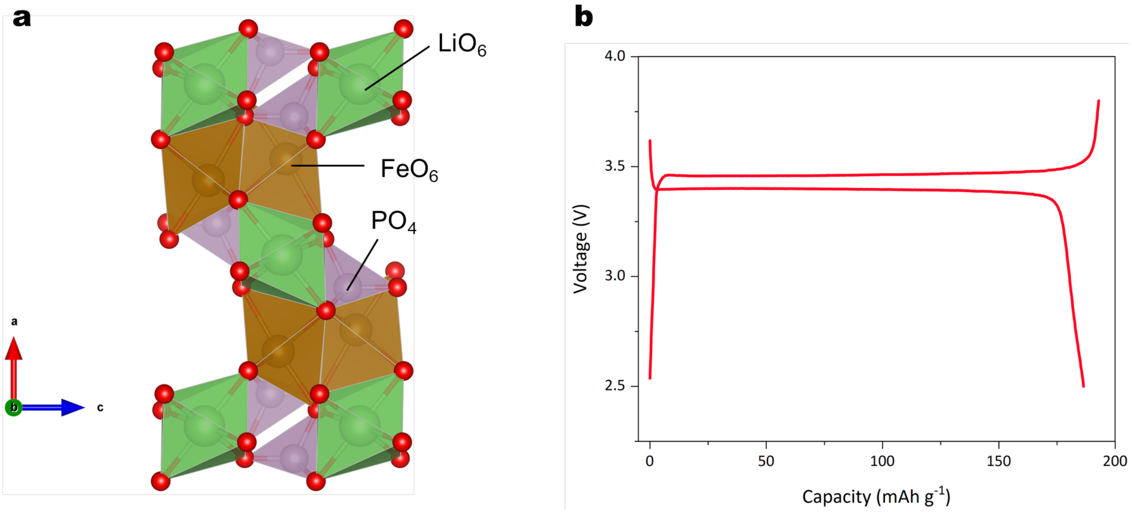

Figure 1.2 (a) The crystal structure of $LiFePO_4$. (b) The charge/discharge curves of $LiFePO_4$ in the first cycle.

1.2.1 Olivine-type cathode materials

Olivine-type polyanion cathode materials were first reported by the research team led by Goodenough[11], with lithium iron phosphate ($LiFePO_4$, LFP) serving as a prominent representative. **Figure 1.2a** depicts the crystal structure of LFP, which features an orthorhombic configuration within the *Pnma* space group. This structure is characterized by densely packed oxygen atoms arranged in a hexagonal pattern. The framework consists of LiO_6 octahedra, FeO_6 octahedra, and PO_4 tetrahedra, which together create a unique one-dimensional channel for lithium ion diffusion[12]. First-principles calculations[13] have elucidated the potential pathways for lithium-ion diffusion within this crystal structure, revealing that the lithium-ion diffusion coefficient in the [010] direction is several orders of magnitude higher than that in the [001] direction. Additionally, atomic simulations[14] indicate that the migration energy barrier for lithium ions in the [010] direction is significantly lower than that in the [001] and [101] directions. These theoretical findings have been corroborated by high-temperature neutron diffraction experiments[15]. Consequently, the one-dimensional lithium ion diffusion channel inherent in LFP contributes to a relatively slow rate of ion transport. To enhance lithium ion diffusion kinetics, material particles are often reduced to the nanoscale, effectively shortening the diffusion path for lithium ions[16].

Figure 1.2b displays the charge and discharge curve for the first cycle of LFP, indicating that its capacity is primarily derived from a voltage plateau around 3.45 V. This plateau is associated with phase transformations characterized by the coexistence of LFP and $FePO_4$. However, the distribution of these two phases and their interconversion during lithium insertion and extraction remains inadequately understood. Several models of phase transformation have been proposed, including the core-shell, shrinking core, and domino-cascade models[11,17,18]. Despite the complexity of the phase transformation processes in LFP, the lattices of LFP and $FePO_4$ exhibit good compatibility, enabling LFP to maintain its structural integrity during cycling. LFP demonstrates excellent cycling performance, exceeding 1000 cycles, along with remarkable thermal stability. Nevertheless, the primary challenges associated with LFP include its relatively low energy density and poor rate capability. To address these issues, strategies such as surface carbon coating combined with particle nanocrystallization can enhance both ionic and electronic conductivity. Furthermore, various olivine-type cathode materials with different compositions can be synthesized through partial substitution of the Fe element, which serves to increase the redox potential and improve energy density[19,20].

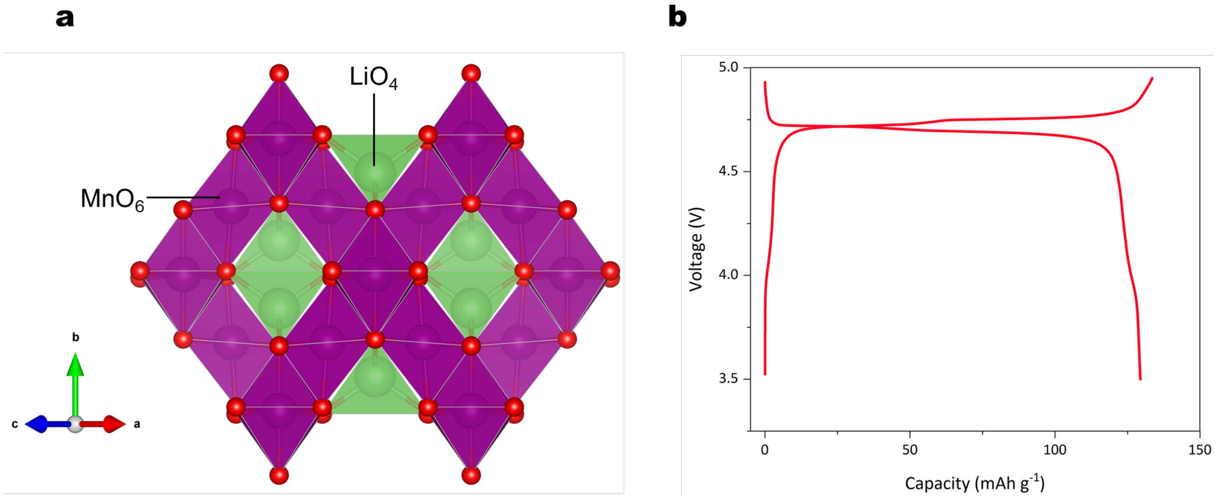

Figure 1.3 (a) The crystal structure of $LiMn_2O_4$*. (b) The charge/discharge curves of* $LiNi_{0.5}Mn_{1.5}O_4$ *in the first cycle.*

1.2.2 Spinel-type cathode materials

Spinel-type cathode materials, first introduced by Thackeray[21] et al., are represented by the chemical formula $LiMn_2O_4$ (LMO). **Figure 1.3a** depicts the crystal structure of the LMO cathode, which belongs to the *Fd-3m* space group. In this structure, lithium occupies the tetrahedral 8a sites, manganese resides in the octahedral 16d sites, and oxygen is located in the 32e sites. The spinel structure exhibits a high diffusion coefficient for lithium ions, which is generally attributed to its three-dimensional distribution network[22,23]. Given the abundance of manganese, its environmental friendliness, and the ease of material preparation, LMO is considered to have significant application potential. However, a critical issue with LMO is the presence of Mn^{3+} ions (with the electron configuration $t_{2g}^3e_g^1$), which can induce Jahn-Teller distortions in the lattice, leading to instability in the crystal structure during battery operation[24–26]. Additionally, Mn^{3+} ions are susceptible to disproportionation reactions when in contact with hydrofluoric acid (HF) present in the electrolyte, resulting in the formation of Mn^{2+} and Mn^{4+} ions[27,28]. This process leads to an irreversible loss of manganese and a rapid degradation of battery capacity.

To mitigate these challenges, the surface chemistry of LMO particles can be enhanced through coating techniques and the optimization of electrolyte composition. Furthermore, partially replacing manganese with alternative elements can help regulate the oxidation states of manganese and reduce the concentration of Mn^{3+}, thereby increasing the stability of the crystal structure. The introduction of foreign elements can modulate the redox potential of LMO, resulting in an increased operating voltage. A series of high-voltage spinel-type cathode materials has been developed with the general formula $LiM_{0.5-x}Mn_{1.5+x}O_4$ (where M represents elements such as Al, Ti, Cr, Fe, Co, Ni, Cu, etc.)[29–31]. Among these materials, lithium nickel manganese oxide ($LiNi_{0.5}Mn_{1.5}O_4$, LNMO) is regarded as the most promising high-voltage spinel cathode material. LNMO can be further categorized into ordered and disordered spinel structures, depending on the arrangement of Ni and Mn in the octahedral positions[29,32]. The distinct cation distributions within these structures significantly influence their electrochemical properties. Ordered LNMO typically exhibits a voltage plateau around 4.7 V during the charge-discharge process, which is accompanied by a structural phase transformation (see **Figure 1.3b**). In contrast, disordered LNMO exhibits charge and discharge curves resembling those of a solid solution mechanism around 4.0 V. This lower voltage feature is attributed to the oxidation and reduction of small amounts of Mn^{3+} ions, which may originate from localized nickel-rich impurity domains within the disordered structure. These impurities disrupt the theoretical 1:3 ratio of Ni to Mn, leading to the reduction of some Mn^{4+} to Mn^{3+} ions[33,34]. While ordered LNMO generally exhibits higher energy density, some studies indicate that their kinetic performance during charge and discharge may be inferior to that of disordered LNMO[35]. Therefore, it is essential to adjust the application of these cathode materials based on specific operational scenarios. Overall, spinel-type cathode materials merit further research and exploration due to their significant potential in the development of high-power, high-energy-density LIBs.

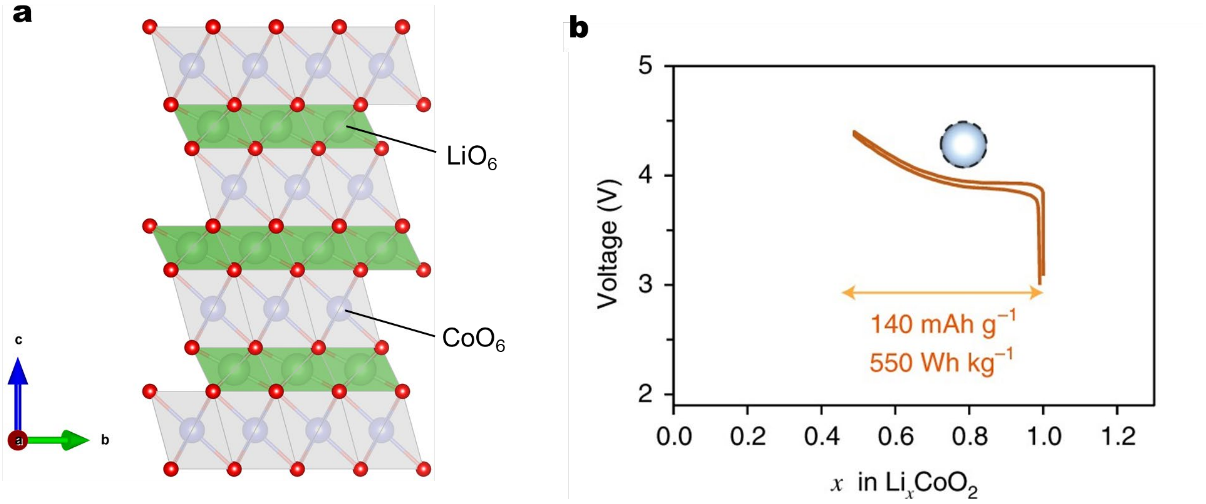

Figure 1.4 (a) The crystal structure of $LiCoO_2$. (b) The charge/discharge curves of $LiCoO_2$. Adapted from reference[36].

1.2.3 Layered stoichiometric cathode materials

The first layered cathode material, lithium cobalt oxide ($LiCoO_2$, LCO), was reported by Goodenough[37] in 1980, marking a significant milestone in the development of LIBs. The introduction of LCO revolutionized the design of LIBs and facilitated the creation of the prototype for modern batteries. More importantly, it served as the cathode material for the first commercial lithium-ion battery, launched by Sony Corporation of Japan in 1991, thereby initiating the ongoing era of LIBs. The crystal structure of LCO is depicted in **Figure 1.4a**. LCO crystallizes in the *R-3m* space group, with lithium and cobalt occupying specific lattice sites (3b and 3a respectively), while oxygen atoms are located at site 6c. This crystal structure features alternating layers of LiO_6 and CoO_6 octahedra, creating a layered arrangement that facilitates two-dimensional lithium-ion diffusion within the lithium layers. As a result, LCO exhibits favourable lithium-ion diffusion kinetics. LCO has a high theoretical capacity of 274 mAh g^{-1}; however, it experiences rapid capacity decay when lithium depletion exceeds 0.5 ions per formula unit. Beyond this threshold, the crystal structure becomes unstable, leading to distortion or collapse, which limits the practical discharge capacity to approximately 140 mAh g^{-1} (see **Figure 1.4b**). A fundamental cause of this instability is the overlap between the oxygen ion band and the Co^{3+}/Co^{4+} energy levels within the structural framework. Deep charging and discharging cycles result in the oxidation and reduction of lattice oxygen, compromising the stability of the framework[38–40].

In recent years, various modifications[41,42] to enhance the performance of high-voltage LCO have been proposed, leading to significant advancements. However, despite its widespread adoption as a commercial lithium-ion battery cathode material, LCO has several drawbacks, including the toxicity of Co, its environmental impact, and its relatively low abundance in the Earth's crust. The urgent development of alternative layered oxide cathode materials that incorporate other elements is necessary to enhance battery performance. By integrating Ni, Mn, and Al elements, ternary layered oxide cathode materials, such as $LiNi_xCo_yMn_{1-x-y}O_2$ and $LiNi_xCo_yAl_{1-x-y}O_2$, have been successfully developed[43,44]. In these materials, Ni plays a critical role in providing high specific discharge capacity, while Co enhances ionic and electronic conductivity and mitigates cation mixing. Meanwhile, Mn and Al, which are less reactive, contribute to the stabilization of the crystal structure during deep delithiation. The varying proportions of Ni, Co, Mn, and Al in these materials result in different electrochemical properties. Generally, within the standard charging cut-off voltage of 4.3 V, an increase in Ni content leads to a greater number of electrochemically active Ni redox pairs, thereby facilitating higher discharge capacities[45]. However, the oxidation of Ni^{2+} to Ni^{3+} during the synthesis of Ni-rich materials poses significant challenges. To promote this oxidation process, a highly purified oxygen atmosphere must be introduced during synthesis, which consequently increases production costs[46]. Despite these challenges, Ni-rich layered oxide cathode materials are regarded as the most promising power source for large electronic devices, such as electric vehicles.

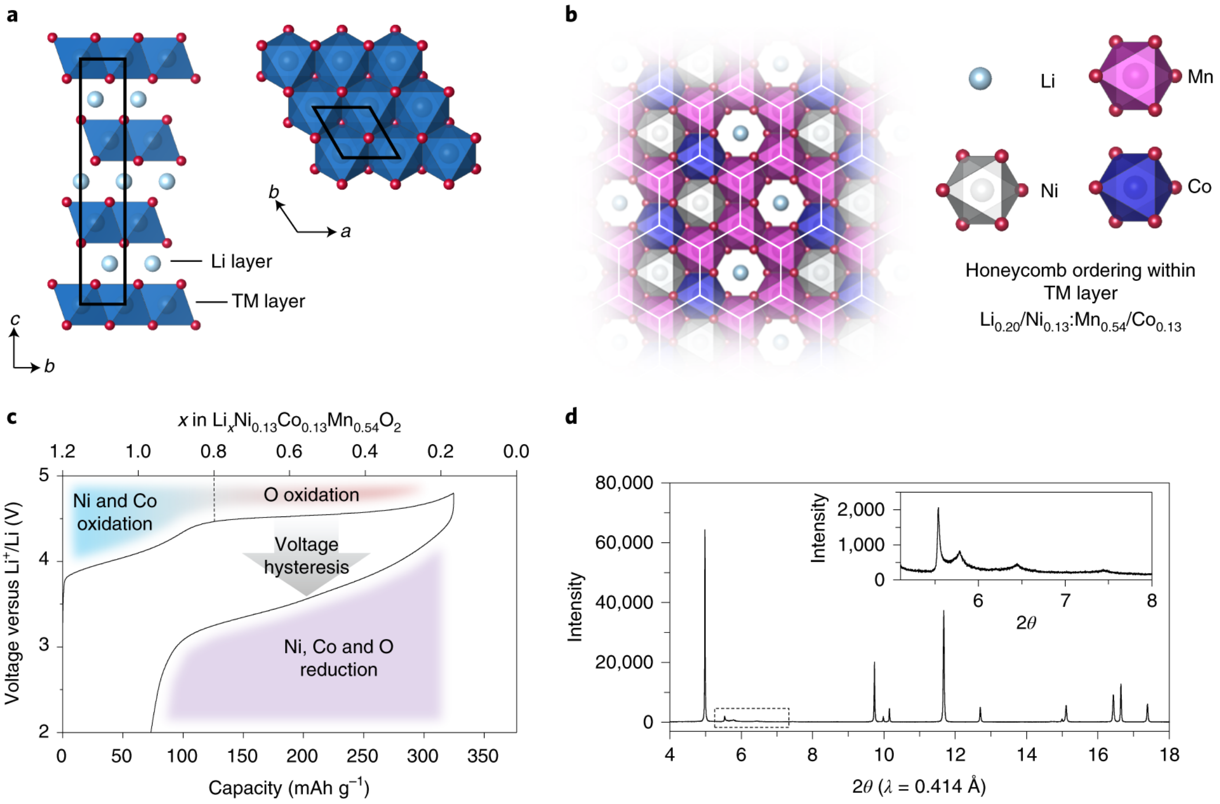

Figure 1.5 (a) $Li_{1.2}Ni_{0.13}Co_{0.13}Mn_{0.54}O_2$ with a layered R-3m crystal structure. (b) In-plane ordering of Li/TM within the TM layer gives rise to a honeycomb arrangement. (c) First charge–discharge cycle for $Li_{1.2}Ni_{0.13}Co_{0.13}Mn_{0.54}O_2$. (d) Synchrotron PXRD data showing diffraction peaks arising from honeycomb ordering (inset). Adapted from reference[47].

1.2.4 Layered lithium-rich cathode materials

Lithium-rich (Li-rich) cathode materials are classified as non-stoichiometric layered oxides, where the designation "Li-rich" indicates a lithium-to-transition-metal ion ratio (Li/TM) greater than 1. The development of Li-rich cathode materials originated from research on layered cathodes. In the early 1990s, the impressive performance of LCO garnered significant attention, promoting the exploration of layered cathode materials. However, due to various drawbacks associated with the use of cobalt, researchers sought alternatives, leading to the exploration of manganese as a viable substitute to create high-performance lithium manganese oxide ($LiMnO_2$) cathodes. In this context, Thackeray[48] et al. utilized Li_2MnO_3 as the initial material and attempted to synthesize $LiMnO_2$ by chemically leaching a portion of Li_2O with acid, ultimately producing the electrochemically active layered cathode material $Li_{1.09}Mn_{0.91}O_2$. However, this material exhibited a charge voltage limited to 4.3 V, hindering its distinction from other layered cathodes. It was not until 2001 that Dahn[49] successfully increased the charge cut-off voltage to 4.6 V in the $Li[Ni_xLi_{(1/3-2x/3)}Mn_{(2/3-x/3)}]O_2$ layered cathode material. As the understanding of Li-rich cathode materials has advanced, it has become clear that these materials differ significantly from conventional stoichiometric layered oxides such as LCO, justifying their classification as a distinct cathode material system.

The crystal structure of a typical Li-rich cathode material is illustrated in **Figure 1.5a**. Similar to conventional layered oxide materials, oxygen atoms are densely packed in a cubic arrangement. However, a key distinction from traditional layered oxides is the presence of additional lithium ions in the transition metal layer. The arrangement of lithium within this layer is not random or disordered. Numata, Dahn, and their colleagues[49,50] were the first to observe superlattice diffraction peaks (**Figure 1.5d**) in the X-ray diffraction (XRD) patterns of Li-rich cathode materials. This phenomenon was attributed to the formation of a short-range ordered structure known as $LiTM_6$ within the transition metal layers (see **Figure 1.5b**). The ordered arrangement of $LiTM_6$ reduces the symmetry of the crystal structure, leading to the reclassification of the unit cell containing this structure into the monoclinic system (space group *C2/m*), while the rest of the material corresponds to the traditional layered oxide structure in the *R-3m* space group. The structural composition of these layered Li-rich oxides is a subject of ongoing debate, particularly regarding whether they should be classified as two-phase composites with the chemical formula $x\mathrm{Li_2MnO_3}\cdot(1-x)\mathrm{LiTMO_2}$ or as single-phase solid solutions represented by the formula $\mathrm{Li[Li}_x\mathrm{TM}_{1-x}\mathrm{]O_2}$[51,52].

In contrast to conventional layered cathodes, Li-rich layered oxides can achieve a high discharge capacity of up to 250 mAh g^{-1} at the voltage range of 2.0-4.8 V (**Figure 1.5c**). Early hypotheses, such as further oxidation of Mn^{4+} to Mn^{7+} mechanism[53], have been proposed to explain the high capacity of Li-rich cathodes. Subsequent theories have advanced our understanding by suggesting that processes such as oxygen release and recombination, interfacial oxygen redox reactions, and reversible redox processes in the bulk phase, accompanied by the release of Li_2O, play integral roles alongside the activation of MnO_2[54–57]. In 2013, experiments conducted by Tarascon, Delmas, and others[58,59] demonstrated that the reversible redox activity of oxygen in the bulk phase of layered Li-rich cathode materials contributes additional capacity and elucidates the underlying charge compensation mechanism. Subsequently, in 2016, Ceder[60] et al. employed theoretical calculations to propose that the anion redox behaviour in Li-rich cathode materials originates from oxygen atoms in a lone pair state, with the Li-O-Li configuration serving as the structural basis for this electronic state. This theory not only clarifies the source of oxygen activity within Li-rich cathode materials but also redefines these materials in the context of battery technology. The details of this theory regarding oxygen redox contributions will be discussed in the following section of this thesis. However, the inherent instability associated with oxygen redox behaviour can result in significant voltage hysteresis, voltage decay, and oxygen gas release, posing substantial challenges for commercial applications[61]. While obstacles remain for the widespread adoption of Li-rich cathode materials, ongoing research offers optimism that these issues can be effectively addressed, paving the way for their successful integration in high-energy-density LIBs in the near future.

1.3 Band structures of oxygen redox activity

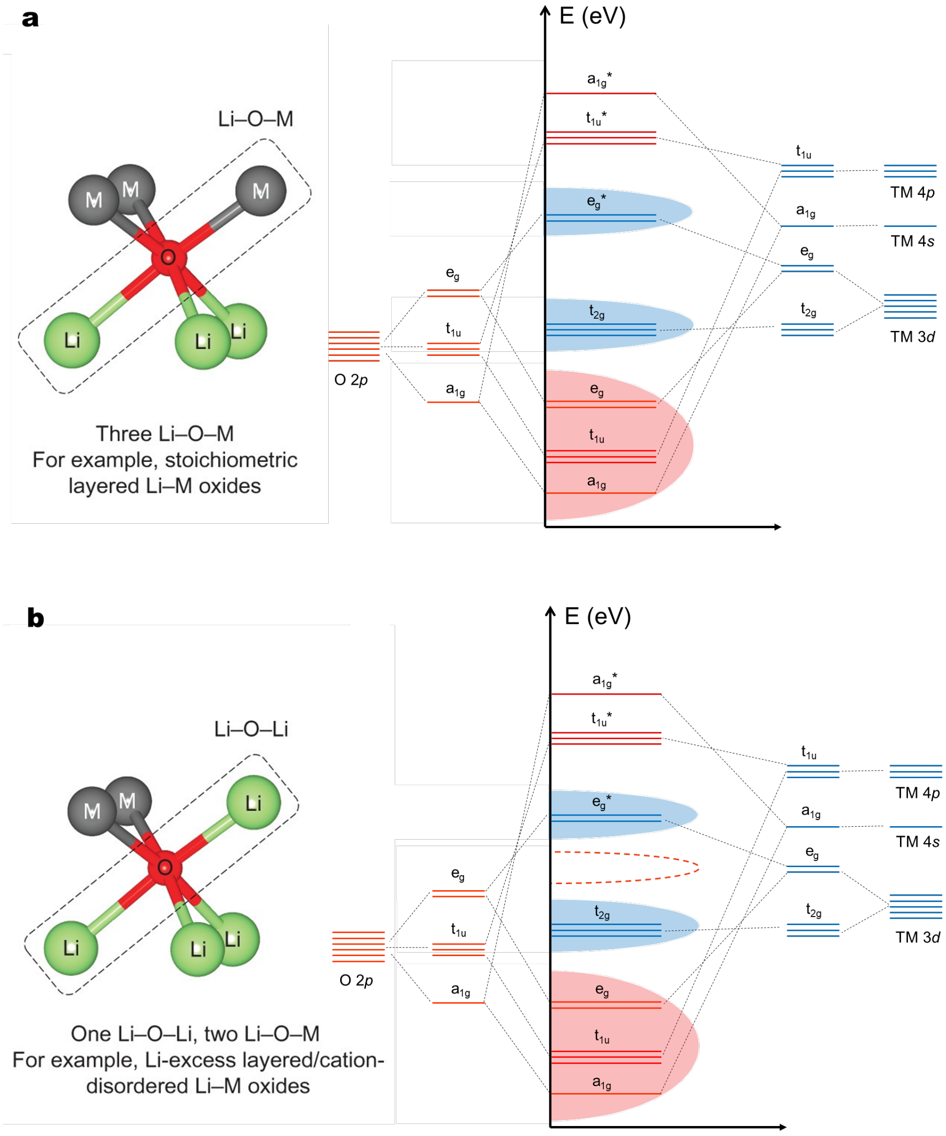

Figure 1.6 (a) Local atomic coordination around oxygen consisting of three Li–O–M configurations in stoichiometric layered cathodes. Corresponding band structures between the TM and O orbitals in a typical TMO_6 coordination. (b) Local atomic coordination around oxygen with one Li–O–Li and two Li–O–M configurations in Li-rich cathodes. Corresponding band structures between the TM and O orbitals in a typical TMO_6 coordination. Adapted from reference[60].

While significant understanding has been developed regarding the redox behaviour of TM ions in battery materials, relatively little is known about oxygen redox processes within these systems. This gap in knowledge can be attributed to the absence of a rigorous definition of oxygen redox in the literature until recently. The fundamental principles underlying redox processes in battery materials are closely related to their band structures[60,62–65]. In layered lithium-stoichiometric transition metal oxides, such as LCO, each oxygen ion is coordinated with three TM ions and three lithium ions (as illustrated in **Figure 1.6a**, left panel). This configuration facilitates the hybridization of each oxygen 2p orbital with the d/s/p orbitals of the TM in a linear Li–O–TM arrangement. From an electronic structure perspective, as shown in **Figure 1.6a** (right panel), the 3d orbitals of 3d TM ions are split into doubly degenerate e_g orbitals (comprising d_{x2-y2} and d_{z2}) and triply degenerate t_{2g} orbitals (including d_{xy}, d_{xz}, and d_{yz}). The e_g orbitals directly overlap with the oxygen 2p orbitals along the TM-O bond direction, resulting in the formation of an antibonding e_g* band at a higher energy level and a bonding e_g band at a relatively lower energy level. In contrast, t_{2g} orbitals typically form non-bonding states due to the lack of direct overlap with the 2p orbitals. Furthermore, the overlap between the TM 4s and O 2p orbitals generates bonding a_{1g} and antibonding a_{1g}* states, while the overlap between the TM 4p and O 2p orbitals produces bonding t_{1u} and antibonding t_{1u}* states. Due to the lower energy level of the oxygen 2p orbitals relative to the majority of TM orbitals, the bonding molecular orbitals, including t_{1u}, a_{1g}, and e_g states, predominantly exhibit oxygen 2p character, whereas the antibonding molecular orbital states—including t_{2g}, e_g*, a_{1g}*, and t_{1u}*—are primarily governed by TM orbitals.

In a typical delithiation redox process, the occupied states below the Fermi level donate a specific number of electrons, corresponding to the number of lithium ions extracted. In most lithium transition metal oxides ($LiTMO_2$), the Fermi level typically resides at antibonding e_g* or non-bonding t_{2g} states, which are characterized predominantly by TM 3d orbitals. This arrangement allows TM 3d electrons to effectively participate in the oxidation of TM ions, thereby operating as a cationic redox center. This type of redox process is commonly referred to as cation redox. For instance, in LFP, electrons are removed from the Fe t_{2g} states, resulting in the oxidation of Fe^{2+} ($t_{2g}^6 e_g^0$) to Fe^{3+} ($t_{2g}^5 e_g^0$). The redox mechanisms in Li-rich cathodes differ significantly from those in lithium-stoichiometric transition metal oxides. In Li-rich materials, some lithium ions replace TM ions within the transition metal layers, leading to the emergence of new configurations, namely the Li–O–Li configuration, in addition to the conventional Li–O–TM configuration (see **Figure 1.6b**, left panel). This unique Li–O–Li configuration gives rise to the formation of non-bonding ligand p states that are positioned at a higher energy level than those in $LiTMO_2$ (as indicated by the dashed red ellipse between the t_{2g} and e_g* bands in **Figure 1.6b**, right panel). Consequently, during the charging process, electrons are extracted not only from the hybridized TM 3d–O 2p states but also from O 2p states. Given that the O 2p states are at a lower energy level than the TM redox states, oxygen redox typically occurs over a high voltage plateau (~4.5 V) during the first charge cycle. This phenomenon makes oxygen redox particularly advantageous for Li-rich materials, as it provides additional redox capacity at high voltages, resulting in a substantial increase in energy density.

1.4 Motivation and objectives of the thesis

The increasing demand for high-performance energy storage systems—driven by the rapid growth of electric vehicles and renewable energy technologies—necessitates the development of advanced high-energy-density LIBs. To achieve significant capacity improvements, lithium-ion layered oxides that utilize oxygen redox chemistry have garnered considerable attention. However, a comprehensive understanding of the relationship between oxygen redox activity and the chemical composition and structure of lithium-ion layered cathodes remains elusive. Moreover, unlike the stable and reversible TM redox contributions, oxygen redox processes are often unstable and irreversible, which negatively impacts battery performance. Designing and producing large-scale commercial modifications to achieve stable oxygen redox activity in lithium-ion layered oxides has therefore become a critical challenge. This thesis focuses on addressing these issues related to oxygen redox activity in lithium-ion layered oxides.

(1) We conduct a comprehensive investigation of cobalt-free Li-rich layered oxides with varying nickel contents through advanced techniques such as synchrotron X-ray powder diffraction (SXRD), pair distribution function (PDF) analysis, transmission electron microscopy (TEM), X-ray absorption spectroscopy (XAS), nuclear magnetic resonance (NMR) spectroscopy, soft X-ray absorption spectroscopy (SXAS), resonant inelastic X-ray scattering (RIXS), and density function theory (DFT) calculations. By integrating these methods with electrochemical investigations, we identify the types of honeycomb superstructure units within the TM layers and establish a direct correlation between oxygen redox activity and the ratio of these superstructure units. Furthermore, we propose a practical solution to enhance electrochemical performance with reversible oxygen redox activity by tailoring the honeycomb superstructure in Li-rich layered oxides.

(2) We design a high-performance lithium-ion layered oxide that achieves stable oxygen redox activity through an optimized chemical composition. Advanced characterization techniques, including SXRD, neutron powder diffraction (NPD), NMR, High-angle annular dark-field scanning TEM (HAADF–STEM), SXAS, RIXS, and DFT calculations, confirm the unique local honeycomb structure that enables stable oxygen redox activity without the release of oxygen gas. This innovation results in high-energy-density LIBs that significantly outperform low-Ni counterparts while demonstrating performance metrics comparable to the commercially available high-Ni NCM811 cathode.

Chapter 2 Characterization

Accurate characterization of the redox behaviour of oxygen ions in LIBs cathode materials is fundamental to advancing our understanding of intrinsic anion redox mechanisms. Probing the electronic structure of heavy transition metals such as Ni and Co using conventional techniques is generally more straightforward and established than that of light elements. Oxygen ions, in particular, pose significant challenges for investigation due to their ubiquitous presence in the environment, complicating efforts to target the specific oxygen ions within the material of interest. In this section, we will focus on several commonly used characterization techniques for examining oxygen redox processes in lithium-ion cathode materials.

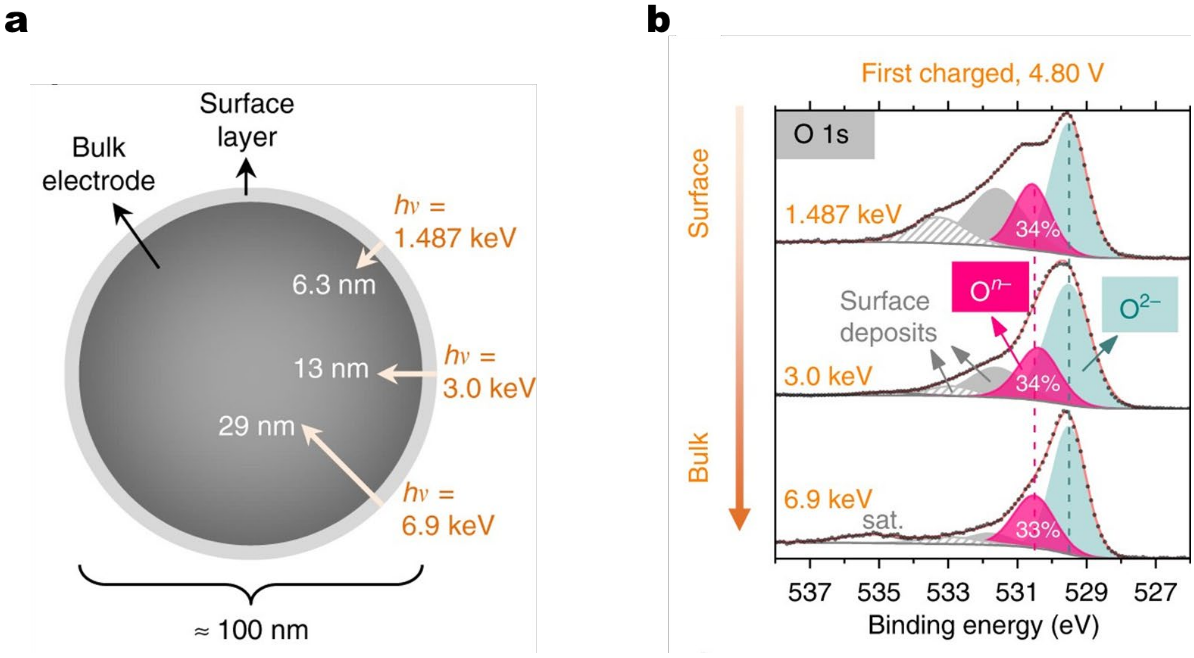

Figure 2.1 (a) Schematic view of XPS probe depths estimated for the O 1s core peak at increasing photon energies from hv = 1.487 to 3.0 and 6.9 keV. (b) The effect of probe depth on the O 1s spectra first charged at 4.80 V. Adapted from reference[66]*.*

2.1 X-ray Photoelectron Spectroscopy (XPS)

X-ray photoelectron spectroscopy (XPS) is a prominent surface analysis technique primarily used to investigate the elemental composition, chemical state, and electronic structure of materials. The foundational principle of XPS is based on the photoelectric effect. In a high vacuum environment, when the surface of a sample is irradiated with high-energy X-rays, core-level electrons (such as those in the 1s orbital) absorb sufficient energy to overcome their binding energy (E_B). This process leads to their excitation and eventual escape from the atom. The process begins with the interaction of incident X-rays, commonly generated from sources such as Al Kα (1486.6 eV) and Mg Kα (1253.6 eV), with the surface atoms of the sample. This interaction causes core-level electrons to absorb energy, resulting in their transition to unoccupied high-energy states and the formation of excited states. Subsequently, these excited electrons escape from the sample into the vacuum due to energy loss. By utilizing a highly sensitive electron energy analyser, the kinetic energy of the emitted electrons can be measured, allowing for the calculation of their binding energy using the equation: $E_B = hv - E_K - \mathrm{WF}$, where hv represents the photon energy, E_K is the measured kinetic energy, and WF is the spectrometer work function[67]. The electron binding energy E_B is characteristically distinct for atoms in different electronic shells and is influenced by the chemical environment surrounding the atom. Specifically, changes in the chemical state can lead to shifts in the energies of emitted photoelectrons. A higher electron density around an atom results in an increased kinetic energy of the emitted photoelectrons, leading to a correspondingly lower chemical shift in the E_B peaks observed in the spectrum. XPS is particularly well-suited for analysing thin films, coatings, and surface treatments due to the limited escape depth of emitted photoelectrons, which typically ranges from 0 to 10 nm. However, this limitation confines XPS to the evaluation of electronic and chemical states of surface species only.

XPS has been utilized since the 1990s to monitor changes in the electronic structure of $Li_xCo_{1-x}O$ as the value of x increases[68]; however, these early measurements provided limited insights. Dahéron[69] et al. investigated the electronic structure changes of Li_xCoO_2 during lithium deintercalation using XPS. They proposed that the observed variations in the O 1s spectrum primarily reflected the presence of oxygen-containing species at the electrode/electrolyte interface during electrochemical reactions, rather than changes within the Li_xCoO_2 structure itself. More recently, Tarascon[66] et al. elucidated the complete mechanisms of anionic and cationic charge compensation in Li-rich layered cathodes by employing bulk-sensitive synchrotron-based spectroscopies. In contrast to conventional lab XPS, which uses an incident photon energy of 1.487 keV, high-energy synchrotron X-rays utilized in high-energy X-ray photoelectron spectroscopy (HAXPES) have energies of 3.0 keV and 6.9 keV. This increased photon energy enhances the detection depth of HAXPES to approximately 13 nm at 3.0 keV and 29 nm at 6.9 keV, as illustrated in **Figure 2.1**. In their study, the primary particles were relatively small (approximately 100 nm), allowing the researchers to infer that the detected signals at the highest photon energy of 6.9 keV corresponded to bulk information. By integrating this data with lower photon energy measurements, they concluded that comprehensive insights regarding both the surface and bulk characteristics of Li-rich cathodes during electrochemical reactions could be obtained. However, for particles exceeding 100 nm, tracking bulk information remains a significant challenge.

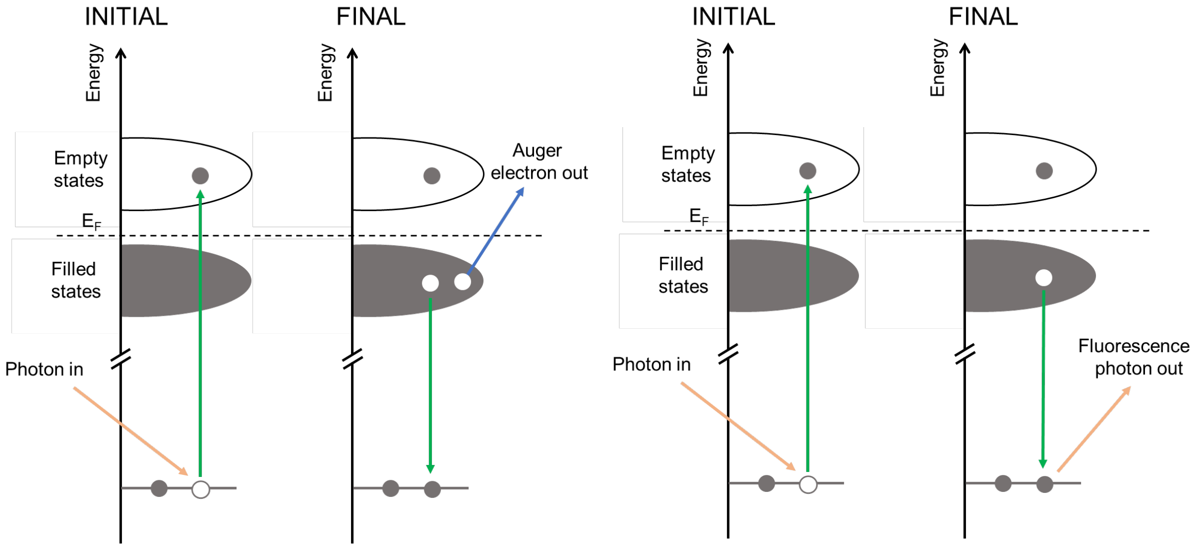

Figure 2.2 Schematic diagram of the TEY and FY detection modes in SXAS.

2.2 Soft X-ray Absorption Spectroscopy (SXAS)

Soft X-ray absorption spectroscopy (SXAS) is a crucial spectroscopic technique employed to investigate the electronic structure, chemical state, and elemental composition of materials[70,71]. The fundamental principle of SXAS is based on the interaction between photons and matter. By utilizing X-rays with adjustable energy, core-level electrons in the sample, such as those in the 1s or 2p orbitals, can be excited to unoccupied states. This process places the system in an unstable excited state, resulting in holes in the core-level orbitals, with the excited electrons residing in unoccupied states (see **Figure 2.2**, Initial State). During the subsequent de-excitation (decay) process, energy is released in two primary ways: through the emission of Auger electrons or the emission of fluorescent photons (**Figure 2.2**). In practical measurements, SXAS employs two common detection modes. The first mode, known as the photon-in-electron-out total electron yield (TEY) mode, involves the emission of Auger electrons when other electrons fill the holes in the core-level orbitals. To maintain electrical neutrality, a compensation current is generated on the sample surface, allowing TEY to characterize light absorption by detecting this current. The typical detection depth in TEY mode is around 10 nm, making it particularly effective for analysing electronic states at the sample's surface. The second mode is the photon-in-photon-out total fluorescence yield (FY) mode. In this mode, electrons in the occupied states fill the core holes by releasing energy in the form of fluorescent photons. These photons generally possess lower energy and carry structural information about the sample. The detection depth in FY mode typically ranges from 100 to 200 nm, which facilitates the characterization of electronic states in the bulk material. It is important to note that the decay process operates through both mechanisms—Auger electron emission and photon emission—simultaneously. Within the soft X-ray energy range, the probability of de-excitation via Auger electron emission exceeds 99%, while the probability of photon emission is approximately 1%. During spectral measurements, both TEY and FY spectra can be obtained concurrently, enabling comparative analysis of the electronic states present in both the surface and bulk regions of the material.

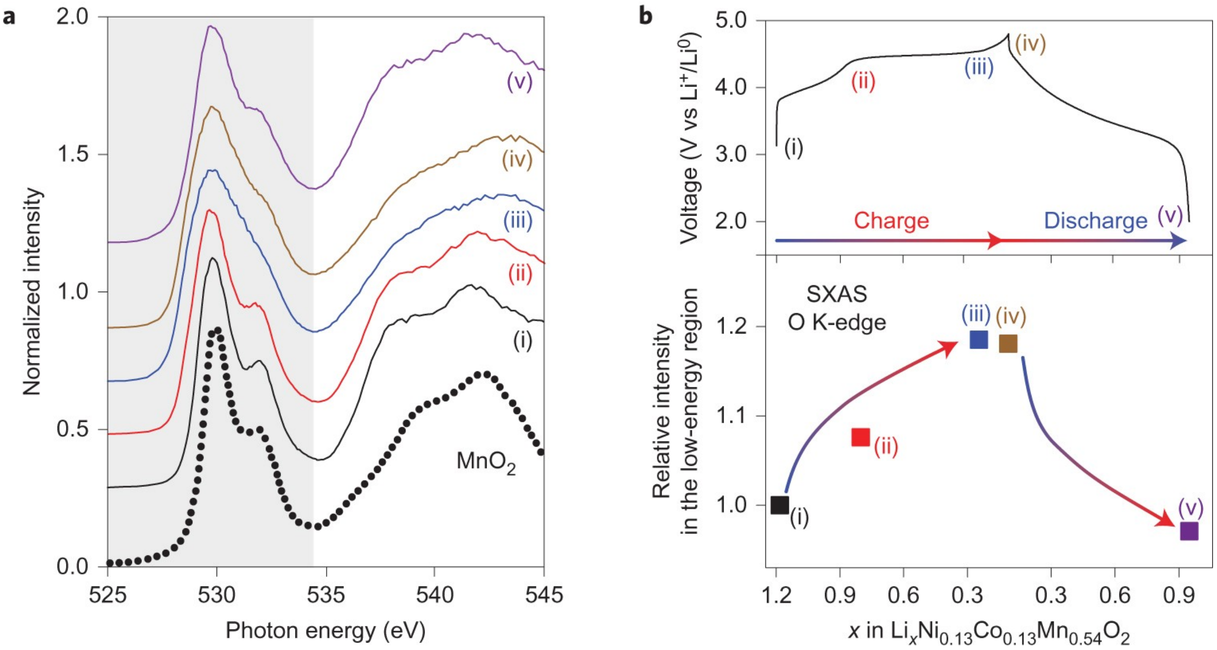

Figure 2.3 (a) SXAS spectra collected at different states of charge in FY mode, and corresponding to the points in the voltage profile in (b). Variation of the integrated intensity in the low-energy region (shaded region in a) for O K-edge SXAS (b, bottom) at the points shown in the load curve immediately above. Adapted from reference[72].

Most previous studies have employed O K-edge SXAS measurements to investigate the electronic structure of oxygen ions during electrochemical reactions in various cathodes, including $LiCoO_2$[73,74], $LiNiO_2$[75,76], $LiCo_{1/3}Ni_{1/3}Mn_{1/3}O_2$[77], and $xLi_2MnO_3\cdot(1-x)LiTMO_2$[78] cathodes. The pre-edge region of the O K-edge SXAS spectrum corresponds to the transition of O 1s electrons to holes formed from the hybridization of O 2p and TM 3d orbitals. Consequently, the intensity of this peak is correlated with the number of electron holes generated by the covalence of the TM–O bond, providing insight into the electronic states of the oxygen ions. Typically, an increase in intensity at the O K-edge, without concomitant changes at the TM L-edge or TM K-edge, suggests the occurrence of oxygen redox activity. If the state has any 3d character, it should be detectable at the TM L-edge, which probes electric dipole-allowed transitions from 2p to 3d orbitals. Peter[72] et al. utilized SXAS to identify the hole states of oxygen ions during the charging process in the classical Li-rich cathode $Li_{1.2}Ni_{0.13}Co_{0.13}Mn_{0.54}O_2$. As shown in **Figure 2.3**, below 4.5 V (spectrum ii), the spectra exhibit similar features. However, by comparing the integrated intensity of the SXAS (indicated by the shaded region) for spectra i and ii, the difference reveals additional unoccupied states associated with the Ni^{4+} e_g and Co^{4+} t_{2g} orbitals.

Upon charging to stage iii, there is a notable increase in the density of unoccupied states, with the difference in integrated intensities between spectra iii and ii indicating an additional density of states of approximately 10%. This increase cannot be attributed to further unoccupied states among Co, Ni, or Mn, as their respective K-edge XANES spectra show no evidence of oxidation beyond the +4 state. Therefore, the additional unoccupied states are primarily linked to holes in the O 2p orbitals. Additionally, an increase in intensity is observed above the absorption onset around 531 eV during charging, as noted in nearly all layered Li-rich cathodes[79–81]. This increase has also been attributed to oxidized lattice oxygen in recent studies. However, it is crucial to consider the corresponding changes in TM ions when using SXAS to determine the electronic structure of oxygen ions. Thus, O K-edge SXAS may not provide the most definitive or direct characterization for elucidating oxygen redox processes.

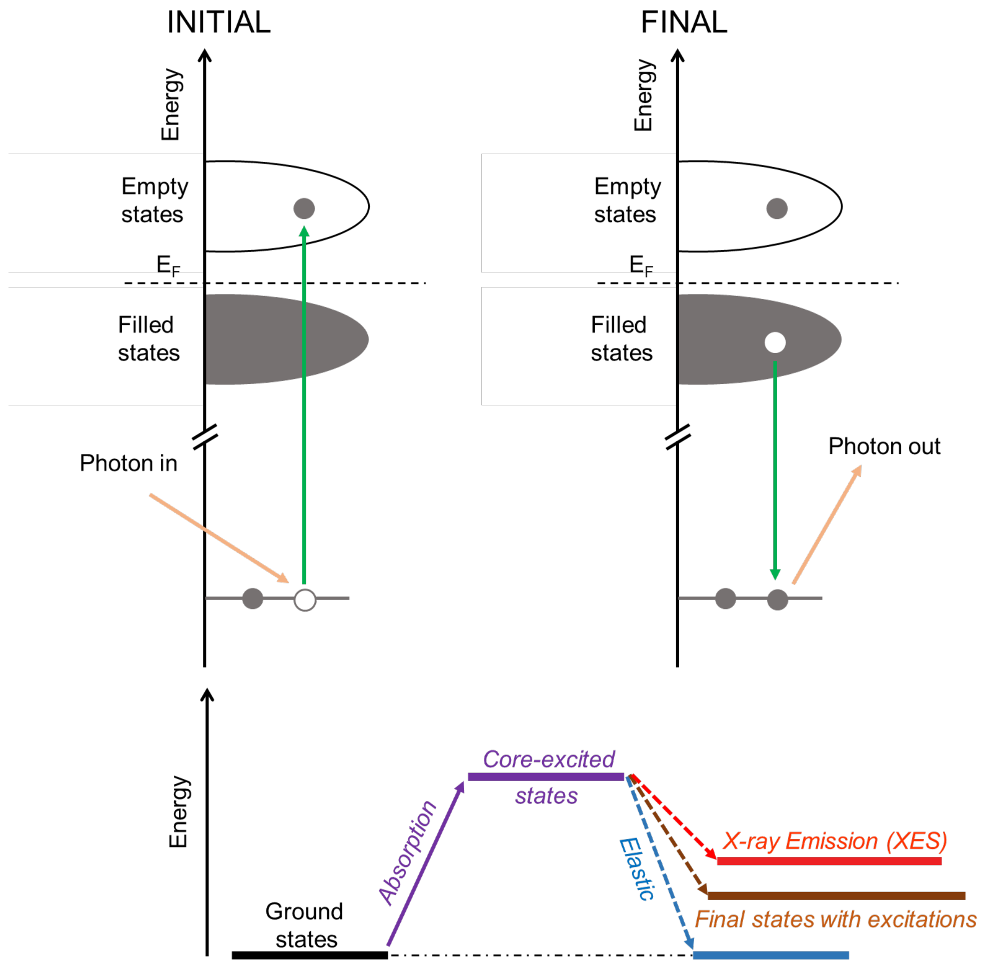

Figure 2.4 Schematic diagram of RIXS. The figure illustrates the two-step process of excitation and de-excitation that characterizes the RIXS spectrum, highlighting the different final states resulting from de-excitation, which include the elastic peak, emission peak, and energy loss peak. Adapted from reference[70].

2.3 Resonant inelastic X-ray scattering (RIXS)

Resonant inelastic X-ray scattering (RIXS) is a highly sensitive spectroscopic technique extensively employed to study the electronic structure, excited states, and phonon behaviour of materials[70]. RIXS integrates the fundamental principles of resonant light absorption and inelastic scattering to provide comprehensive information about the internal state of a sample. The RIXS process consists of two primary steps. Similar to SXAS, core-level electrons are excited to unoccupied states by photons with adjustable energy (**Figure 2.4**, top panel). At this stage, the system enters an excited state, known as the intermediate state in RIXS, resulting in holes in the core energy level and the presence of excited electrons in unoccupied states. Subsequently, these excited states decay to fill the core holes, leading to distinct features in the decay process: (1) If the excited state returns to the same final state as the ground state and emits energy equal to the excitation energy, the resulting peak is referred to as the elastic feature. (2) If, during decay, valence band electrons transition to the core-level holes, the energy of the emitted photon becomes independent of the incident energy, depending solely on the energy difference between the valence band electrons and the core energy level holes; this scenario produces what is known as the emission peak. (3) To stabilize the excited state after photon absorption, the core hole in the intermediate state generates a strong potential that screens the outer shell electrons. This screening effect can induce various other excitations at lower energy scales, including lattice vibrations (phonons), spin flips (spinons or magnons), charge transfer excitations, and d-d transitions (between transition metal d orbitals). Once the core hole is filled, these excitations remain within the system. The energy difference between the emitted photon and the incident photon corresponds to the energy required for these excitations, leading to what is referred to as the energy loss feature. Consequently, through the excitation and decay processes, the system can reach three distinct types of final states (**Figure 2.4**, bottom). Compared to SXAS, RIXS enhances the data obtained from a single excitation energy by decomposing it into a detailed distribution curve of emission energies. This capability introduces a new dimension of information along the emission energy axis, facilitating a more nuanced investigation of various chemical states that may be obscured within the characteristic peaks of the SXAS spectrum at specific excitation energies.

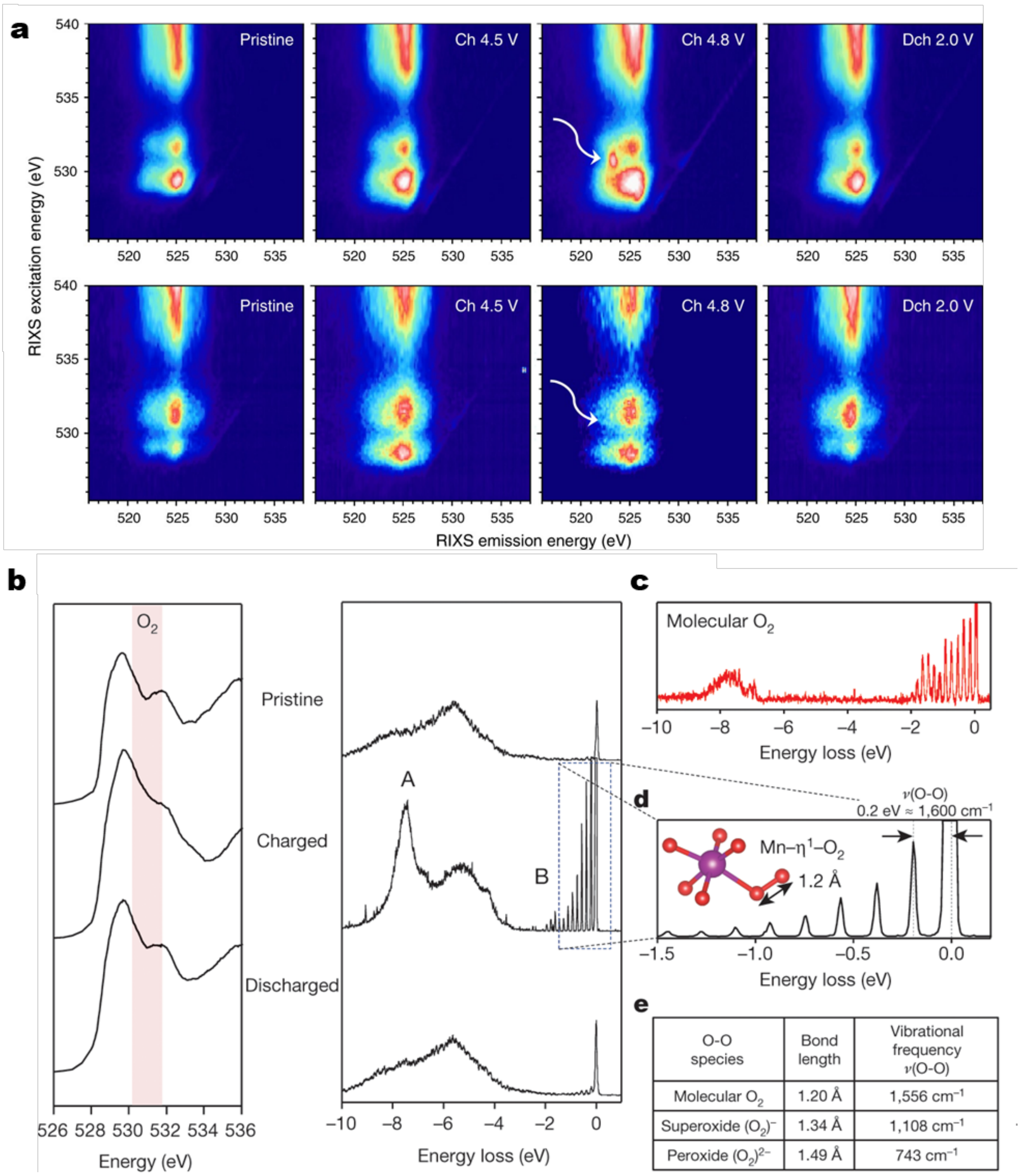

O-O species	Bond length	Vibrational frequency ν(O-O)
Molecular O_2	1.20 Å	1,556 cm^{-1}
Superoxide $(O_2)^-$	1.34 Å	1,108 cm^{-1}
Peroxide $(O_2)^{2-}$	1.49 Å	743 cm^{-1}

Figure 2.5 (a) O K-edge RIXS maps of LNMO (top) and LNRO (bottom) electrodes at different states of charge. The while arrow points to the specific oxygen redox state that is absent in LNRO. (b) Oxygen K-edge XAS and high-resolution RIXS spectra recorded at an excitation energy of 531 eV for $Na_{0.75}[Li_{0.25}Mn_{0.75}]O_2$*. (c) The high-resolution RIXS spectrum for molecular* O_2 *at 530.3 eV. (d) With high-resolution RIXS, feature B in a is resolved into a progression of energy-loss peaks, arising from the vibrations of the O–O bond with a fundamental vibrational frequency. (e) Literature values for the bond lengths and frequencies of O–O dimers for comparison. Adapted from reference*[82,83].

William[84] et al. combined scanning transmission X-ray microscopy and nanoscale X-ray absorption spectroscopy (STXM-XAS) with resonant inelastic X-ray scattering (RIXS) and various structural probes to investigate the anion redox mechanisms in Li-rich cathodes. After charging to 4.6 V and using an excitation energy of 530.8 eV, a notable new emission feature was observed at 523.25 eV, which distinctly differs from the broad emission feature detected in the range of 522-527 eV, associated with the hybridized states of transition metal-oxygen (TM-O). Subsequently, Tong[82] et al. observed a prominent RIXS feature (indicated by the white arrow in **Figure 2.5a**) at excitation and emission energies of 530.8 eV and 523.75 eV, respectively, when the Li-rich cathode was charged to 4.8 V. Importantly, this sharp RIXS feature disappeared upon discharging to 2.0 V, suggesting that it serves as a unique fingerprint of the changes in oxygen states during the electrochemical process. In a subsequent study, Peter[47,83,85,86] et al. employed high-resolution RIXS spectroscopy that surpassed the resolution of previous investigations to uncover new insights into the oxygen redox processes in layered oxides. As illustrated in **Figure 2.5b-e**, their data reveal the intricate fine structure of the elastic peak, labelled B, which consists of a series of energy-loss peaks corresponding to the vibrations of the O–O bond, exhibiting a fundamental vibrational frequency of approximately 1,600 cm^{-1}, closely aligning with that of molecular O_2[87]. Alongside the broad inelastic peak, labelled A, these features bear a striking resemblance to the RIXS spectrum of gaseous molecular O_2 in previous study. Furthermore, they proposed a novel mechanism by which molecular O_2 is trapped within cathodes. Specifically, during the charging process, the in-plane migration of TM ions, predominantly Mn, leads to the formation of vacancy clusters capable of encapsulating molecular O_2. These findings also elucidate the voltage hysteresis observed in Li-rich cathodes. Additionally, they also examined the trapping of molecular O_2 in Li-stoichiometric $LiNiO_2$ cathodes[88]. Notably, while Li-stoichiometric NCM materials exhibit same RIXS signals for molecular O_2 at high voltages (4.8 V), they do not display voltage hysteresis. Consequently, further research is required to elucidate the relationship between molecular O_2 and voltage hysteresis in Li-rich cathodes. Overall, it is evident that the signal detected through high-resolution RIXS encompasses molecular O_2, which is frequently associated with oxygen redox processes. As such, RIXS represents one of the most effective tools available for characterizing oxygen redox behaviour in battery materials.

Chapter 3 Tailoring superstructure units for enhanced oxygen redox in Li-rich layered oxides

3.1 Introduction

In contrast to conventional layered cathode oxides, such as $LiCoO_2$, relying solely on transition metal (TM) redox activity, Li-rich layered oxides have emerged as promising cathode materials due to their utilization of both TM and oxygen redox contributions at high voltage, resulting in a remarkable discharge capacity[66,72,89]. However, the instability of oxygen redox triggers severe voltage decay, posing a substantial challenge to commercial applications[90,91]. Over the past decades, intensive studies have been proposed to elucidate the origins of voltage decay, including the continuous reduction of TM valence states, irreversible TM ions migration, and phase transitions (from layered to spinel/rock-salt phases) during cycling[92–95]. Recently, a more profound understanding[96] has emerged, highlighting the crucial role of the accumulation of mesoscale lattice strain and lattice displacement within distinct nanoscale domains ($LiTMO_2$ and Li_2MnO_3) as the driving force behind voltage decay during battery operation. Consequently, conventional post-synthesis treatments such as surface coating have proven ineffective in addressing this issue.

Tailoring the local structure and optimizing chemical composition is emerging as a promising avenue to mitigate voltage decay in layered Li-rich cathodes. For instance, a consensus has emerged form relevant studies, highlighting the detrimental role of localized superstructure domains characterized by in-plane Li/Mn order of Li-rich cathodes, while delocalized or dispersed domains characterized by in-plane Li/Mn disorder effectively improve the oxygen redox reversibility and voltage stability[97–99]. In addition, O2-type cathodes exhibit superior voltage stability compared to traditional O3-type cathodes, attributed to the reversible migration of TM ions[100,101]. Remarkably, an O2-type Li-rich cathode with a capped-honeycomb structure demonstrates negligible voltage decay[102]. However, synthesizing these cathodes through an ion exchange method from P2-type sodium cathode precursors presents challenges for large-scale production. Introducing concentration gradients in Li-rich cathodes, with low manganese and high nickel content on the particle surface, has shown improved voltage retention[103,104]. Nevertheless, uncertainties in nickel/manganese ions migration during high-temperature calcination lead to deviations from the intended design, compromising materials synthesis reproducibility. In terms of optimizing chemical composition, high-nickel Li-rich layered oxides enhance voltage stability by promoting the formation of Ni^{3+} in the pristine material. This serves as a redox buffer, suppressing the redox activation of $Mn^{4+/3+}$ at low potentials[105,106]. Notably, Li et al. demonstrated the superiority of nickel over cobalt in slowing down the kinetics of ligand-to-metal charge transfer, mitigating TM ions migration, and resulting in reduced oxygen release and lower voltage decay[107]. Moreover, these materials can be easily obtained through hydroxide/carbonate co-precipitation, which is currently the preferred synthesis method for large-scale industrial production. Despite their potential, high-nickel Li-rich cathodes, like $Li_{1.2}Ni_{0.4}Mn_{0.4}O_2$, have received less attention due to their unsatisfactory electrochemical behaviour, including lower discharge capacity and slower lithium ions diffusion compared to low-nickel Li-rich cathodes[108–111]. However, there is still no comprehensive explanation for the unsatisfactory electrochemistry of high-nickel Li-rich layered oxides, and no universal solutions to address this dilemma have been identified. Thus, the key to advancing Li-rich cathodes is achieving voltage stability in high-nickel systems without compromising discharge capacity.

In this chapter, we present a comprehensive investigation of cobalt-free Li-rich layered oxides with varying nickel contents ($Li_{1.20}Ni_xMn_{0.8-x}O_2$, x = 0.28, 0.32, 0.36, 0.40). By employing advanced techniques including synchrotron X-ray diffraction (SXRD), X-ray pair distribution function (PDF) analysis, X-ray absorption spectroscopy (XAS), solid-state nuclear magnetic resonance (NMR) spectroscopy, and density functional theory (DFT) calculations, we identify the types of honeycomb superstructure units within the TM layers and, for the first time, elucidate the influence of the valence state of nickel ions on these units. Furthermore, by integrating electrochemical investigations with soft XAS and resonant inelastic X-ray scattering (RIXS) spectroscopy, we establish a direct correlation between oxygen redox behaviours and the ratio of superstructure units. This correlation provides insights into the underlying reasons for the poor electrochemistry observed in high-nickel Li-rich layered oxides. Finally, we propose a practical solution to achieve improved electrochemical performance with reversible oxygen redox by tailoring honeycomb superstructure units in high-nickel Li-rich layered oxides.

3.2 Experimental

3.2.1 Materials synthesis

$Li_{1.2}Ni_xMn_{0.8-x}O_2$ (x = 0.28, 0.32, 0.36, 0.40) materials were synthesized using a hydroxide co-precipitation method followed by a solid-state reaction. First, a 2.0 M aqueous solution containing $NiSO_4 \cdot 6H_2O$ (≥98%, Sigma–Aldrich) and $MnSO_4 \cdot H_2O$ (≥98%, Sigma–Aldrich) (molar ratios of 7:13, 2:3, 9:11 and 1:1 for N28, N32, N36 and N40, respectively), along with a 4.0 M NaOH solution (≥98%, Sigma–Aldrich) and an aqueous 0.5 M $NH_3 \cdot H_2O$ solution (28%-30%, Sigma–Aldrich), were separately fed into a batch reactor with a volume of 1 L. The aqueous TM solution and $NH_3 \cdot H_2O$ solution were fed at the same rate while maintaining the pH value at 11.0 ± 0.2 by adjusting the feeding rate of the NaOH solution. The reaction process was carried out at a temperature of 50 °C and under a N_2 atmosphere. After a reaction duration of 20 h, followed by a 2-h aging process, the precursor was washed three times with deionized water and subsequently dried in an oven at 80 °C for 12 h under an air atmosphere.

The target positive electrodes were obtained by mixing the precursor and Li_2CO_3 (≥99%, Sigma–Aldrich) in a molar ratio of 1:1.5, followed by a heat treatment at 500 °C for 5 h and subsequently at 850 °C for 12 h under an air atmosphere. Similarly, other positive electrodes were prepared utilizing identical procedures except for a change in the ratio of Li_2CO_3 and precursor (1.2:1, 1.3:1, 1.4:1, and 1.5:1 for LM12, LM13, LM14, and LM15, respectively).

3.2.2 Materials characterization

Ex-situ powder diffraction. X-ray diffraction (XRD) measurements were measured by a Mo source powder diffractometer (STOE STADI P) in transmission geometry, with a wavelength of 0.7093 Å. The samples were loaded into capillaries with an outer diameter of 0.5 mm. The acquisition time for each pattern was 150 min. Synchrotron X-ray diffraction (SXRD) measurements were conducted at beamline P02.1, PETRA III (wavelength of ~0.207 Å) at DESY in Hamburg[112,113]. The samples were loaded into capillaries with an outer diameter of 0.5 mm. Measured intensities were collected using a VAREX CT4343 detector (2880 × 2880 pixels, 150 × 150 μm^2 each) and the acquisition time of 120 s for each pattern. NIST SRM 660c (LaB_6) was used for geometry calibration performed with the software DAWN[114] followed by image integration including geometry, solid-angle, and polarization corrections.

In-situ powder diffraction. In-situ XRD measurements were conducted using an Ag source powder diffractometer (STOE STADI P, wavelength of 0.5594 Å) in transmission geometry. In-situ 2032-type coin cells with a Kapton window were employed. All cells were cycled at C/10 (1C defined as 200 mA g^{-1}) in a 2.0-4.7 V range for 1 cycle at room temperature using a battery system (NOVA, Metrohm). The collection time for each pattern was set to 20 min. All Rietveld refinements were performed using the Fullprof software package[115].

Pair distribution function. Pair distribution function (PDF) measurements were performed at beamline ID31 at the European Synchrotron Radiation Facility (ESRF). The sample powders were loaded into cylindrical slots (approx. 1 mm thickness) held between Kapton windows in a high-throughput sample holder. Each sample was measured in a transmission geometry with an incident X-ray energy of 75.00 keV (wavelength of 0.1653 Å). Measured intensities were collected using a Pilatus CdTe 2M detector (1679 × 1475 pixels, 172 × 172 μm^2 each) positioned with the incident beam in the corner of the detector. The sample-to-detector distance was approximately 0.3 m for the total scattering measurement. Background measurements for the empty windows were measured and subtracted. NIST SRM 660b (LaB_6) was used for geometry calibration performed with the software pyFAI followed by image integration including a flat-field, geometry, solid-angle, and polarization corrections. The calculated PDF data was performed by PDFgui[116] software package.

SEM. The morphology of all samples was investigated by a scanning electron microscopy (SEM, Zeiss Merlin) with an acceleration voltage of 10 kV.

TEM. Scanning Transmission electron microscopy (STEM) energy dispersive X-ray spectroscopy (EDS) mapping and electron energy loss spectroscopy (EELS) experiments were conducted using a double aberration corrected Thermo-Fisher Themis-Z (operated at 300 kV equipped with a Super-X EDS detector and a Gaten GIF Continuum 970 HighRes EELS spectrometer). The structural information of samples was studied by high-resolution transmission electron microscopy (HRTEM). Each specimen was examined using Thermofisher Talos F200X TEM operated at 200 kV. The atomic structures were plotted using VESTA software[117].

ICP–OES. The compositions of the samples were quantitatively determined by inductively coupled plasma-optical emission spectroscopy (ICP–OES) using a Thermo Fischer Scientific iCAP 7600 DUO.

3.2.3 Spectroscopy characterization

XAS. Hard X-ray absorption spectroscopy (XAS) experiments were performed at the XAS beamline of the KIT synchrotron in in Karlsruhe. These measurements were conducted at room temperature, employing the transmission mode for data acquisition. The obtained XAS data were processed using ATHENA software package[118].

SXAS. Soft X-ray absorption spectroscopy (SXAS), experiments were carried out at the WERA beamline at the KARA synchrotron in Karlsruhe. The Ni L-edge and O K-edge spectra were recorded using the fluorescence yield (FY) detection mode and the inverse partial fluorescence yield (iFY) for the Mn L-edge spectra.

RIXS. Resonant inelastic X-ray scattering (RIXS) experiments were conducted at beamline U41-PEAXIS at BESSY II, located at Helmholtz-Zentrum Berlin (HZB)[119]. A vacuum suitcase was used to transfer the sample from an N_2-filled glovebox to the test chamber. The spectrometer was positioned at specular conditions relative to 60° scattering angle and was optimized to a combined resolution of 90 meV using a carbon tape. The O K-edge RIXS spectra of the samples were collected at an excitation energy of 531.0 eV. The acquisition time for each pattern was 30 min. RIXS mapping was measured in 0.5 eV energy steps from 526 eV to 534 eV. Data were processed using the Adler-4.0 software package.

NMR. Magic-angle spinning (MAS) nuclear magnetic resonance (NMR) spectroscopy was performed on a Bruker Avance neo 200 MHz spectrometer with a magnetic field strength of 4.7 T. MAS spinning was carried out using 1.3 mm rotors at a frequency of 55 kHz. For the ^{6}Li

NMR experiments, $^{6}LiOH\cdot H_2O$ (95 atom%, Sigma–Aldrich) was utilized as the Li source for synthesis. The Larmor frequencies for ^{6}Li and ^{7}Li NMR were 29.5 MHz and 77.8 MHz, respectively. Spectra were acquired employing a rotor-synchronized Hahn-echo pulse sequence, with a 90° pulse length of 0.85 μs for ^{7}Li and 1.6 μs for ^{6}Li. All spectral shifts were referenced to an aqueous solution of LiCl (^{6}LiCl for ^{6}Li) at 0 ppm. The spectral intensities were normalized based on the sample mass and the number of scans. The NMR spectra were fitted using DMFIT program[120].

3.2.4 Theoretical calculations

DFT calculations. The pre-optimization of the structure model was done by using the Vienna ab-initio simulation package (VASP) within the projector augmented-wave approach using the Perdew-Burke-Ernzerhof (PBE) with r^{2}SCAN functional[121–125]. The correlation effects of the 3d-Ni and Mn orbitals (corresponding parameter U_{Mn} = 1.8 eV, U_{Ni} = 2.1 eV) and long-range dispersion with Grimme's D4 correction were taken into account[126,127]. A plane-wave energy cut-off of 450 eV and 2×2×2 gamma centered *k*-point grid were used for the total energy. To obtain reasonable electronic properties, the obtained structure model was reoptimized with CRYSTAL17 program version 1.0.2 using the PW1PW hybrid functional which has been successfully used, e.g., for the determination of transition metal oxide nitride phase stability and ortho phosphates before[128–130]. Long-range London dispersion was taken into account with Grimme's D3 correction with Becke-Johnson damping[131–133]. The empirical s_8 parameter was re-adjusted in preliminary calculations of the relative stability of α_{II}-$VOPO_4$ and α-$NbOPO_4$, in which a modified value of s_8 = 1.5363 was obtained[134]. Several convergence parameters were changed to increase the numerical precision of the calculations. The truncation criteria for bielectronic integrals (TOLINTEG) were set to 7 7 7 7 14.

To accelerate the SCF convergence, FMIXING was increased from default 30% to 85%. The Monkhorst-Pack shrinking factor is 4×4. The pob-TZVP-rev2 basis sets were used in all calculations[135,136]. Since Ni and Mn have magnetic moments, some pre-settings needed to be done. The calculation of the spins was done in an antiferromagnetic configuration with a maximum total spin of 66. Additionally, SPINLOCK was set to 66 30. The densities of states are calculated according to the Fourier-Legendre technique[137]. For a reliable result, the number of *k*-points must be set to 4 4. The development of different structure models for $Li_{44}Mn_{18}Ni_{10}O_{72}$ ($Li_{1.22}Mn_{0.50}Ni_{0.28}O_2$) was done by the program supercell[138]. The initial structure model is based on $LiMnO_2$ (S.G. *C*2/*m*, *a* = 4.9370(10) Å, *b* = 8.5320(10) Å, *c* = 5.030(2) Å, *β* = 109.46(3)°). For the calculations the primitive cell was used (*a* = 4.928 Å, *b* = 4.928 Å, *c* = 5.030 Å, *α* = 80.35°, *β* = 99.60°, *γ* = 60.11°) with adjusted occupancies for the metal cations Li, Mn and Ni (**Table A3**). For the given supercell input file with the partial S.O.F in the transition metal positions with a 3×2×2 cell ca. $3.1 \cdot 10^8$ different combinations for $Li_{44}Mn_{18}Ni_{10}O_{72}$ were found. The structure model for $Li_{44}Mn_{18}Ni_{10}O_{72}$ was chosen based on low coulombic energy and the honeycomb superstructure $LiNiMn_5$. **Figure 3.9a** shows the exemplary crystal structure of the model. Atomic coordinates are given in **Table A4**.

3.2.5 Electrochemical characterization

Electrode preparation. The electrodes were prepared by thoroughly mixing the active material, Super C65 conductive carbon black (MTI Co., Ltd.), and polyvinylidene fluoride (PVDF, Sigma-Aldrich) in a mass ratio of 8:1:1 using a mortar. N-methyl-2-pyrrolidone (NMP) with a moisture content of less than 0.1% (VMR) was used as the solvent. The resulting mixture was then processed in a planetary mixer (THINKY ARV-310) with 2000 rpm for 10 min under an air atmosphere to ensure homogeneity. The resulting slurry was applied to aluminium foil (15 μm thickness, häberle LABORTECHNIK GmbH & Co.KG) at a speed of 25.0 mm s^{-1} using a ZUA 2000 Universal applicator and the thickness was 150 nm. The coated aluminium foil was subsequently dried in an oven at 80 °C under ambient conditions to evaporate the NMP solvent. After a drying period of 6 h, the electrode material was punched into discs with a diameter of 12 mm (with an active material loading of approximately 3 mg cm^{-2}) using a handheld punch (NOGAMIGIKEN Co., Ltd.). A subsequent drying step was conducted using a Büchi glass oven (B-585) under vacuum conditions at 120 °C for 12 h.

Galvanostatic measurements. To evaluate the electrochemical performance, 2025-type coin cells were assembled. These cells comprised a Li metal anode (14 mm diameter, 0.25 mm thickness, PI-KEM), a single-layer Celgard 2500 membrane (25 μm thickness, 55% porosity, DODO Co., Ltd.) as the separator, and 80 μL of electrolyte consisting of 1 M lithium hexafluorophosphate ($LiPF_6$) dissolved in a solvent mixture of ethylene carbonate (EC), ethyl methyl carbonate (EMC), and dimethyl carbonate (DMC) in a volume ratio of 1:1:1, with moisture content maintained below 10 ppm (DODO Co., Ltd.). All assembly procedures were conducted within an argon-filled glovebox (O_2 and H_2O < 0.1 ppm). The cells were cycled at a constant temperature of 25 °C using a Biologic VMP3 multichannel battery test system within a voltage range of 2.0–4.7 V. The charging protocol included a constant voltage step at 4.7 V for 10 min, followed by a 10-min resting period after each charge-discharge cycle. To ensure reproducibility, all electrochemical experiments were performed using a minimum of two-coin cells. Additionally, the current density for each cell was calculated based on the mass of the active material in the electrode. The coulombic efficiency was determined as the percentage ratio of discharging capacity to charging capacity, multiplied by 100. The average cell discharge voltage was defined as the voltage when the discharge capacity reached half of its maximum. For all ex-situ electrode measurements conducted in this work, which included

SXAS, NMR, and RIXS, the coin cells were subjected to specific voltage applications before being disassembled in the glovebox. The obtained electrodes were then thoroughly washed with DMC solvent three times and sealed under vacuum conditions within the glovebox.

3.3 Results and Discussion

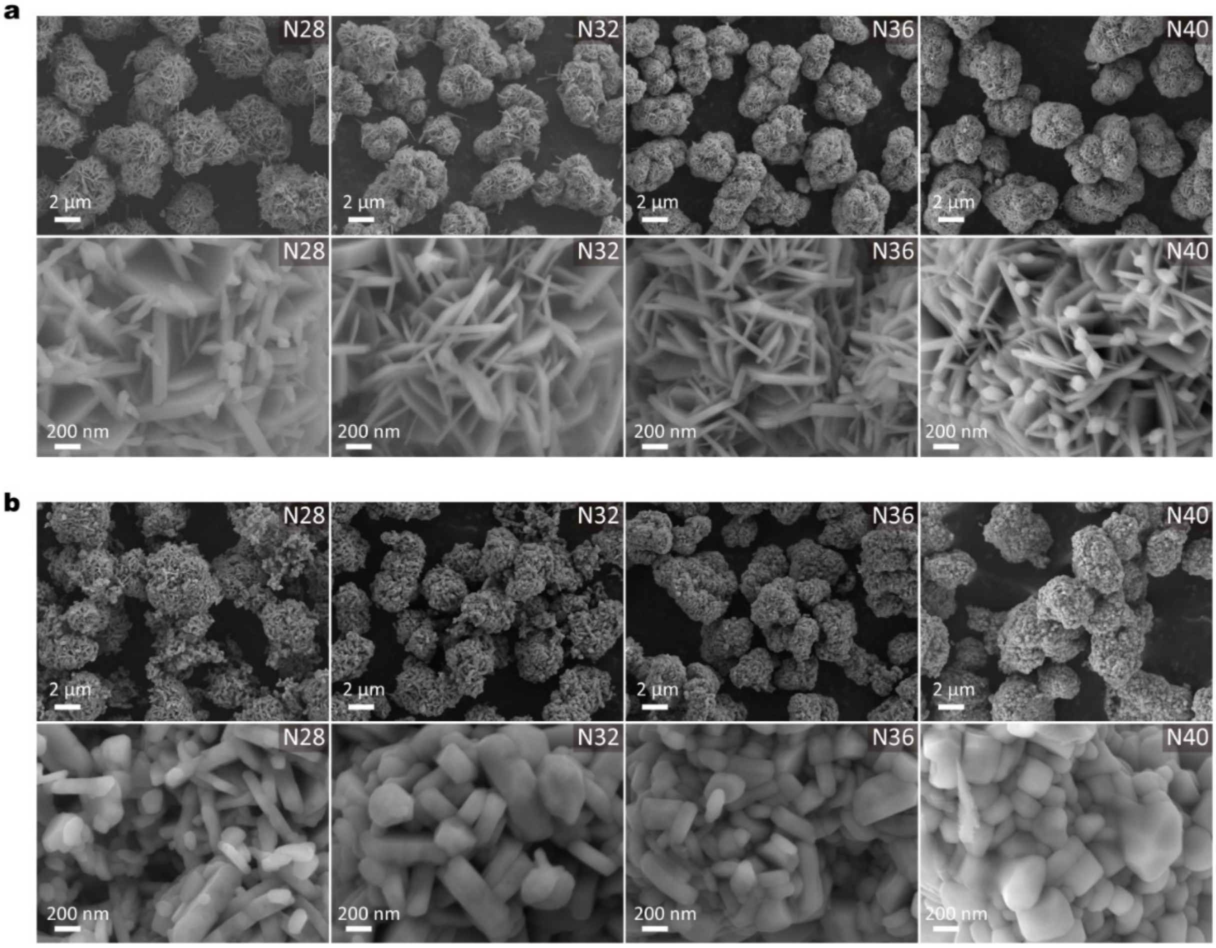

Figure 3.1 SEM images of (a) hydroxide precursors and (b) synthesized materials of N28, N32, N36, and N40 powders.

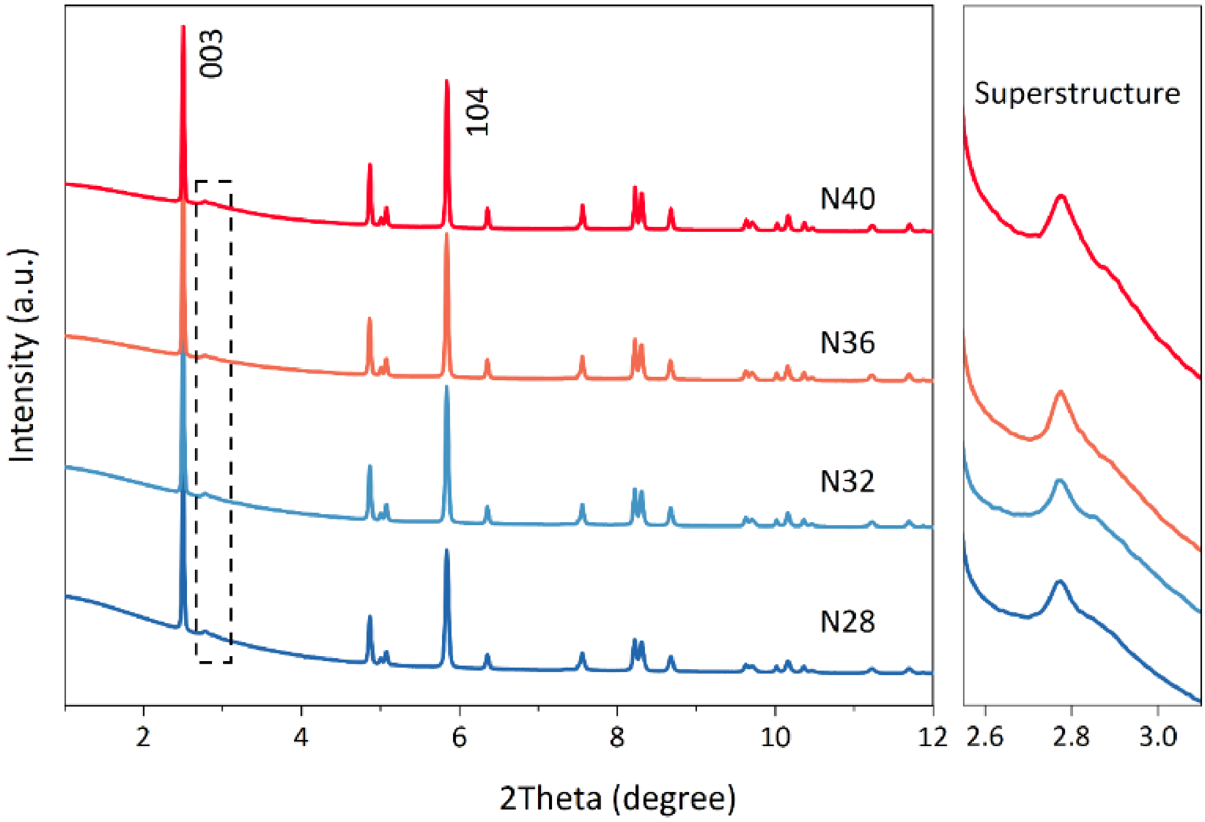

Figure 3.2 SXRD patterns for N28, N32, N36 and N40 powders. The wavelength was 0.2073 Å.

We synthesized a series of precursors with varying Ni/Mn ratios using the hydroxide co-precipitation method. The specific chemical compositions are $Ni_{0.35}Mn_{0.65}(OH)_2$, $Ni_{0.40}Mn_{0.60}(OH)_2$, $Ni_{0.45}Mn_{0.55}(OH)_2$, and $Ni_{0.50}Mn_{0.50}(OH)_2$. The $Li_{1.20}Ni_xMn_{0.8-x}O_2$ cathodes, with *x* values of 0.28, 0.32, 0.36, and 0.40, were synthesized via solid-state reactions using above TM hydroxide precursors and Li_2CO_3 (Li/TM molar ratio = 1.5) under ambient air conditions. In this section, these materials are denoted as N28, N32, N36, and N40, respectively. Scanning electron microscopy (SEM) images (**Figure 3.1a**) show that all precursors have random flake primary particles stacked into spherical secondary particles, each approximately 6 μm in diameter. After the calcination treatment with Li_2CO_3, the secondary particles remain spherical, while the primary particles increase in thickness (**Figure 3.1b**) due to continued crystalline growth at high temperatures. High-resolution synchrotron X-ray diffraction (SXRD) measurements were used to obtain the crystal structure information. As shown in **Figure 3.2**, the main Bragg reflections for N28, N32, N36, and N40 correspond to a layered rhombohedral (*R-3m*) phase without impurities. Additionally, the broad diffraction peaks at 2θ values of 2.7-3.1° indicate honeycomb Li/TM ordering (*C2/m* space group) within the TM layer. Meanwhile, these superstructure diffraction peaks show similar intensities (see enlarged image on the right), indicating all materials have comparable amounts and faulting of honeycomb domains.

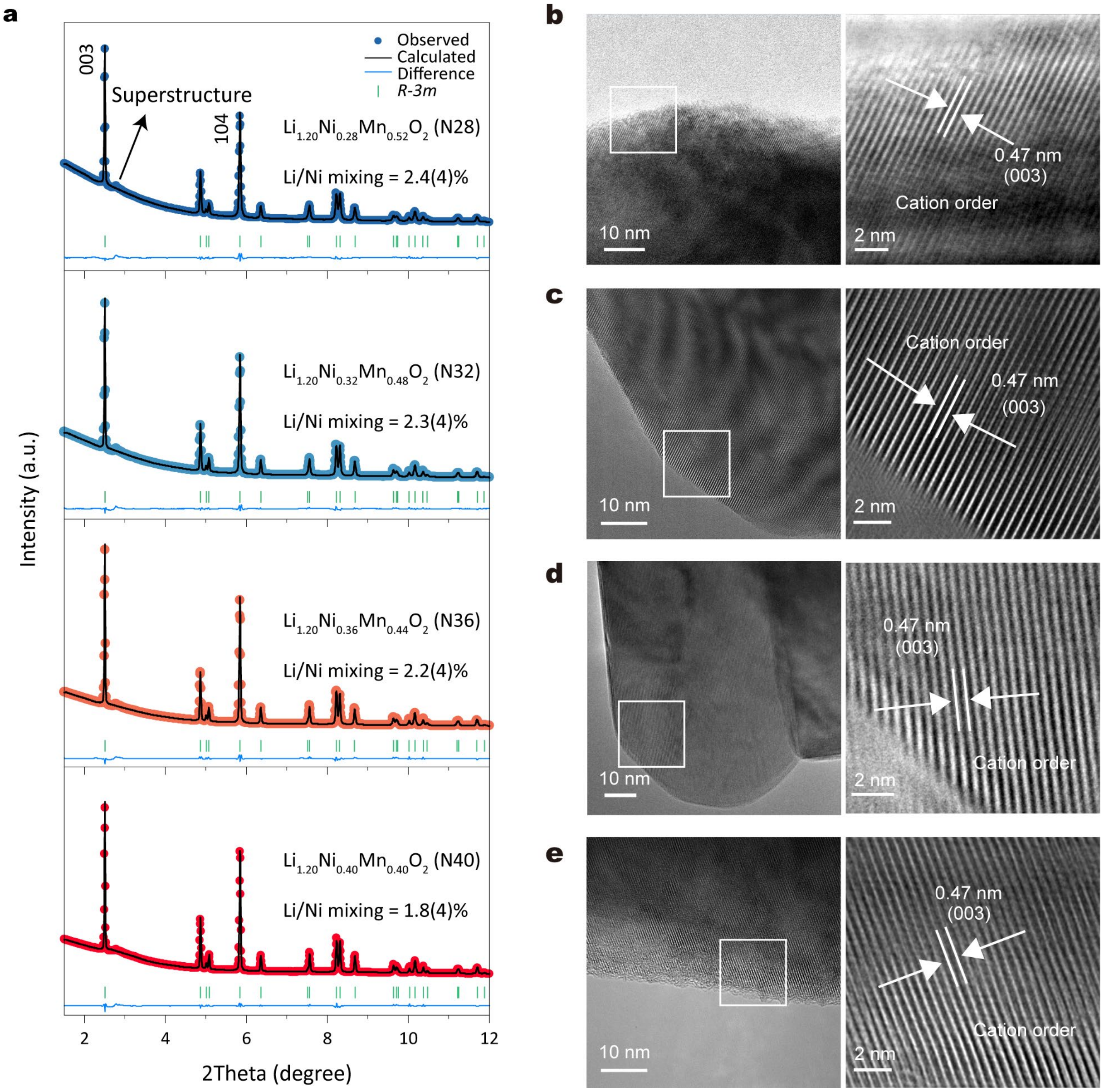

Figure 3.3 (a) SXRD patterns and corresponding refinement results for N28, N32, N36 and N40 powders. The Rietveld refinement was performed with space group R-3m. The wavelength was 0.2073 Å. HRTEM images of N28 (b), N32 (c), N36 (d), and N40 (e) powders.

To obtain detailed lattice parameters, we conducted SXRD refinements (**Figure 3.3a**). For simplicity, we used a single *R-3m* phase as the initial structural model. The detailed refinement results are shown in **Table A1**. The lattice parameters, including *a* and *c*, show no significant differences across these cathodes. To investigate the Li/Ni mixing changes, we have refined the Li/Ni occupancy while constraining the sum of both to two per formula unit. The values for N28, N32, N36, and N40 are 2.4(4), 2.3(4), 2.2(4), and 1.8(4)%, respectively. High-resolution transmission electron microscopy (HRTEM) measurements were performed to verify local atomic arrangements. The TEM images (**Figure 3.3b-e**) of N28, N32, N36, and N40 show clear lattice fringes without obvious evidence of Li/Ni mixing, consistent with the small values if Li/Ni exchange obtained from the SXRD results. These results suggest that the Ni content in Li-rich layered cathodes has little effect on the structural arrangement. Additionally, the observed average interplanar spacing of approximately 0.47 nm corresponds to the $(003)_R$ or $(001)_M$ plane of the layered rhombohedral (*R-3m*) or monoclinic (*C2/m*) structures.

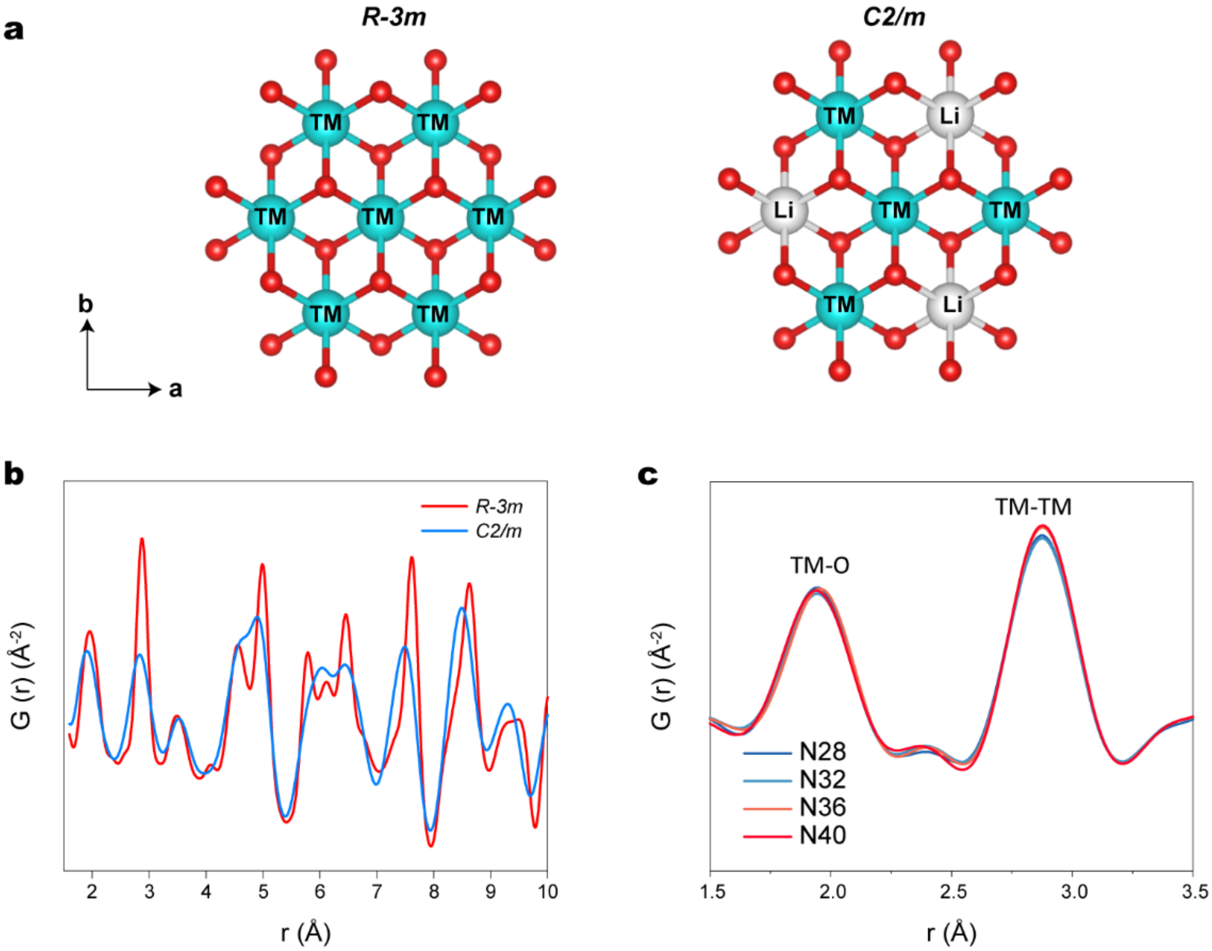

Figure 3.4 (a) Schematic representation of the crystal structures of R-3m and C2/m. (b) Calculated PDF patterns based on the R-3m and C2/m model. (c) PDF patterns of N28, N32, N36 and N40 powders.

To capture local structural arrangement, X-ray pair distribution function (PDF) measurements were conducted. The PDF patterns of $LiMnO_2$ and Li_2MnO_3 are calculated and shown in **Figure 3.4b**. The first two peaks below 3.0 Å represent the octahedral TM-O and the nearest TM-TM atom pairs, respectively[139]. The intensity of the second PDF peak (~2.86 Å) differs significantly between the *R-3m* model (mostly TM-TM pairs, **Figure 3.4a**) and the *C2/m* model (partial TM-TM and partial Li-TM pairs, **Figure 3.4a**), leading to a distinct difference in the intensity ratio of the first (I1) and second (I2) PDF peaks. This I1/I2 ratio for the *R-3m* model is approximately 1/2, while for the *R-3m* model is about 1. This distinction arises from the unique Li/Mn ordering in Li_2MnO_3, where one-third of the Mn ions at the 3b sites are replaced by Li ions (i.e., Li_2MnO_3 = $Li[Li_{1/3}Mn_{2/3}]O_2$). Consequently, the intensity of the second PDF peak is significantly weakened in the *C2/m* structure due to the relatively poor X-ray scattering capability of the Mn-Li atom pairs. As shown in **Figure 3.4c**, the PDF patterns of N28, N32, N36, and N40 show no noticeable differences in the first two PDF peaks, indicating nearly identical atomic arrangements across all cathodes. Combining the structural analyses described above, Li-rich cathodes with different Ni/Mn ratios exhibit similar morphology, superstructure content, Li/Ni mixing, and atomic arrangements.

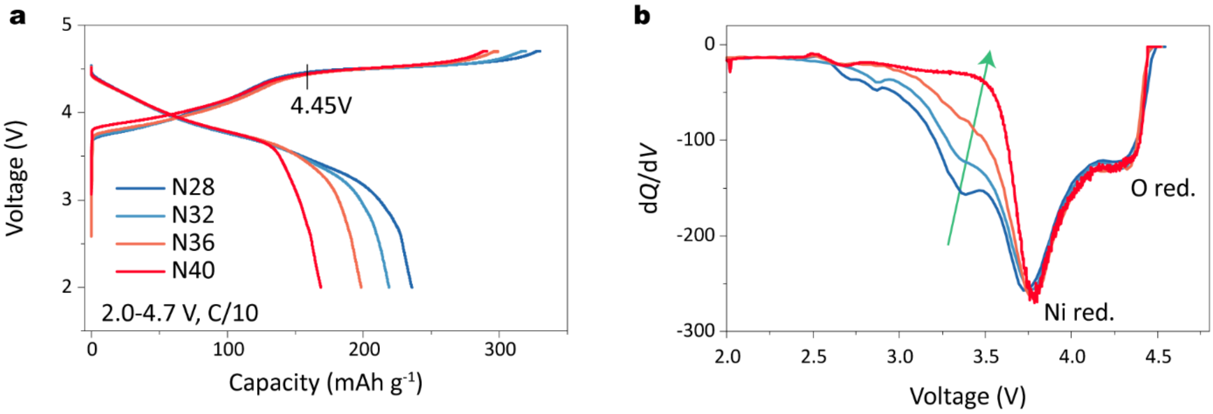

Figure 3.5 (a) Charge and discharge curves and (b) corresponding dQ/dV curves of N28, N32, N36, and N40 cathode in the first cycle in the voltage range of 2.0-4.7 V at C/10 at 25 °C.

We then evaluated the electrochemical performance of these cathodes using coin-type half cells at a rate of C/10 (1C is defined as 200 mA g^{-1}) within the voltage range of 2.0-4.7 V at 25 °C. **Figure 3.5a** displays the characteristic voltage profiles of Li-rich layered oxides, featuring a sloping part below 4.45 V and a subsequent plateau above 4.45 V[96]. The former is associated with cationic redox activity in $LiTMO_2$ domains, whereas the latter involves anionic (oxygen) redox activity in Li_2MnO_3 domains. Despite comparable total charge capacities, a notable divergence emerges in discharge capacity with increasing nickel content, leading to a gradual decrease. For example, N28 and N40 exhibit discharge capacities of 235.6 and 168.8 mAh g^{-1}, with initial columbic efficiencies (ICE) of 71.4% and 58.1%, respectively. Meanwhile, during discharging, all cathodes display nearly overlapping curves above 3.7 V. The primary difference arises from the reduction plateau at approximately 3.3 V, which gradually disappears, as evident in the differential capacity (dQ/dV) curves depicted in **Figure 3.5b** (indicated by the green arrow). From previous studies, reduction peaks around 4.4 V and 3.7 V are typically associated with the reduction of oxygen and nickel at high and mid potentials, respectively. The peak below 3.7 V, corresponding to low potential, likely relates to the reduction of oxygen or manganese. Distinguishing these peaks is challenging in low-nickel Li-rich cathodes due to their overlap. However, in high-nickel Li-rich cathodes, the low-potential peak nearly disappears as the nickel content increases. Thus, high-nickel cathodes serve as an ideal model for investigating the redox mechanism in this region.

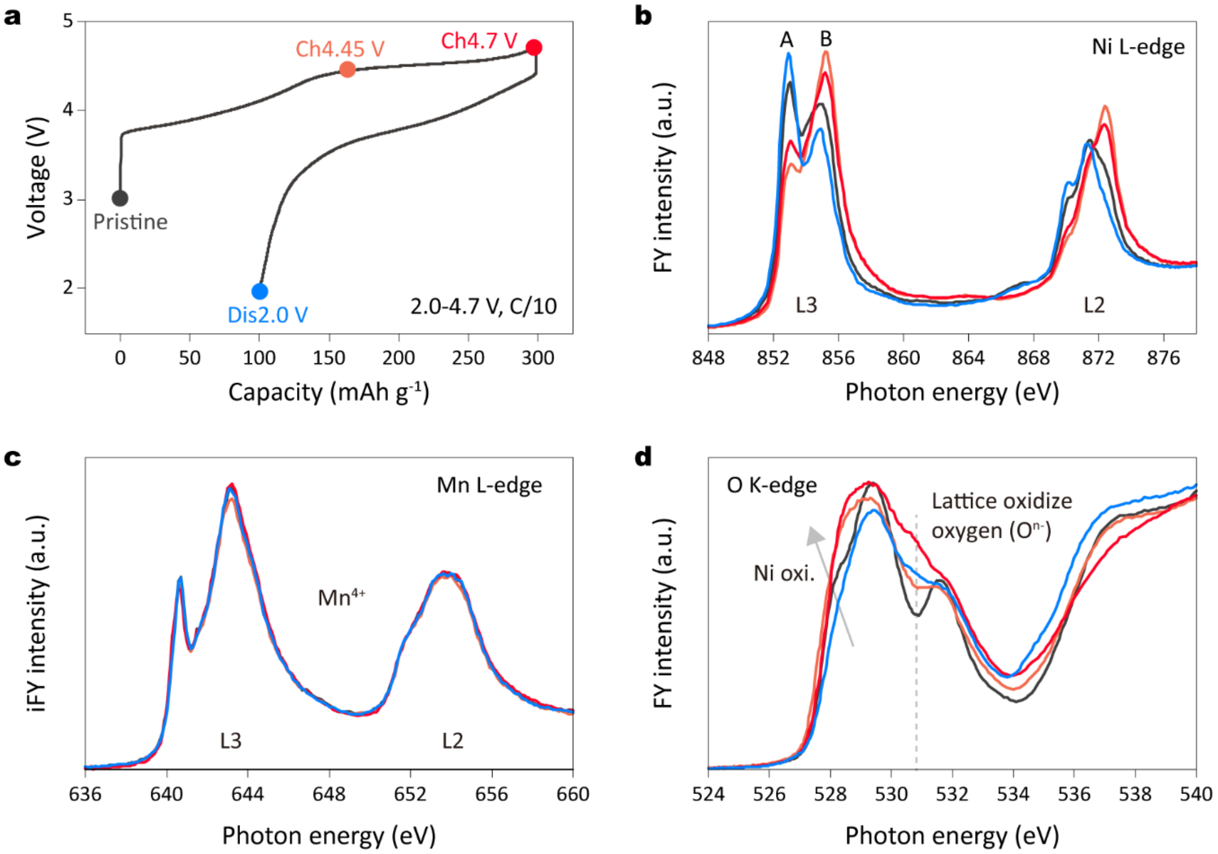

Figure 3.6 (a) Initial charge/discharge curves for N36 with specific points marked for SXAS measurements. SXAS results of the Ni L-edge (b), Mn L-edge (c), and O K-edge (d) collected at pristine, charge to 4.45 V, charge to 4.7 V, and discharge to 2.0 V states. The FY mode was applied for Ni and O and the iFY mode was applied for Mn.

To verify the redox nature of the dQ/dV peak observed in the region below 3.7 V, we conducted soft X-ray absorption spectroscopy (SXAS) measurements, using N36 as an example. Ni and O were analyzed in the fluorescence-yield mode (FY), while Mn was examined in the inverse partial-fluorescence-yield mode (iFY) at different charge/discharge states (as marked in **Figure 3.6a**). FY and iFY measurements are sensitive to a depth of approximately 100 nm, thus providing information about the bulk of the cathode material. Charging to 4.45 V led to Ni oxidation, evidenced by a decrease in peak A intensity (~852.9 eV) and an increase in peak B (~854.8 eV) in the Ni L3-edge spectra (**Figure 3.6b**)[140,141]. At the end of the 4.7 V charge, the spectra exhibit slightly inverted changes, possibly related to charge transfer from ligand to metal[107]. Upon discharging to 2.0 V, reversed changes in the Ni L3-edge spectra indicate Ni reduction, with peak A showing higher intensity and peak B lower intensity compared to the pristine state, suggesting a reduction of nickel species to a lower valence state. The Mn L-edge spectra remain constant, indicating Mn stability in an inactive Mn^{4+} valence state throughout the entire process (**Figure 3.6c**). In the O K-edge spectra (**Figure 3.6d**), the pre-edge region (below 535 eV) primarily reflects the electron transition from O 1s level to the unoccupied TM 3d-O 2p hybridized states[72,142,143]. Charging to 4.45 V induces increased intensity at around 528.5 eV (marked as a grey arrow), attributed to Ni oxidation, consistent with prior analysis. Additionally, a new peak emerges at approximately 530.8 eV (dashed lines), becoming more pronounced upon charging to 4.7 V. This peak is recognized as characteristic of oxidized oxygen species, as observed in the Li-rich cathodes[79,144]. Notably, this peak associated with oxidized oxygen retains some intensity after discharging of 2.0 V, failing to fully revert to its pristine state, suggesting incomplete oxygen redox within the material.

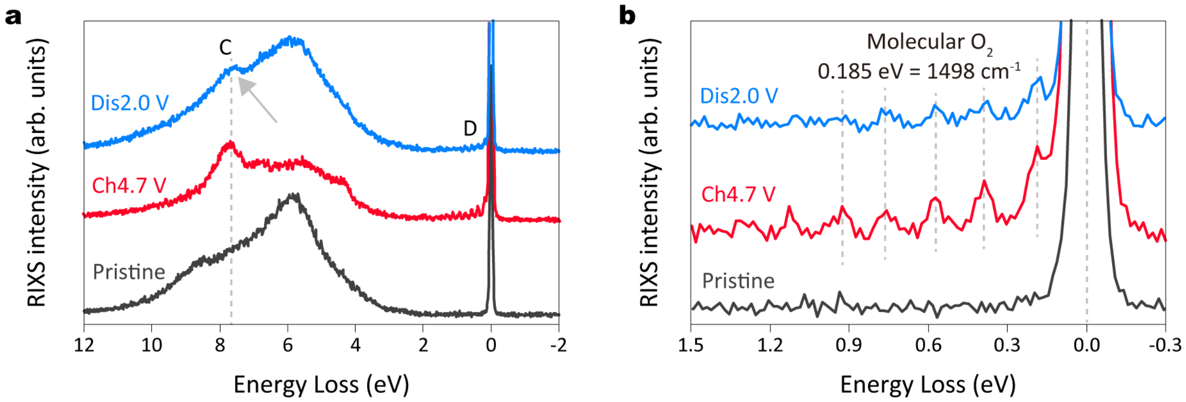

Figure 3.7 (a) The O K-edge RIXS spectra collected at an excitation energy of 531 eV at pristine, charge to 4.7 V, and discharged to 2.0 V states in the first cycle and (b) an enlarged view of the elastic region (0-1 eV) for N36.

To further elucidate the nature of oxidized lattice oxygen, we conducted O K-edge resonant inelastic X-ray scattering (RIXS) measurements. In **Figure 3.7a**, at 4.7 V in the charged state, N36 exhibits a distinct characteristic peak C (around 7.8 eV, denoted by the dashed line) and vibrational peak D around the elastic region (0 eV). In addition, the enlarged view of the vibrational peak is presented in **Figure 3.7b**, revealing vibrational frequencies of 1498 cm^{-1}, similar to the O-O bond length of molecular O_2, aligning with recent research findings[47,83,85–87,145–149]. More importantly, after discharging to 2.0 V, the distinctive feature of molecular O_2 persists (indicated by the grey arrow), suggesting an incomplete reduction of molecular O_2 to O^{2-} species. These findings are consistent with the above SXAS results. Thus, we identify that the incomplete oxygen redox occurs at a low potential (3.3 V) in Li-rich layered oxides for a high-nickel system.

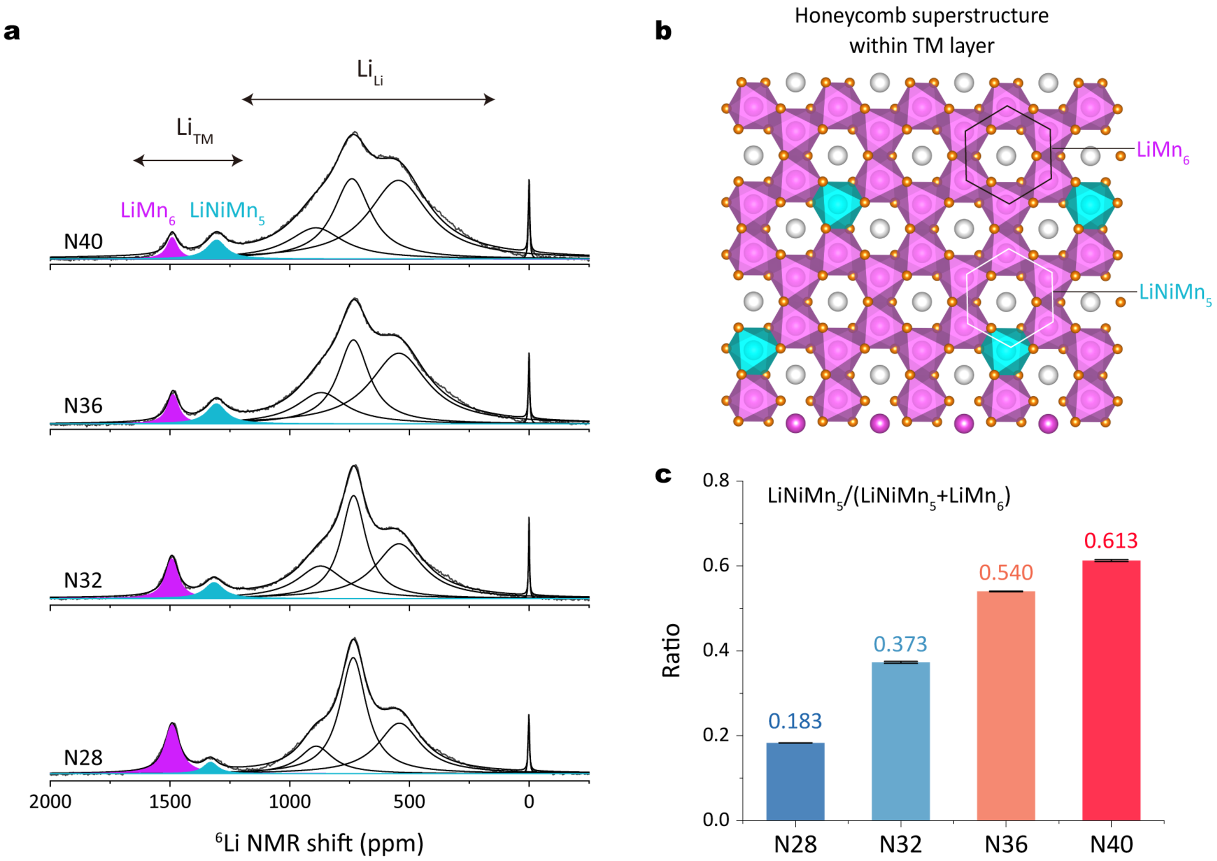

Figure 3.8 (a) ^{6}Li MAS NMR spectra and fitting results for N28, N32, N36, and N40 powders. (b) In-plane ordering of Li (gray) and Mn (purple octahedra) or Ni (blue octahedra) within TM layers forming LiMn$_6$ and LiNiMn$_5$ superstructure units. (c) The ratio of LiNiMN$_5$/(LiNiMn$_5$ + LiMn$_6$). The error bars in (c) correspond to the s.d. of three independent fitting. Data are given as average ± s.d.

Despite having similar morphology, superstructure content, Li/Ni mixing, atomic arrangements, and charging capacities, why is there a significant difference in discharge capacity among these materials? As discussed in the Introduction, this abnormal electrochemical phenomenon has been observed in other studies, though no plausible explanation has been found. Typically, molecular O_2, in the charged state, is trapped in vacancy clusters within the TM layer of Li-rich layered oxides. Our experiments have demonstrated the presence of molecular O_2 at the end of discharge in high-nickel Li-rich layered oxides. This suggests that Li ions cannot smoothly re-enter the TM layer to coordinate with oxygen during discharge, leaving some oxygen species as molecular O_2. Therefore, the issue may lie in the TM layer, specifically at the local honeycomb superstructure.

To detect the honeycomb superstructure distribution, we conducted ^{6}Li solid-state nuclear magnetic resonance (NMR) spectroscopy measurements[150,151]. **Figure 3.8a** and **Table A2** present the ^{6}Li NMR patterns with fitting results. The sharp peak at 0 ppm represents diamagnetic species such as LiOH, Li_2CO_3, and organic lithium salts[152,153]. Two prominent groups of peaks are observed at 500-1000 ppm and 1300-1500 ppm, corresponding to Li in the Li layer (Li_{Li}) and Li in the TM layer (Li_{TM}), respectively. The NMR patterns reveal two distinct peaks at approximately 1300 and 1500 ppm, indicating two different Li environments within the TM layer. Consistent with previous literature[154–156], these peaks are assigned to honeycomb superstructure units for $LiMn_6$ (purple, Li surrounded by six Mn) and $LiNiMn_5$ (blue, Li surrounded by one Ni and five Mn), respectively. The corresponding atomic structures are plotted in **Figure 3.8b**. Interestingly, although all materials show similar total lithium content in the TM layer, the local lithium environments differ. Specifically, NMR patterns reveal a gradual increase in the intensity of peaks corresponding to $LiNiMn_5$ units, while the intensity of peaks for $LiMn_6$ units decreases from N28 to N40. Fitting results show that the ratio of $LiNiMn_5/(LiNiMn_5 + LiMn_6)$ increases progressively: 0.183 for N28, 0.373 for N32, 0.540 for N36, and 0.613 for N40 (**Figure 3.8c**). Thus, the varying Ni/Mn ratios in Li-rich layered oxides affect the type of superstructure units within the TM layer. As nickel content increases, the Li-rich oxide exhibits more $LiNiMn_5$ units, replacing $LiMn_6$ units.

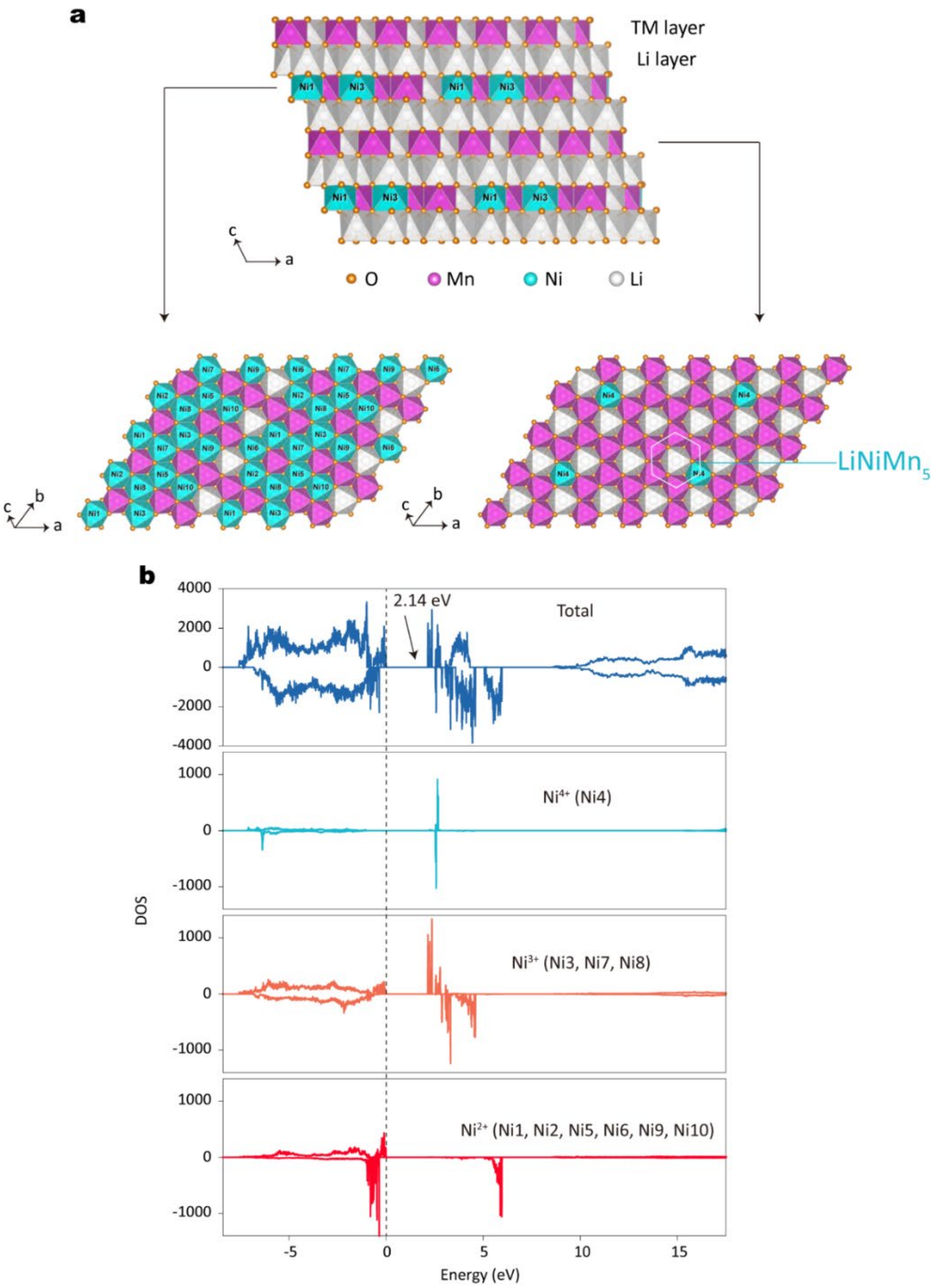

Figure 3.9 (a) Atomic structure model (top panel) and $LiNiMn_5$ honeycomb superstructure within TM layers (bottom panel). (b) The Total DOS and corresponding pDOS of Ni^{2+}, Ni^{3+}, and Ni^{4+} from the DFT calculation. The Fermi level is set to 0 eV and shown with a dashed line.

Since it is difficult to detect the $LiNiMn_5$ superstructure units in conventional Li-rich cathodes (e.g., $Li_{1.2}Ni_{0.2}Mn_{0.6}O_2$), the potential impact of this unit on electrochemistry may have been overlooked. To understand the formation mechanism of $LiNiMn_5$, we conducted density functional theory (DFT) calculations. We chose $Li_{44}Mn_{18}Ni_{10}O_{72}$ ($Li_{1.22}Mn_{0.50}Ni_{0.28}O_2$, $LiNiMn_5$ within the TM layer) as the structural model (**Figure 3.9a**). By calculating the spin density of all atoms, we confirmed their valence states. The calculations show Mn with +4 valence state, Ni with +2, +3, and +4 valence states, and O with -2 valence state. Importantly, Ni occurs exclusively as Ni^{4+} within the highly symmetric $LiNiMn_5$ units, whereas Ni^{2+} or Ni^{3+} are identified in more Ni-rich local configurations. Note that we have calculated the oxidation state of Ni in the $LiNiMn_5$ configuration without a priori assumptions on the Ni oxidation state. The relaxed structure shows that Ni possesses the oxidation state +4. In addition, we have calculated models with the same overall composition but without the $LiNiMn_5$ configuration (always without assuming the oxidation state a priori), in which we find that Ni has an oxidation state lower than +4. Based on that we conclude the $LiNiMn_5$ configuration stabilize Ni in the oxidation state +4 in the structure. In addition, these findings are supported by the density of states (DOS) analysis (**Figure 3.9b**). The detailed calculation processes are described in the Experimental section. Consequently, we have identified, for the first time, that the valence state of Ni is crucial for the formation of $LiNiMn_5$ units in layered Li-rich cathodes.

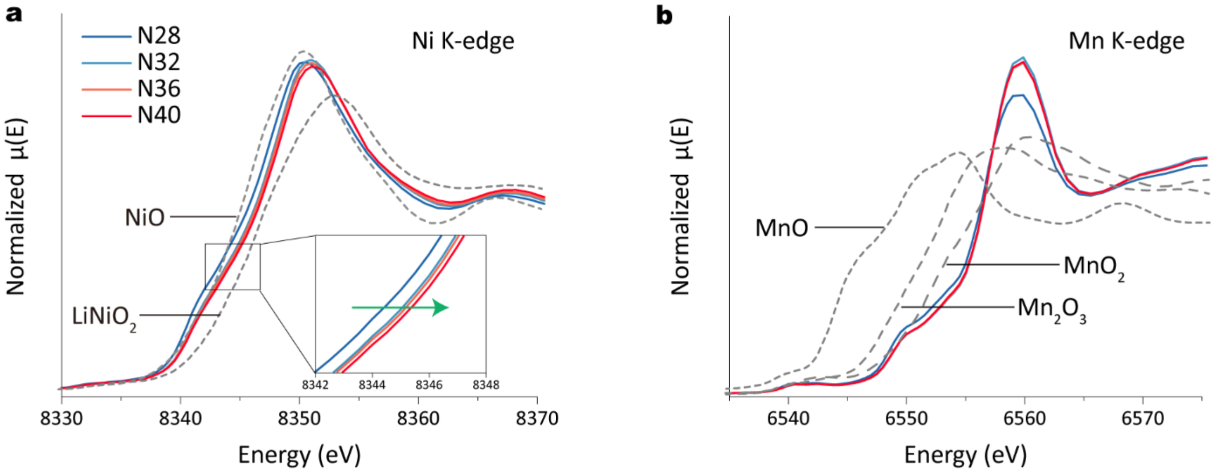

Figure 3.10 Normalized XAS Ni (a) and Mn (b) K-edge XANES of N28, N32, N36, and N40 electrodes. The XAS data are collected in transmission mode.

To confirm the Ni valence state changes in these cathodes, we conducted XAS measurements. As shown in **Figure 3.10a**, the Ni K-edge spectra shift to higher energy from N28 to N40, indicating an increase in the average Ni oxidation state. In contrast, the Mn K-edge spectra position remain constant for all materials, indicating an Mn^{4+} oxidation state (**Figure 3.10b**). The slight shape changes in the Mn spectra are typically associated with alterations in the local coordination environment around Mn ions. This trend aligns well with previous studies on Li-rich cathodes with varying Ni/Mn ratios. Although the average valence state of Ni is below +3, the presence of Ni^{4+} in localized structures cannot be excluded. While Ni^{4+} is atypical in conventional layered cathodes, its presence in Li-rich cathode systems is plausible due to the lithium excess structural configuration[157]. Consequently, forming $LiNiMn_5$ superstructure units is easier in N40 than in N28, as the higher Ni valence state in N40 allows for more Ni^{4+} to be present.

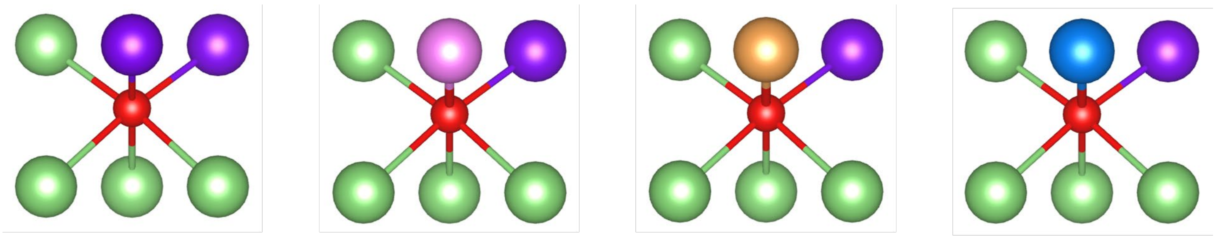

$LiMn_2$-O-Li_3 $\Delta Z = 0$

LiNiMn-O-Li_3 (Ni^{2+}) $\Delta Z = 1/3$

LiNiMn-O-Li_3 (Ni^{3+}) $\Delta Z = 1/6$

LiNiMn-O-Li_3 (Ni^{4+}) $\Delta Z = 0$

Figure 3.11 Schematic of atomic coordination centered on the oxygen atom. According to Pauling's electrostatic valence rule, the stability of a certain coordination configuration is determined by the valence difference between cations and the centered anion.

In addition, Pauling's electrostatic valence principle[158] and semi-quantitative equation[159] (see bellow) can be used to evaluate the possibility of a coordination configuration:

$$\Delta Z = \left| Z_A - \Sigma \frac{Zc}{n} \right|$$

where Z_A is the valence of anion and Zc is the valence of the cations. Number n is the coordination number of the central anion. The summation notation represents summing over all coordinate cations. According to principle of local electrical neutrality, a structure may become unstable if $\Delta Z > 0$. In Li-rich cathodes, three Li ions in the Li layer are consistently coordinated with the central oxygen atom, while the coordination environments of cations in the transition metal layer may have different combinations. As shown in **Figure 3.11**, the most common $LiMn_6$ superstructure units, equivalent to $LiMn_2$-O-Li_3, exhibit a stable state with $\Delta Z = 0$. Similarly, $LiNiMn_5$ units (LiNiMn-O-Li_3) also demonstrate $\Delta Z = 0$, attributed to the presence of Ni^{4+} rather than Ni^{2+} ($\Delta Z = 1/3$) and Ni^{3+} ($\Delta Z = 1/6$). This elucidates why prior investigations failed to detect nickel within Li_2MnO_3-like domains, given that the possibility of the presence of Ni^{4+} in $LiNiMn_5$ superstructure units has been previously overlooked[159,160].

Additionally, previous theoretical calculations[160] indicate that the Li_4MnNi-coordinated O, referred to as $LiNiMn_5$ in our work, exhibits significantly lower cationic and anionic redox activity compared to $LiMn_6$ units, indicating limited electrochemical activity. Moreover, lithium ions move from one octahedral site to another, passing through an intermediate tetrahedral site where they encounter strong repulsion from nearby transition metals. The associated activation barriers for lithium movement with Ni^{4+}, Ni^{3+} and Ni^{2+} are 490, 310, and 210 meV, respectively[161]. These theoretical findings imply that $LiNiMn_5$ may impede the extraction/insertion of lithium ions. During charging/discharging, Li-rich cathodes experience a cationic–anionic redox inversion, leading to electrochemical asymmetry[140]. As a consequence, at low discharge potentials, some Li ions fail to return to the TM layer to coordinate with oxygen, resulting in an incomplete oxygen redox process. This analysis is consistent with the findings from O K-edge SXAS and RIXS experiments described above.

Combining all the results described above, a clear correlation between the incomplete oxygen redox activity and honeycomb superstructure units can be established. In Li-rich cathodes, as the nickel valence state increases (reflecting increased nickel content from N28 to N40), cathodes exhibit a rise in $LiNiMn_5$ at the expense of $LiMn_6$ units. Cathodes with higher $LiNiMn_5$ content exhibit limited electrochemical activity, resulting in incomplete oxygen redox reactions (retention of molecular O_2) at a low potential of 3.3 V, thereby leading to decreased capacity. In contrast, Li-rich cathodes with less $LiNiMn_5$, such as N28, demonstrate enhanced oxygen redox reversibility, showing higher discharge capacity. To advance the commercialization of Li-rich cathodes, research into high-nickel content is crucial. Our findings indicate that the primary issue with high-nickel Li-rich cathodes is their incomplete oxygen redox reaction, leading to lower specific discharge capacity. This incomplete reaction is mainly due to an excess of $LiNiMn_5$ superstructure units in the TM layer. To reduce these units and to improve the reversibility of the oxygen redox reaction in high-nickel systems, the overall Ni valence state in Li-rich cathodes must be decreased. Our next focus will be on tailoring superstructure units to enhance the oxygen redox activity, thereby increasing capacity in high-nickel Li-rich cathodes.

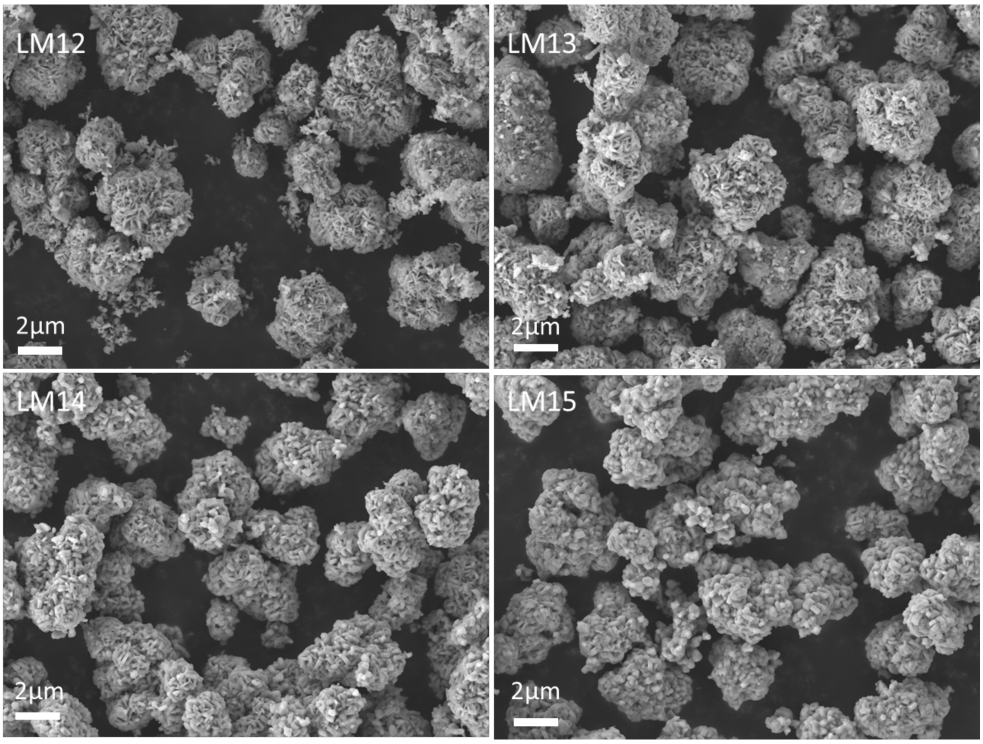

Figure 3.12 SEM images of LM12, LM13, LM14, and LM15 powders.

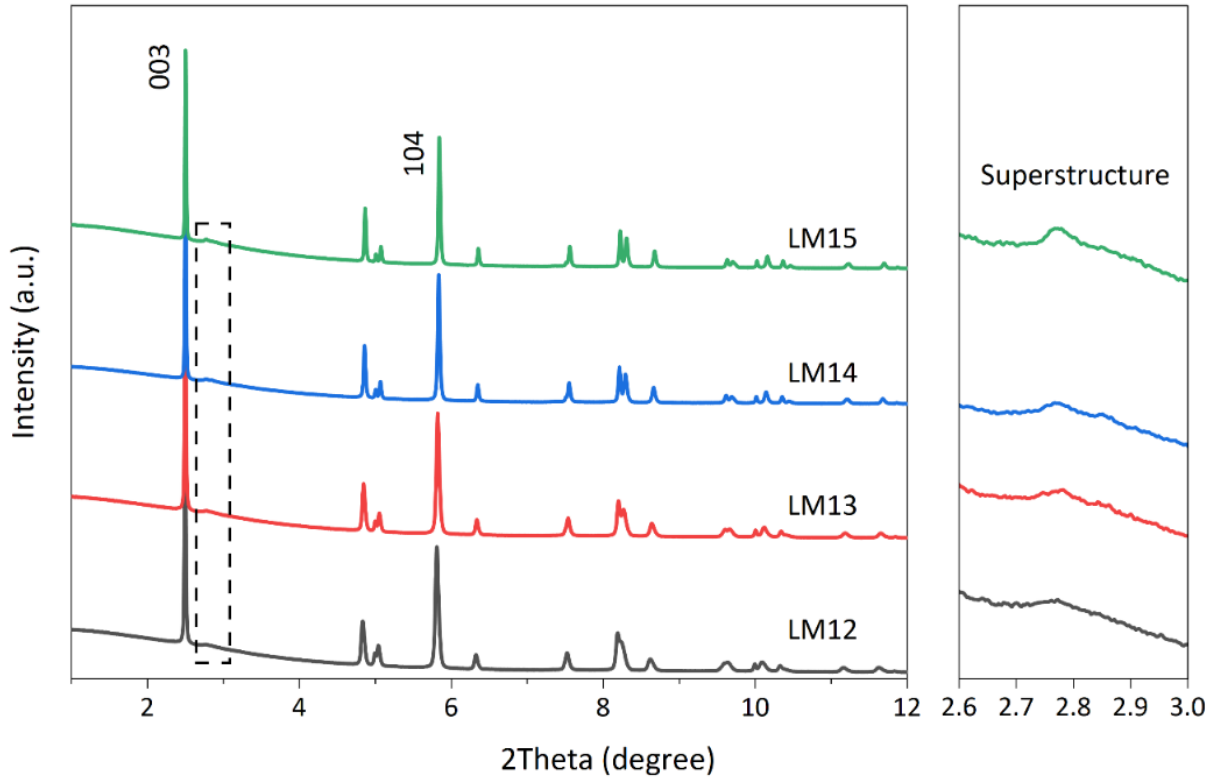

Figure 3.13 SXRD patterns for LM12, LM13, LM14, and LM15 powders. The wavelength was 0.2073 Å.

We propose a practical solution: reducing the lithium content to lower the Ni valence state and thus tailor the $LiNiMn_5$ superstructure units. During the synthesis, we varied the lithium content and the ratio of TM precursors. Specifically, we used Li/TM ratios of 1.2, 1.3, 1.4, and 1.5 based on the N36 precursor $Ni_{0.45}Mn_{0.55}(OH)_2$. The resulting chemical formulas are $Li_{1.09}Ni_{0.41}Mn_{0.50}O_2$ (LM12), $Li_{1.13}Ni_{0.39}Mn_{0.48}O_2$ (LM13), $Li_{1.17}Ni_{0.37}Mn_{0.46}O_2$ (LM14), and $Li_{1.20}Ni_{0.36}Mn_{0.44}O_2$ (LM15). It is important to note that LM15 is equivalent to the N36 sample mentioned earlier. Inductively coupled plasma-optical emission spectroscopy (ICP–OES) results confirm that the Li/TM molar ratios are consistent with the design values, except for some lithium evaporation at high temperatures, as shown in **Table A5**. SEM images (**Figure 3.12**) reveal that the thickness of primary particles increases with higher lithium content. This is likely because sufficient lithium content promotes further crystalline fusion of the material. As shown in **Figure 3.13**, LM12, LM13, LM14, and LM15 maintain a layered phase with space group *R-3m* without impurities. The broad diffraction peaks at 2*θ* values of 2.7-3.1° indicate honeycomb Li/TM ordering (*C2/m* space group) within the TM layer. From the enlarged view on the right, the diffraction intensity corresponding to the superstructure decreases from LM15 to LM12. This indicates a strong correlation between the superstructure and the lithium content, with lower lithium content leading to a lower probability of forming superstructure domains.

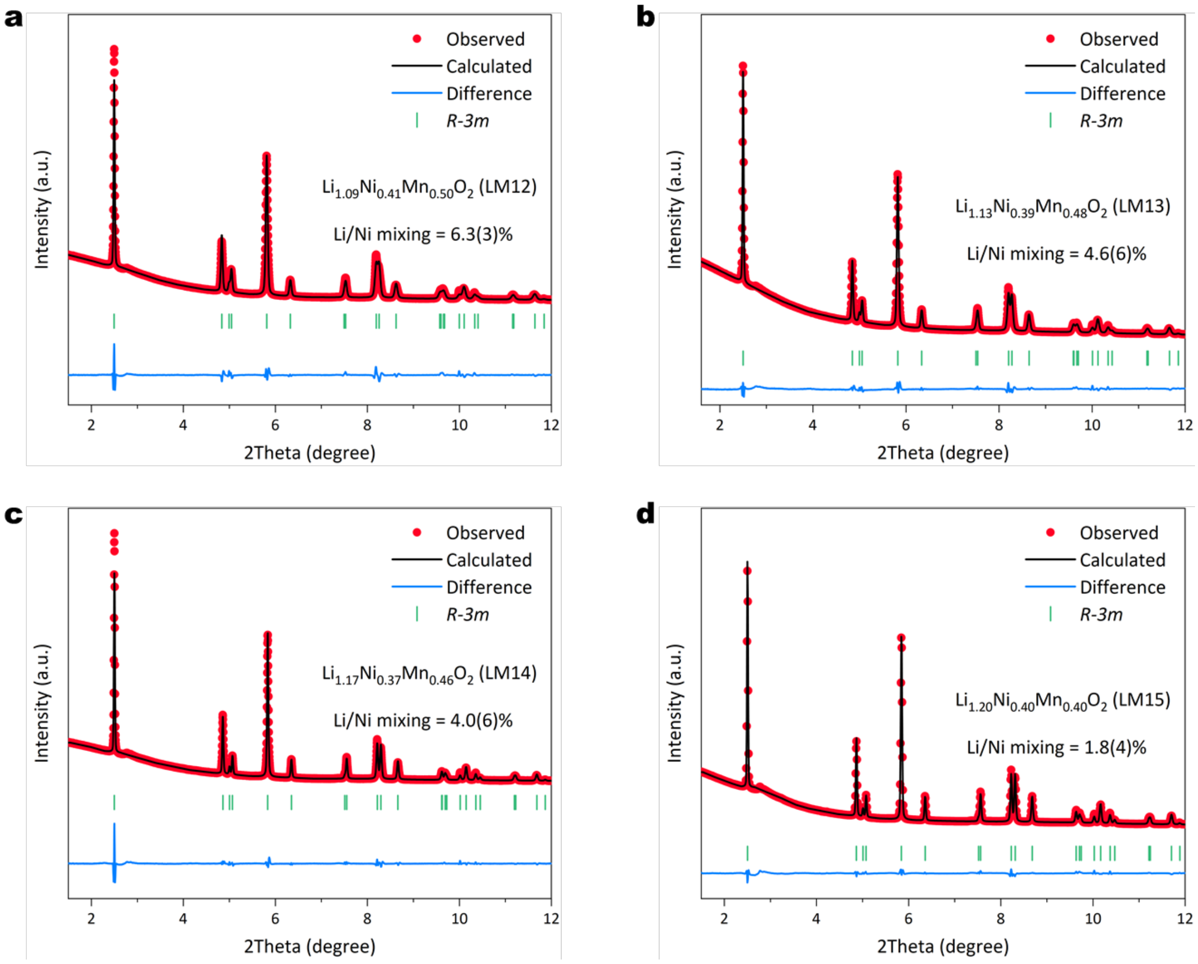

Figure 3.14 SXRD patterns and corresponding refinement results for LM12 (a), LM13 (b), LM14 (c), and LM15 (d) powders. The wavelength was 0.2073 Å.

We conducted SXRD refinement using the *R-3m* phase as the structural model, with the results detailed in **Figure 3.14** and **Table A6**. As lithium content decreases, the lattice parameters *a* and *c* gradually increase. Specifically, the lattice parameters *a* are 2.8593(1), 2.8649(1), 2.8717(2), and 2.8787(1) Å for LM15, LM14, LM13, and LM12, respectively. The corresponding lattice parameter *c* values are 14.2241(8), 14.2398(8), 14.2519(24), and 14.2659(15) Å. These changes are primarily due to the gradual decrease in *C2/m* phase domains from LM15 to LM12. Furthermore, Li/Ni mixing shows increasing disorder from LM15 to LM12, with LM15 exhibiting a minor disorder value of 1.8(4)% compared to higher value of 6.3(3)% for LM12.

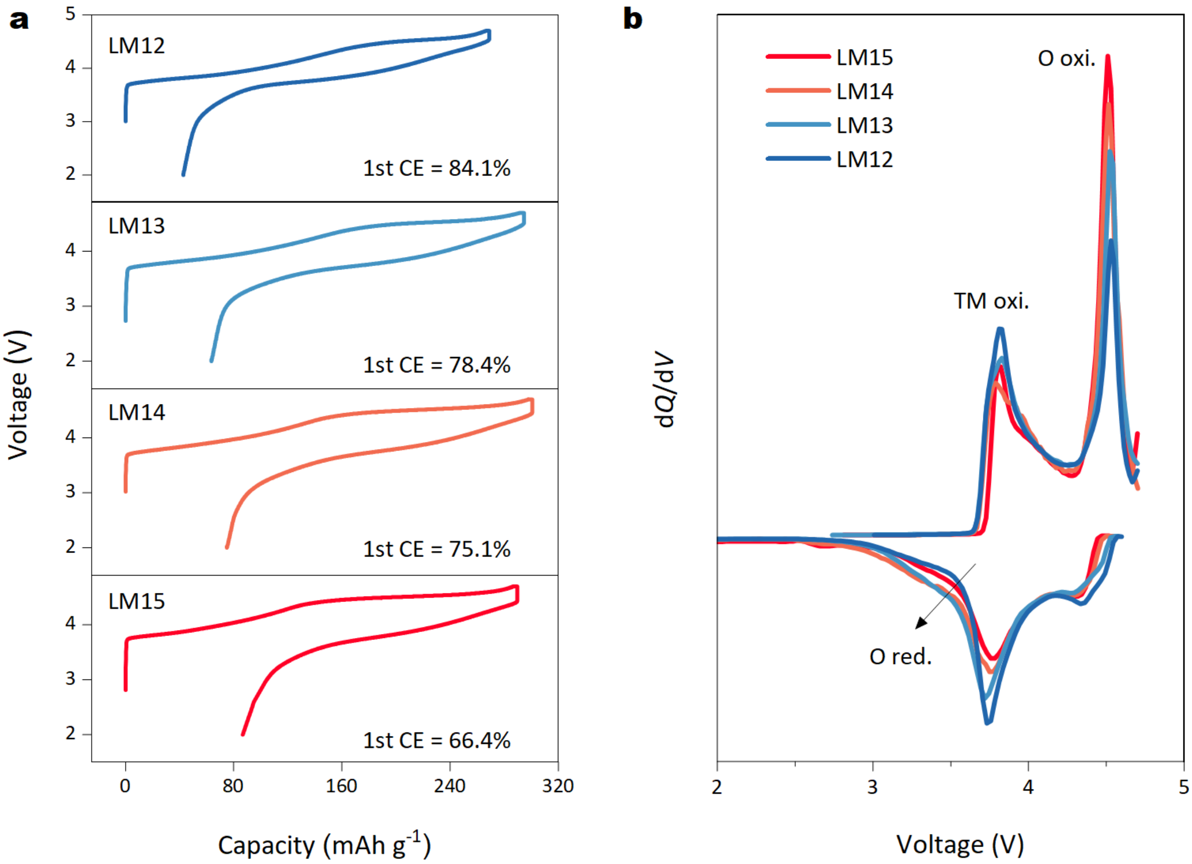

Figure 3.15 (a) The charge/discharge curves and (b) corresponding dQ/dV curves of LM12, LM13, LM14, and LM15 in the first cycle in the voltage range of 2.0-4.7 V at C/10 at 25 °C. 1C is defined as 200 mA g^{-1}.

We then evaluated the electrochemical performance of these cathodes. As shown in **Figure 3.15a,** all cathodes exhibit typical Li-rich charging curves. However, there are clear differences in the lengths of the cation redox region and the oxygen redox region, as confirmed by the dQ/dV curves in **Figure 3.15b**. From LM15 to LM12, the oxygen redox contribution in the Li-rich cathode gradually decreases, while the cation redox contribution gradually increases. In addition, the lower lithium content also reduces the total charging capacity. For example, LM12 and LM15 deliver charging capacities of 268.9 and 298.7 mAh g^{-1} at C/10, respectively. As previously noted, Li-rich cathodes with a higher nickel content suffer from incomplete oxygen redox processes. Consequently, LM15 delivers a capacity of 198.4 mAh g^{-1}, corresponding to an ICE of 66.4%. Although LM12 has a lower charging capacity, it delivers a higher discharge capacity of 226.3 mAh g^{-1} with an ICE of 84.1%. These inverse changes in discharge capacity are due to more reversible oxygen redox activity at low potential, as indicated by the arrow in **Figure 3.15b**. **Figure A1** presents the cycle performance at 2.0-4.7 V at a C/3 rate over 100 cycles. It is important to note that the capacity retention calculation is based on the initial capacity; therefore, the 94.7% retention for LM15 is not necessarily superior to the others.

Among LM12, LM13, and LM14 cathodes, LM13 delivers 231.1 mAh g^{-1} at C/10 and retains an excellent cycle life with 91.2% capacity retention after 100 cycles at C/3. Considering both discharge capacity and cycle stability, LM13 is selected as the optimized cathode for further discussion. The PDF patterns of both cathodes are shown in **Figure A2**. LM13 shows a higher intensity of the second PDF peaks corresponding to TM-TM pairs compared to LM15 (indicated by the arrow). It suggests LM13 exhibits more *R-3m* than *C2/m* domains, which agrees with above SXRD analysis. Additionally, both cathodes exhibit a uniform distribution of Ni, Mn, and O, confirmed by transmission electron microscopy (TEM) energy dispersive X-ray spectroscopy (EDS) mapping images (**Figure A3**).

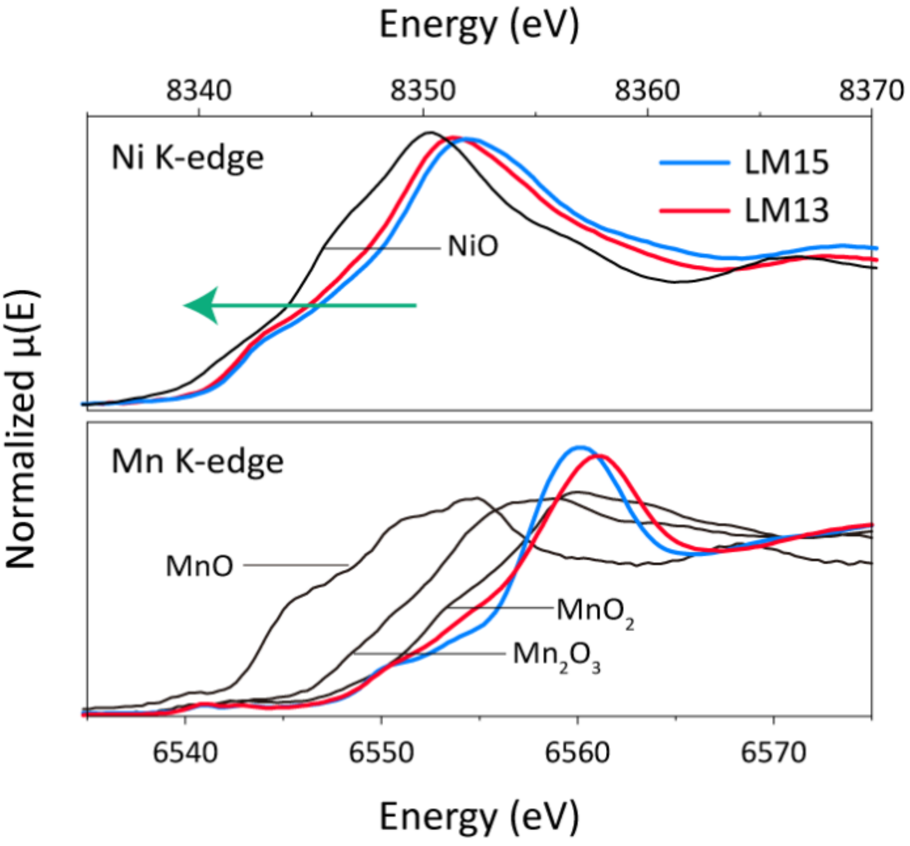

Figure 3.16 Normalized XAS Ni (top) and Mn (bottom) K-edge XANES of LM13 and LM15 in the pristine state. The XAS data are collected in transmission mode.

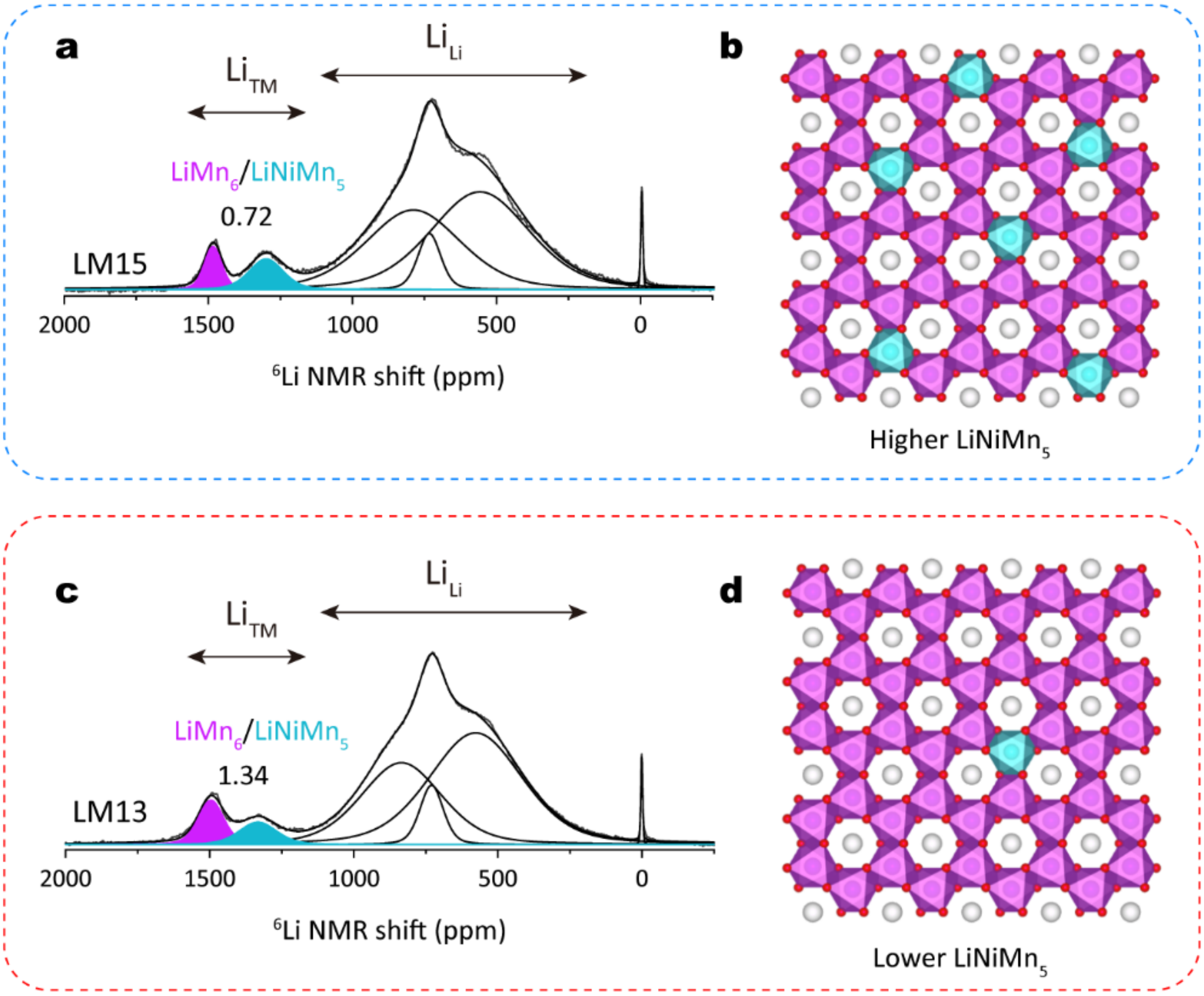

Figure 3.17 ^{6}Li MAS NMR spectra and fitting results and the corresponding schematic of in-plane ordering of Li (gray) and Mn (purple octahedra) or Ni (blue octahedra) within TM layers forming $LiMn_6$ and $LiNiMn_5$ superstructure units for (a-b) LM13 and (c-d) LM15.

To reduce the formation of $LiNiMn_5$ superstructure units, the valence of Ni must be decreased, as indicated by our theoretical studies. To confirm these changes in LM13 and LM15 cathode, XAS measurements were conducted. **Figure 3.16** shows that the Ni K-edge spectra shift to lower energy from LM15 to LM13, indicating a decrease in the average Ni oxidation state. The Mn XAS spectra show no significant energy shift, aside from slight shape changes. These results confirm that reducing the lithium content effectively lowers the valence state of Ni while maintaining the Mn valence state. To investigate the distribution of honeycomb superstructure units, we conducted ^{6}Li NMR measurements of LM13 and LM15. Compared to LM15, LM13 exhibits a lower NMR peak intensity at approximately 1300 ppm, indicating fewer $LiNiMn_5$ units (**Figure 3.17**). The NMR fitting results (**Table A7**) show that LM13 has a relative $LiMn_6$/$LiNiMn_5$ peak ratio of 0.72, compared to 1.34 for LM15. These findings demonstrate the effectiveness of our lithium adjustment in tailoring the superstructure units. To better understand the distribution of these honeycomb superstructures, we developed a structural model shown in

Figure 3.17b-d. Overall, through our comprehensive analyses (including SXRD, PDF, XAS, and NMR), we have successfully tuned the composition and content of the honeycomb superstructure units and introduced an optimal amount of Li/Ni mixing in the LM13 cathode. This adjustment enhances the cationic redox activity, improving structural stability, while mitigating the instability caused by the anionic redox activity at high voltages. Additionally, moderate Li/Ni disordering promotes structural reversibility due to the pillar effect. This approach offers a practical and straightforward solution for industrial applications compared to other complex modification processes.

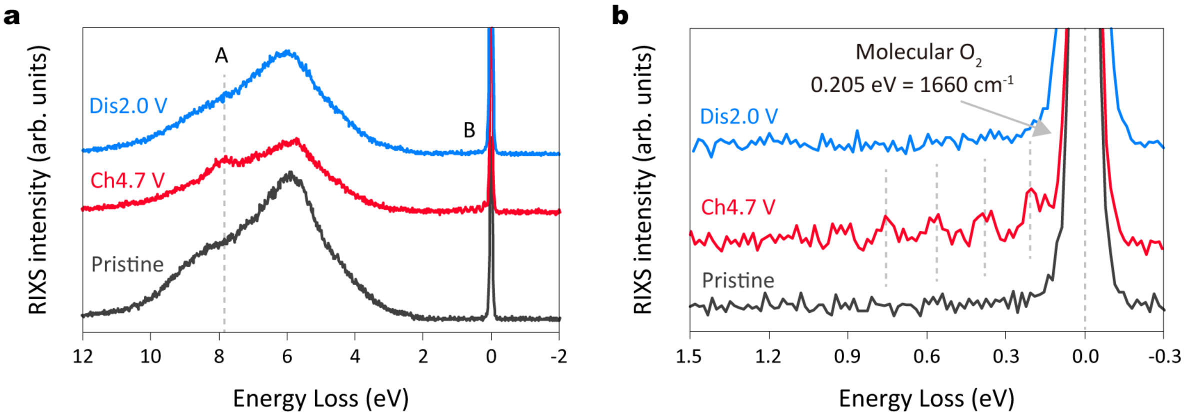

Figure 3.18 (a) The O K-edge RIXS spectra collected at an excitation energy of 531 eV at pristine, charged to 4.7 V, and discharge to 2.0 V states in the first cycle and (b) an enlarged view of the elastic region (0-1 eV) for LM13.

In **Figure 3.15a**, LM13 exhibits a longer sloping part (below 4.45 V) and a shorter oxygen redox plateau than LM15, reflecting differences in superstructure contents. Despite a slight trade-off in charge capacity due to lower lithium content, LM13 demonstrates a notable capacity of 231.1 mAh g^{-1} with an ICE of 78.4%. This surpasses the 199.0 mAh g^{-1} of LM15 (ICE of 69.8%). The dQ/dV curves in **Figure 3.15b** highlight the significant difference in discharge capacity, attributed to the co-contribution of nickel redox and oxygen redox activity (especially at a low potential of 3.3 V, indicated by the arrow). This modulation of cationic and anionic redox contributions aligns precisely with the impact of superstructure content and units in Li-rich layered oxides. To confirm the reversibility of the oxygen redox process in the LM13 cathode, we conducted O K-edge RIXS measurements. **Figure 3.18** shows a clear molecular O_2 signature during charging, indicating oxygen oxidation. In contrast to LM15 (**Figure 3.7**), no signal is detected at the end of discharge for LM13. The enlarged view of the elastic region (0-1 eV) in **Figure 3.18b** further supports these observations. This confirms the complete oxygen redox process in LM13 after adjusting the superstructure units. Note that the relatively lower oxygen redox signal in LM13 is attributed to the reduced superstructure content, consistent with the SXRD and PDF analyses described above.

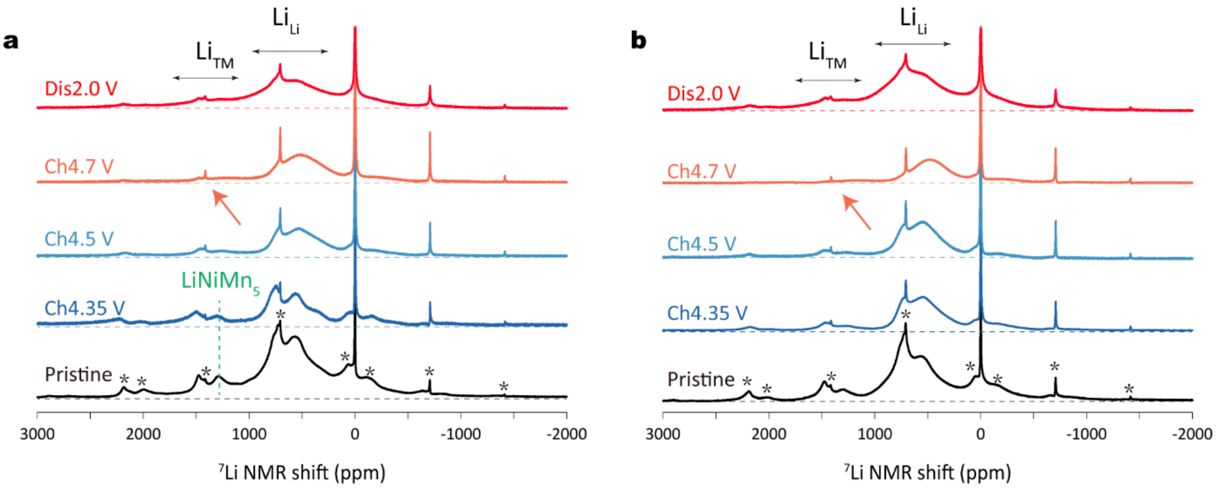

Figure 3.19 ^{7}*Li MAS NMR spectra of LM15 (a) and LM13 electrodes (b) in the pristine state and after charging to 4.35, 4.5, and 4.7 V, and discharging to 2.0 V in the first cycle. Spinning sidebands are marked by an asterisk.*

To track the evolution of the local lithium environments during charge/discharge, ex-situ ^{7}Li NMR spectroscopy was performed. In **Figure 3.19**, the ^{7}Li NMR results in the pristine state, in agreement with the ^{6}Li NMR measurements described above, confirm fewer $LiNiMn_5$ units in LM13. In the charged state at 4.35 V for LM15, the intensity of the peak corresponding to $LiNiMn_5$ remains unchanged (see green dashed line), indicating minimal changes in the oxidation state of TM ions within $LiNiMn_5$, confirming the presence of Ni^{4+}-stabilized $LiNiMn_5$ units rather than Ni^{2+} or Ni^{3+}. Beyond 4.5 V, the NMR peak broadens due to structural disorder induced by TM ions migration in Li environments, making it challenging to identify specific superstructure units in both cathodes. In the charged state at 4.7 V, some NMR signals persist in the 1300-1500 ppm region in LM15, indicating lithium ions in the TM layers. In sharp contrast, LM13 shows no obvious signal in this region, implying complete lithium-ion removal from the TM layer. Moreover, the lower Li_{Li} (500-1000 ppm) intensity suggests fewer lithium ions in the lattice for LM13. During discharge, the peak intensity increases as lithium ions are inserted, with LM13 exhibiting superior capability for extraction/insertion of lithium ions, as indicated by the higher total peak intensity in both Li_{Li} and Li_{TM}.

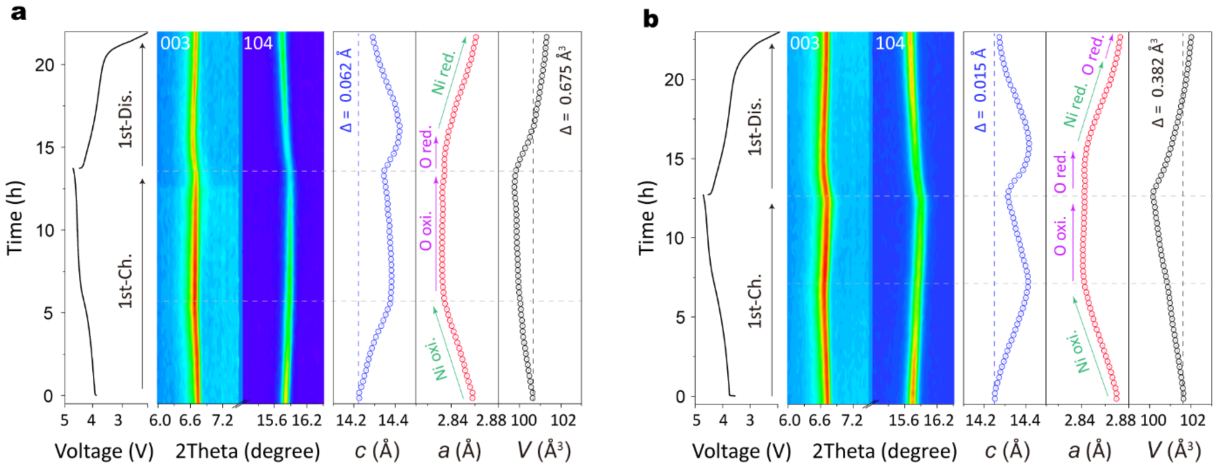

Figure 3.20 In-situ XRD of LM15 (a) and LM13 (b) during the first cycle at C/10 in the voltage range of 2.0-4.7 V at 25 °C. The corresponding lattice parameters and volume were obtained by Rietveld refinement. The in-situ XRD patterns are acquired with an Ag source powder diffractometer in transmission geometry (wavelength of 0.5594 Å).

To capture the structural evolution during the first cycle, in-situ XRD measurements were conducted, and lattice parameters along with volume changes were obtained through Rietveld refinement (**Figure 3.20a-b**). Below 4.45 V (indicated by the horizontal dashed line), both cathodes show an increase in lattice parameter *c*, with the 003 Bragg reflection shifting to lower angles. This shift is attributed to increased electrostatic repulsion accompanying the removal of lithium ions from the Li layer[96]. LM15 exhibits minimal changes in lattice parameter *c* at the oxygen redox plateau, whereas LM13 undergoes significant lattice shrinkage, indicating lithium ions being removed from the TM layer, consistent with previous reports on Li-rich cathodes[162]. The minor changes in LM15, supported by NMR analysis, suggest some lithium ions still reside in the lattice, offsetting the lithium removal effect at the end of the charge. During discharge, both cathodes show similar changes, initially increasing and then decreasing in lattice parameter *c*, implying the insertion of lithium ions into the TM and Li layers, respectively. The lattice parameter *c*, however, cannot revert to the initial position, showing a difference of 0.065 Å. In stark contrast, LM13 demonstrates minor changes in parameter *c*, with a change of only 0.015 Å after one complete cycle.

The lattice parameter *a*, sensitive to the TM-O bond length in the TMO_2 slab, serves as indirect evidence of cationic redox activity[107]. In both cathodes, a linear decrease in the sloping region and minor changes at the oxygen redox plateau are observed, corresponding to nickel oxidation and oxygen oxidation, respectively. During discharge in LM13, lithium ions are inserted into the TM and Li layers, corresponding to oxygen, nickel, and oxygen reduction at high/middle/low potential, respectively (indicated by the coloured arrows). This redox mechanism evolution aligns with other reports on Li-rich cathodes[66,84]. However, in LM15, the absence of oxygen reduction at the low potential of 3.3 V, confirmed by O K-edge XAS and RIXS results, means that changes in the lattice parameter *a* correspond to oxygen reduction followed by nickel reduction during discharge. Additionally, both cathodes experience volume shrinkage after the first cycle, with LM13 exhibiting a smaller volume change of 0.382 Å^3 compared to LM15 (0.675 Å^3). This, combined with the evolution of the lattice parameter *c* described above, confirms the superior structural stability of LM13.

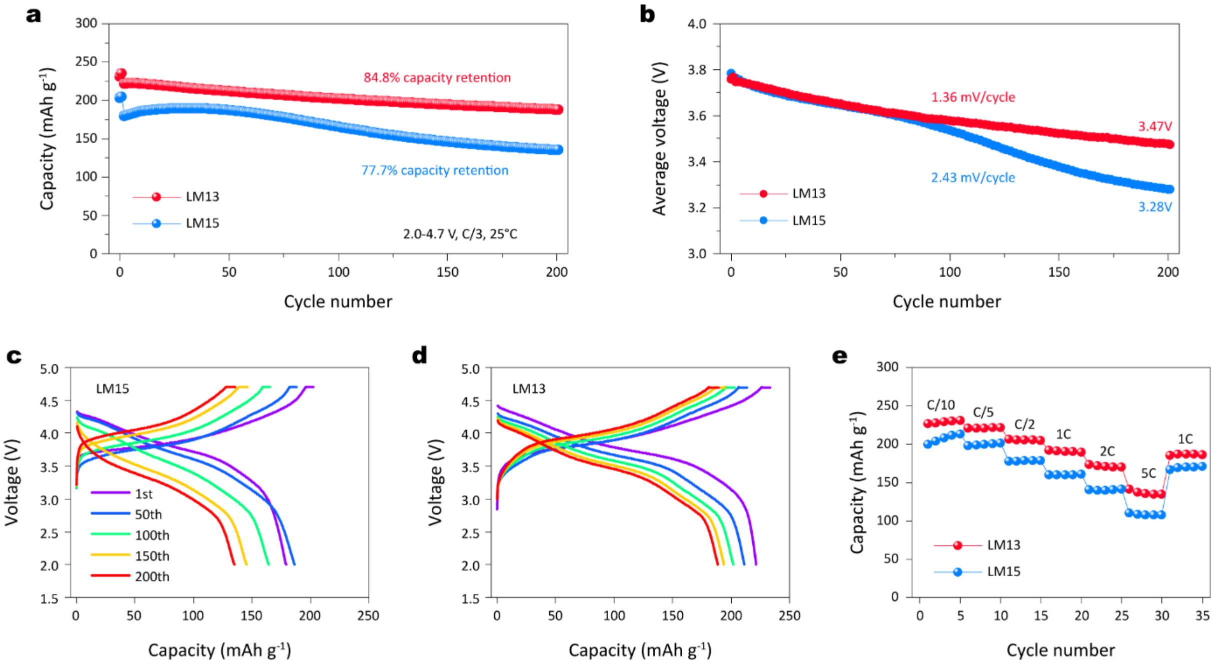

Figure 3.21 (a) Cycling performance and (b) corresponding average discharge voltage curves over 200 cycles at C/3 at 25 °C. Charge/discharge curves (e.g. 1st, 50th, 100th, 150th, and 200th) for LM15 (c) and LM13 (d). Rate capability (e) in the voltage range of 2.0-4.7 V at 25 °C.

Benefiting from the modulation of superstructure content and the introduction of moderate Li/Ni mixing, LM13 delivers both high discharge capacity and excellent cycling stability. As shown in **Figure 3.21a**, LM13 maintains a capacity of 187.7 mAh g^{-1} after 200 cycles at a C/3 rate, with a capacity retention of 84.8%. In contrast, LM15 shows a capacity retention of 71.2% (134.9 mAh g^{-1}). When evaluating Li-rich cathodes, it is more reasonable to assess the average discharge voltage due to the significant challenge of voltage decay. After 200 cycles, LM13 and LM15 exhibit average discharge voltages of 3.47 V and 3.28 V, respectively, corresponding to decreases of 1.36 mV and 2.43 mV per cycle (**Figure 3.21b**). The selected charge/discharge curves clearly illustrate the difference in discharge voltage evolution (**Figure 3.21c-d**). Moreover, LM13 demonstrates superior electrochemical performance even at low current densities of C/10 (**Figure A4**). **Figure 3.21e** highlights the excellent rate capability of LM13, delivering a discharge capacity of 140.9 mAh g^{-1} even at the high rate of 5C. In sharp contrast, LM15 maintains only 109.8 mAh g^{-1} under the same conditions. Overall, these electrochemical performances indicate that the LM13 cathode is superior to the LM15 cathode.

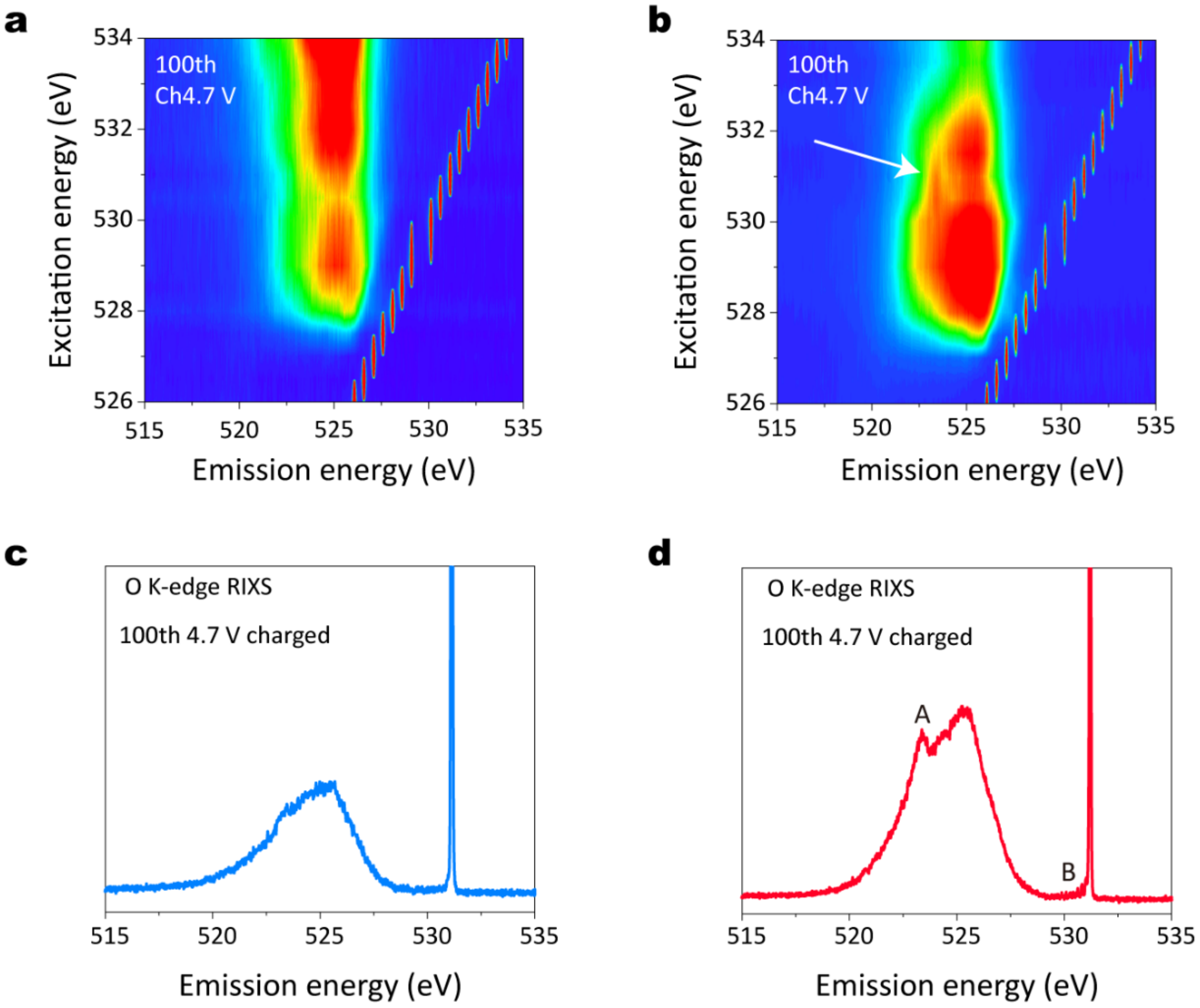

Figure 3.22 The O K-edge RIXS mapping collected with an excitation energy from 526-534 eV after charging to 4.7 V at C/10 after 100 cycles for LM15 (a) and LM13 (b). The O K-edge RIXS spectra collected at an excitation energy of 531 eV in the charged state at 4.7 V after 100 cycles at C/10 for LM15 (c) and LM13 (d).

To verify the oxygen redox stability during long-term cycling, we conducted O K-edge RIXS measurements after 100 cycles at C/10 (approximately 92 days) in the charged state at 4.7 V. As shown in **Figure 3.22a-b**, characteristic features of molecular O_2 are clearly observed in LM13 around an excitation energy of 531 eV and an emission energy of 523.7 eV (indicated by the white arrow), whereas they are barely visible in LM15. Additionally, the O K-edge RIXS spectra collected at an excitation energy of 531 eV (**Figure 3.22c-d**) show that LM13 still exhibits a distinct characteristic peak A (around 523 eV) and a vibrational peak B around the elastic region (530 eV). In sharp contrast, no such signals are detected in LM15. These results indicate that LM13 has higher oxygen redox stability and reversibility, which explains its superior electrochemical performance.

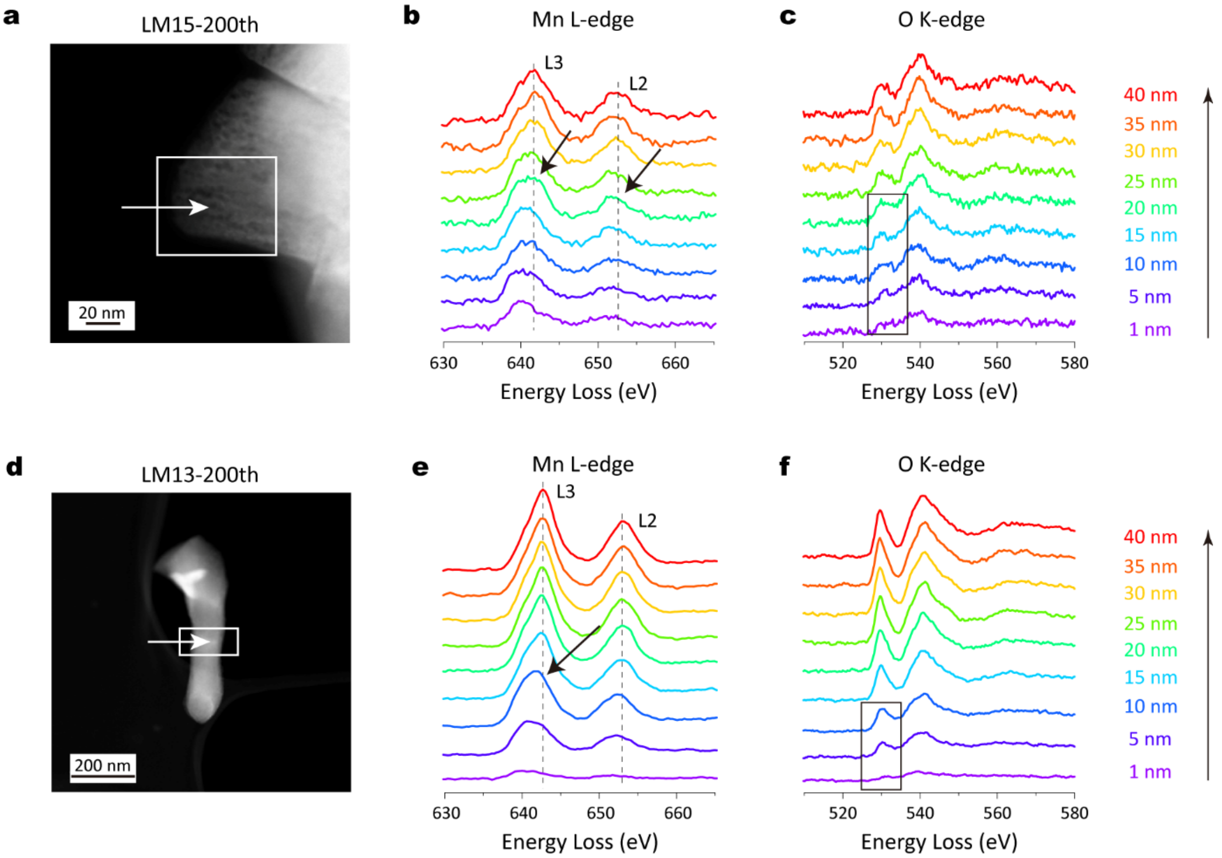

Figure 3.23 EELS line scans at particle surface in the cycled electrode LM15 (a-c) and LM13 (d-f) at C/3 after 200 cycles in the discharged state.

To demonstrate the structural stability of LM13 and LM15, we conducted electron energy loss spectroscopy (EELS) measurements. In the pristine state, as shown in **Figure A5**, the Mn and Ni L-edge spectra of both cathodes remain at the same energy loss position from the surface to the bulk. However, after 200 cycles at a C/3 rate, the Mn L-edge spectra of LM15 exhibit a continuous shift to lower energy within a depth of 20 nm (indicated by arrows in **Figure 3.23b**). This shift suggests a gradual reduction of Mn at the surface[163,164], which is further supported by the fading of the pre-edge peak in the O K-edge spectra (highlighted by the rectangle in **Figure 3.23c).** In contrast, **Figure 3.23e-f** shows that the spectral shifts in LM13 mainly occur up to a depth of 10 nm from the surface. The reproducibility of these results was confirmed by acquiring EELS spectra of the same particle along different directions (**Figure A6**). Additionally, as shown in **Figure 3.23a,** the TEM images LM15 after cycling clearly reveals extensive voiding in LM15, characterized by a high density of voids distributed throughout the particle. In contrast, LM13 exhibits minimal voids, confirmed by the bright particle images (**Figure 3.23d**). These findings indicate that LM13 demonstrates robust surface stability.

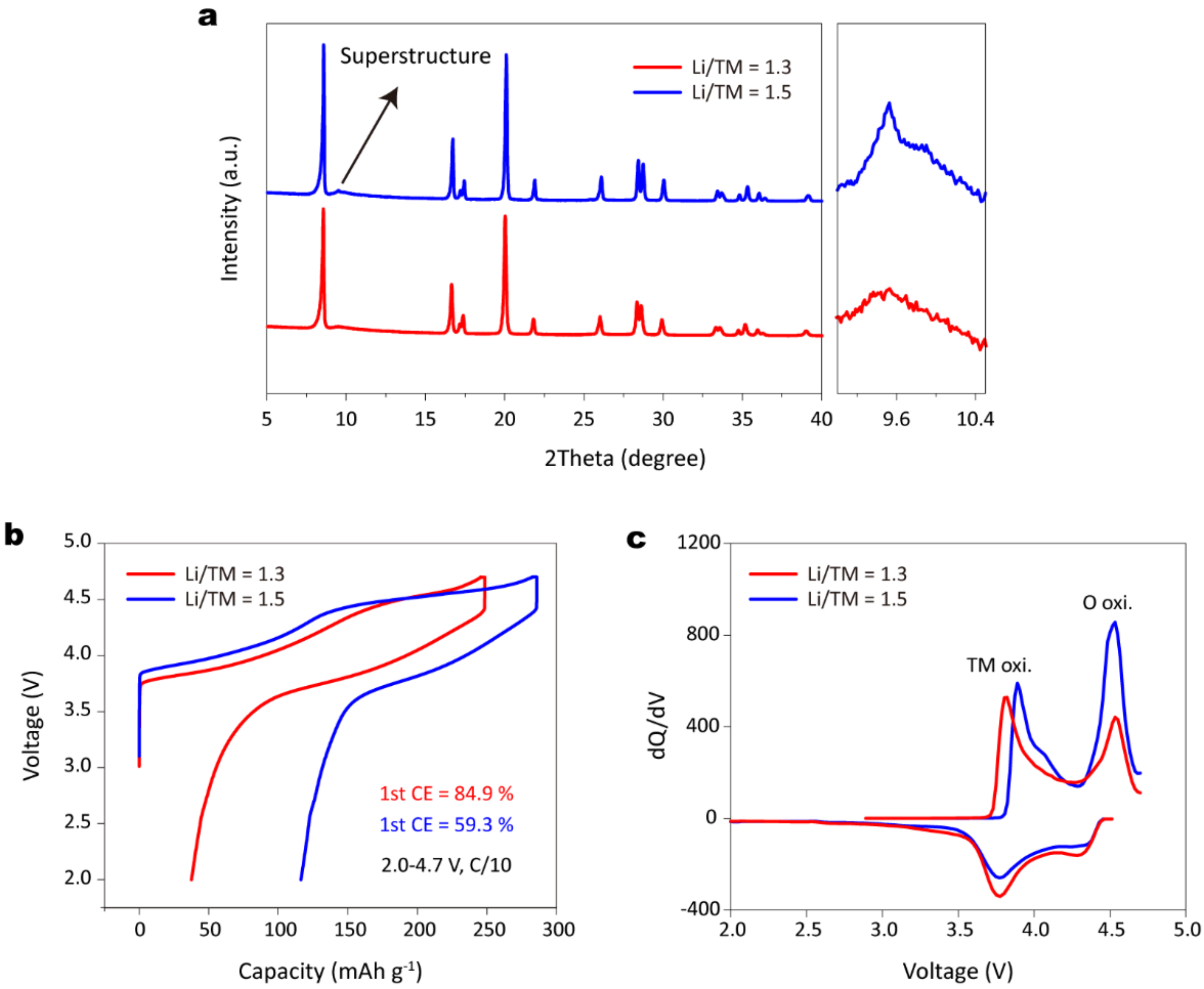

Figure 3.24 (a) XRD patterns for Li/TM = 1.3 and Li/TM = 1.5. The patterns are acquired with a Mo source powder diffractometer in transmission geometry (wavelength of 0.7093 Å). (b) The charge/discharge curves, and (c) corresponding dQ/dV curves in the first cycle.

To validate the effectiveness of our strategy for modulating the honeycomb superstructure in high-nickel Li-rich cathodes, we applied it to $Li_{1.2}Ni_{0.4}Mn_{0.4}O_2$ (50% Ni, 50% Mn in the precursor), now using a Li/TM ratio of 1.3 during synthesis to synthesize $Li_{1.13}Ni_{0.435}Mn_{0.435}O_2$. As shown in **Figure 3.24a**, the XRD patterns confirm that both cathodes exhibit a layered *R-3m* phase without impurities. The enlarged view of the superstructure on the right indicates that Li/TM = 1.3 has lower intensity, suggesting fewer superstructure domains, consistent with the LM13 cathode. In **Figure 3.24b**, the Li/TM = 1.3 cathode delivers a high discharge capacity of 211.0 mAh g^{-1} at C/10, compared to 171.5 mAh g^{-1} for the pristine Li/TM = 1.5 cathode. Additionally, Li/TM = 1.3 shows an initial coulombic efficiency (ICE) of 84.9%, higher than the 59.3% of Li/TM = 1.5. These differences in capacity are mainly attributed to the modulation of the cation and oxygen redox contributions, as illustrated in the dQ/dV curves in **Figure 3.24c**. Due to the stability difference between cation and oxygen redox activity, Li/TM = 1.3, with higher cation redox and lower oxygen redox contributions, exhibits superior and stable electrochemical performance. Overall, our results confirm that adjusting lithium content is an effective and straightforward approach to enhancing the discharge capacity of high-nickel Li-rich cathodes.

3.4 Conclusion

In summary, using a combination of spectroscopic techniques, DFT calculations, and comprehensive electrochemistry analysis, we have successfully elucidated the origin of the $LiNiMn_5$ honeycomb superstructure units and its influence on the electrochemistry, particularly oxygen redox activity in Li-rich cathodes. Our findings reveal the presence of two distinct honeycomb superstructure units in the TM layers, namely $LiMn_6$ and $LiNiMn_5$. As the nickel valence state increases (with consistent Mn valence), cathodes tend to exhibit a higher proportion of $LiNiMn_5$ unit at the expense of $LiMn_6$ units in the cathode. Notably, for the first time, we identify that the $LiNiMn_5$ unit is exclusively stabilized by Ni^{4+} and not by Ni^{2+} or Ni^{3+}. Unlike conventional $LiMn_6$ units, $LiNiMn_5$ impedes the extraction/insertion of lithium ions, resulting in an incomplete oxygen redox process at a low potential of 3.3 V and retaining molecular O_2 in the lattice at the end of discharge. Consequently, cathodes with a higher proportion of $LiNiMn_5$ units exhibit reduced discharge capacity. Guided by theoretical insights, we propose a practical approach to inhibit $LiNiMn_5$ superstructure units by reducing the lithium content during synthesis, resulting in enhanced electrochemical performance with reversible oxygen redox activity. The optimized cathode ($Li_{1.13}Ni_{0.39}Mn_{0.48}O_2$) demonstrates a remarkable capacity of 231.1 mAh g^{-1}, surpassing the 199.0 mAh g^{-1} of the pristine cathode ($Li_{1.20}Ni_{0.36}Mn_{0.44}O_2$) at C/10, and also shows strongly suppressed voltage fade. Our work not only provides a novel understanding of honeycomb superstructure units but also reveals the close relationship between superstructure units and oxygen redox activity. However, it is essential to acknowledge certain limitations of our study. While the modification with lower lithium content results in fewer $LiNiMn_5$ superstructure units, other parameters such as superstructure content, Li/Ni disordering, and even stacking faults also undergo changes. These parameters lie beyond the scope of the current study. Therefore, future research endeavours may focus on exploring these parameters and achieving a balance to enable high-energy-density, high-nickel Li-rich layered oxides.

Chapter 4 Stable oxygen redox chemistry for high-performance lithium-ion layered oxides

4.1 Introduction

Lithium-ion batteries (LIBs) are increasingly crucial due to the growing demand in the portable electronics and electric vehicle markets[165,166]. The cathode, a critical component of LIBs, significantly determines both performance and cost[167]. Consequently, current research focuses on improving cathode performance while reducing material costs. In this context, high-nickel (Ni) layered oxides (with Ni content over 80%)[43,168] have garnered considerable attention, as their higher Ni content enhances discharge capacity. However, high-Ni cathodes face challenges such as low thermal stability, rapid structural degradation, and poor cycle life[169]. Additionally, their synthesis often requires a pure oxygen atmosphere and stringent storage conditions, which substantially increase production costs[170]. Meanwhile, researchers are also investigating lithium-rich (Li-rich) layered oxides, with the chemical formula $Li_{1+x}TM_{1-x}O_2$ (where TM denotes transition metals)[90,171]. These cathodes offer increased capacity through additional oxygen redox activity at high voltages. However, instability in oxygen redox processes can lead to voltage hysteresis, voltage decay, and oxygen gas release[36,66]. Until these issues are resolved, the practical application of Li-rich cathodes remains uncertain.

Recently, attention has shifted to low-Ni layered oxides[172,173]. Although these cathodes typically have lower capacity at a 4.3 V cut-off voltage, this can be partially compensated by operating at higher voltages (>4.5 V). Low-Ni cathodes present significant cost advantages over their high-Ni counterparts, as they can be synthesized in an air atmosphere and stored under less stringent conditions. Additionally, the reduced Ni content and increased manganese (Mn) content further lower material costs. However, challenges such as severe intrinsic Li/Ni mixing and structural instability at high voltages degrade battery performance and impede commercial development[174,175]. Introducing cobalt (Co) elements into cathodes[176–178] has proven effective in addressing these issues. However, Co is scarce, expensive, and poses geopolitical risks, making its elimination crucial for advancing high-voltage, low-Ni cathodes. Various strategies[179–181], including doping, surface coating and chemical composition design, have been proposed to address these issues. Notably, Zhang et al.[182] developed a complex, concentrated, stoichiometric layered cathode ($LiNi_{0.5}Mn_{0.43}Ti_{0.02}Mg_{0.02}Nb_{0.01}Mo_{0.02}O_2$) with high specific energy, excellent thermal stability, and superior cycling performance under high-voltage operation. Despite these advances, low-Ni cathodes remain uncompetitive. Their discharge capacity, even at high voltages, is still below 190 mAh g^{-1}, which is insufficient for future high-energy-density LIBs. Additionally, maintaining structural stability in highly de-lithiated states remains a significant challenge. Finally, designing or modifying these cathodes for cost-effective industrial-scale production requires further consideration.

In this chapter, we present a high-performance, cost-effective lithium-ion layered oxide cathode, $Li_{1.05}Ni_{0.43}Mn_{0.52}O_2$ (LN43). Advanced characterization techniques reveal that 12.7(6) wt.% of Li_2MnO_3-like domains are integrated into the material, with some Ni ions occupying lithium (Li) layers to form a localized Ni-pinned honeycomb structure. Theoretical calculations indicate that these Ni-pinned honeycomb structures enhance the energy barrier for oxygen vacancy formation and alter the local electronic structure of oxygen, thereby stabilizing oxygen redox activity at high voltages. Additionally, the Ni ions within the Li layers primarily migrate in-plane rather than out-of-plane, preserving the integrity of the Ni-pinned honeycomb structure during repeated cycling. As a result, LN43 delivers a high capacity of 202.2 mAh g^{-1}, corresponding to an energy density of 782.8 Wh kg^{-1} (based on cathode active materials), at a C/10 within a voltage range of 2.5-4.55 V. After 200 cycles at a C/3 rate, LN43 retains 96.3% capacity and 93.3% energy. Furthermore, even when cycled within a wider voltage range of 2.0 to 4.7 V, LN43 maintains 95.3% capacity after 150 cycles at a C/3 rate. More importantly, the LN43 cathode does not require the use of expensive Co elements, nor does it necessitate post-treatment processes, thereby facilitating cost-effective production on an industrial scale.

4.2 Experimental

4.2.1 Materials synthesis

$Li_{1.05}Ni_{0.43}Mn_{0.52}O_2$ (LN43) and $LiNi_{0.5}Mn_{0.5}O_2$ (NM50) cathodes were synthesized using a hydroxide co-precipitation method followed by a solid-state reaction. Initially, a 2.0 M aqueous solution containing $NiSO_4 \cdot 6H_2O$ (≥98%, Sigma–Aldrich) and $MnSO_4 \cdot H_2O$ (≥98%, Sigma–Aldrich) was prepared, with molar ratios of 9:11 for LN43 and 1:1 for NM50. This solution was combined with a 4.0 M NaOH solution (≥98%, Sigma–Aldrich) and a 0.5 M $NH_3 \cdot H_2O$ solution (28%-30%, Sigma–Aldrich) fed into a 1 L batch reactor. Both the aqueous TM solution and the $NH_3 \cdot H_2O$ solution were introduced at the same flow rate, while the pH was maintained at 11.0 ± 0.2 by adjusting the feed rate of the NaOH solution. The reaction was conducted at a temperature of 50 °C under a N_2 atmosphere. After a reaction time of 20 h, followed by a 2-h aging process, the precursor was washed three times with deionized water and dried in an oven at 80 °C for 12 h in an air atmosphere. The target cathodes were obtained by mixing the precursor with LiOH (≥99%, Sigma–Aldrich) in molar ratios of 1:1.1 for LN43 and 1:1 for NM50. This mixture was then heat treated at 500 °C for 5 h and subsequently at 850 °C for 12 h in an air atmosphere. The commercial $LiNi_{0.8}Co_{0.1}Mn_{0.1}O_2$ (NCM811) reference cathodes were purchased from MTI company.

4.2.2 Materials characterization

Ex-situ powder diffraction. X-ray diffraction (XRD) measurements were measured by a Mo source powder diffractometer (STOE STADI P) in transmission geometry, with a wavelength of 0.7093 Å. The samples were loaded into capillaries with an outer diameter of 0.5 mm. The acquisition time for each pattern was 150 min. Synchrotron X-ray diffraction (SXRD) measurements were conducted at beamline P02.1, PETRA III (wavelength of ~0.207 Å) at DESY in Hamburg[112,113]. The samples were loaded into capillaries with an outer diameter of 0.5 mm. Measured intensities were collected using a VAREX CT4343 detector (2880 × 2880 pixels, 150 × 150 μm^2 each) and the acquisition time of 120 s for each pattern. NIST SRM 660c (LaB_6) was used for geometry calibration performed with the software DAWN[114] followed by image integration including geometry, solid-angle, and polarization corrections.

Ex-situ neutron powder diffraction. Neutron powder diffraction (NPD) measurement was carried out on the high-resolution powder diffractometer (D2B) at the Institut Laue-Langevin (ILL) at T = 298 K with wavelength of 1.595 Å. The powder sample (~1 g) was sealed in vanadium cylinders (6 mm diameter) and data collection was conducted for around 4 h to obtain good statistics for data analysis.

In-situ powder diffraction. In-situ SXRD measurements were performed at beamline P02.1, PETRA III (wavelength of ~0.207 Å) at DESY in Hamburg. In-situ measurements were conducted using 2032-type coin cells with glass windows, cycled at C/10 (1C defined as 200 mA g^{-1}) in 2.5-4.55 V and 2.0-4.7 V for one cycle at room temperature using a Biologic VMP3 multichannel battery test system. The acquisition time for each pattern was 60 s. All Rietveld refinements were performed using the Fullprof software package[115].

SEM-EDX. The morphology of the samples was observed by a scanning electron microscope (SEM, Zeiss Merlin) with an acceleration voltage of 10 keV. The coupled energy-dispersive X-ray (EDX) analysis was conducted at a Quantax 400 system from Bruker.

TEM. High-angle annular dark-field scanning transmission electron microscopy (HAADF–STEM) images and energy-dispersive X-ray (EDX) spectra were acquired using an aberration-corrected JEM-ARM300F operated at 300 kV. The atomic structures were plotted using VESTA software[117].

ICP–OES. The compositions of the samples were quantitatively determined by inductively coupled plasma-optical emission spectroscopy (ICP–OES) using a Thermo Fischer Scientific iCAP 7600 DUO.

4.2.3 Spectroscopy characterization

XAS. Hard X-ray absorption spectroscopy (XAS) experiments were performed at the XAS beamline of the KIT synchrotron in in Karlsruhe. In-situ XAS experiments were conducted at synchrotron beamline P64 at PETRA III (DESY), Hamburg. In-situ measurements were conducted using 2032-type coin cells with Kapton windows, cycled at C/10 (1C defined as 200 mA g^{-1}) for half cycle at room temperature using a Biologic VMP3 multichannel battery test system. The acquisition time for each edge was 90 s. All measurements were conducted at room temperature, employing the transmission mode for data acquisition. The obtained XAS data were processed using ATHENA software[118].

SXAS. Soft X-ray absorption spectroscopy (SXAS), experiments were carried out at the WERA beamline at the KARA synchrotron in Karlsruhe. The Ni L-edge and O K-edge spectra were recorded using the fluorescence yield (FY) detection mode and the inverse partial fluorescence yield (iFY) for the Mn L-edge spectra.

RIXS. Resonant inelastic X-ray scattering (RIXS) experiments were conducted at beamline U41-PEAXIS at BESSY II, located at Helmholtz-Zentrum Berlin (HZB)[119]. A vacuum suitcase was used to transfer the sample from an N_2-filled glovebox to the test chamber. The spectrometer was positioned at specular conditions relative to 60° scattering angle and was optimized to a combined resolution of 90 meV using a carbon tape. The O K-edge RIXS spectra of the samples were collected at an excitation energy of 531.0 eV. The acquisition time for each pattern was 30 min. RIXS mapping was measured in 0.5 eV energy steps from 527 eV to 535 eV and the acquisition time for each pattern was 12 min. Data were processed using the beamline software, Adler-4.0.

NMR. Magic-angle spinning (MAS) nuclear magnetic resonance (NMR) spectroscopy was performed on a Bruker Avance neo 200 MHz spectrometer with a magnetic field strength of 4.7 T. MAS spinning was carried out using 1.3 mm rotors at a frequency of 55 kHz. For the ^{6}Li NMR experiments, $^6LiOH\cdot H_2O$ (95 atom%, Sigma–Aldrich) was utilized as the Li source for synthesis. The Larmor frequencies for ^{6}Li and ^{7}Li NMR were 29.5 MHz and 77.8 MHz, respectively. Spectra were acquired employing a rotor-synchronized Hahn-echo pulse sequence, with a 90° pulse length of 0.85 μs for ^{7}Li and 1.6 μs for ^{6}Li. All spectral shifts were referenced to an aqueous solution of LiCl (^{6}LiCl for ^{6}Li) at 0 ppm. The spectral intensities were normalized based on the sample mass and the number of scans. The NMR spectra were fitted using DMFIT program[120].

DEMS. Operando differential electrochemical mass spectroscopy (DEMS) analysis was carried out to study the different gases generated during cell cycling. The set up consisted of a quadrupole mass spectrometer (Thermo Fischer) equipped with turbomolecular pump (Pfeiffer Vacuum) and mass-flow controllers (Bronkhorst). Two electrode type cells (ECC-Std from EL-CELL) with gas inlet and outlet ports were used for the operando measurements. The cell consisted of Li anode, electrolyte (1M $LiPF_6$ in PC) and the same cathode as described above. The cell was cycled with the current density of 20 mA g^{-1} and voltage window of 2.0-4.7 V. Ultrapure Ar was used as carrier gas. The purge gas flow was 1 mL min^{-1}. Detection limits are below 1 ppm.

4.2.4 Theoretical calculations

DFT calculations. All DFT calculations for periodic material systems were performed with the Vienna Ab initio simulation package (VASP)[183] using the projector-augmented wave (PAW) method[184]. The exchange–correlation function was handled using the generalized gradient approximation (GGA) formulated by the Perdew-Burke-Ernzerhof (PBE)[185]. The van der Waals (vdW) interactions are described with the DFT-D3 method in Grimme's scheme[186]. The interaction between the atomic core and electrons was described by the projector augmented wave method. The plane-wave basis set energy cutoff was set to 500 eV[187]. The Brillouin zone was sampled with a 5 × 5 × 5 grid centered at the gamma (Γ) point for geometry relaxation. All structures were fully relaxed to optimize without any restriction until their total energies were converged to < 1×10^{-6} eV[188], and the average residual forces were < 0.02 eV/Å. The oxygen vacancy formation energy, ΔE_0, was evaluated using bellow equation[189,190]:

$$\Delta E_O = E_{VO} + \frac{1}{2}E_{O_2} - E_O$$

where E_{V0} and E_0 represent the total energies of the oxygen-deficient and pristine structures. E_{O_2} is the elemental chemical potential of oxygen.

4.2.5 Electrochemical characterization

Electrode preparation. All electrodes were prepared by mixing the active material, Super C65 conductive carbon black, and polyvinylidene fluoride (PVDF) in a mass ratio of 8:1:1, using N-methyl-2-pyrrolidone (NMP) as the solvent. The resulting mixture was processed in a planetary mixer (THINKY ARV-310) at 2000 rpm for 10 min under an air atmosphere. The slurry was then applied to aluminium foil (15 µm thickness) at a speed of 25.0 mm s^{-1} using a ZUA 2000 Universal applicator, achieving a coating thickness of 150 nm. The coated aluminium foil was subsequently dried in an oven at 80 °C under ambient conditions to evaporate the NMP solvent. After a drying period of 6 h, the electrode material was punched into discs with a diameter of 12 mm, resulting in an active material loading of approximately 3 mg cm^{-2}. A further drying step was conducted using a Büchi glass oven (B-585) under vacuum conditions at 120 °C for 12 h.

Galvanostatic measurements. The electrochemical performance of the electrodes was evaluated using 2032-type coin cells, which were assembled with a Li metal anode (14 mm diameter, 0.25 mm thickness), a single-layer Celgard 2500 membrane (25 μm thickness) as the separator, and 80 μL of electrolyte composed of 1 M lithium hexafluorophosphate ($LiPF_6$) dissolved in a solvent mixture of ethylene carbonate (EC), ethyl methyl carbonate (EMC), and dimethyl carbonate (DMC) in a 1:1:1 volume ratio (DODO Co., Ltd.). All assembly procedures were performed in an argon-filled glovebox, maintaining O_2 and H_2O levels below 0.1 ppm. The cells were cycled at a constant temperature of 25 °C using a Biologic VMP3 multichannel battery test system. The voltage range was 2.5-4.55 V for LN43 and NM50, and 2.7-4.3 V for commercial NCM811 cathode. The charging process included a constant voltage step for 10 min at the upper voltage limit, followed by a 2-min resting period after each charge–discharge cycle.

GITT. The galvanostatic intermittent titration technique (GITT) measurements were performed by periodically pulsing and relaxing the battery between 2.5 and 4.55 V using a Biologic VMP3 multichannel battery test system with a 30 min pulse at 20 mA g^{-1} followed by 4 h relaxation for every step. The Li^+ diffusion coefficient (D_{Li+}) was calculated using equation:

$$D = \frac{4}{\pi\tau}\left(\frac{n_m V_m}{S}\right)^2 \left(\frac{\Delta E_s}{\Delta E_t}\right)^2$$

Where τ is the duration of the current pulse; n_m is the amount of substance; V_m is the molar volume of the electrode; S is the electrode active area; ΔE_s is the change in steady state voltage due to the current pulse and ΔE_t is the voltage change during the constant current pulse.

4.3 Results and Discussion

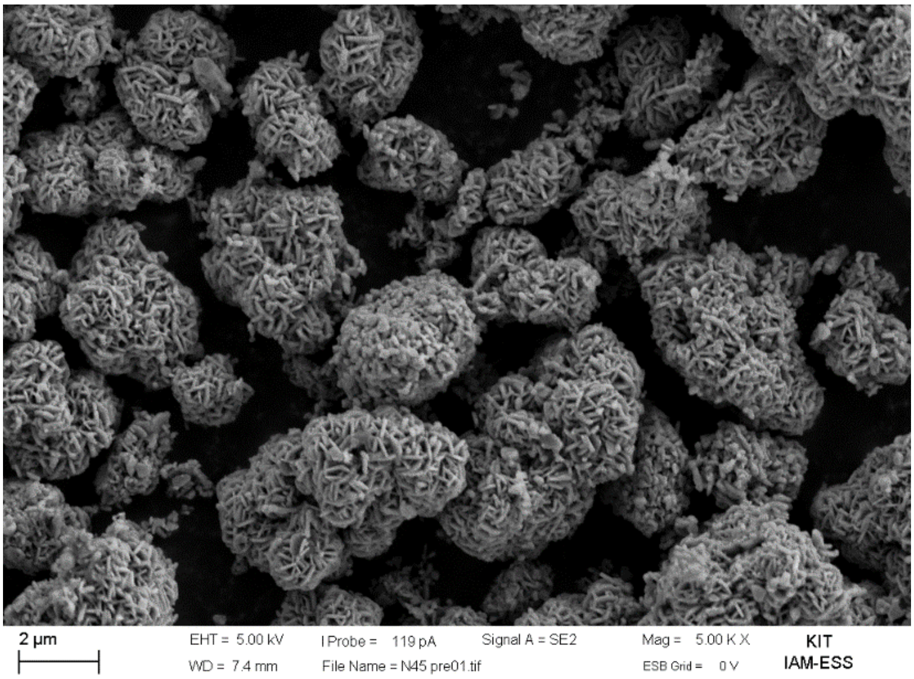

Figure 4.1 SEM images of LN43 powder.

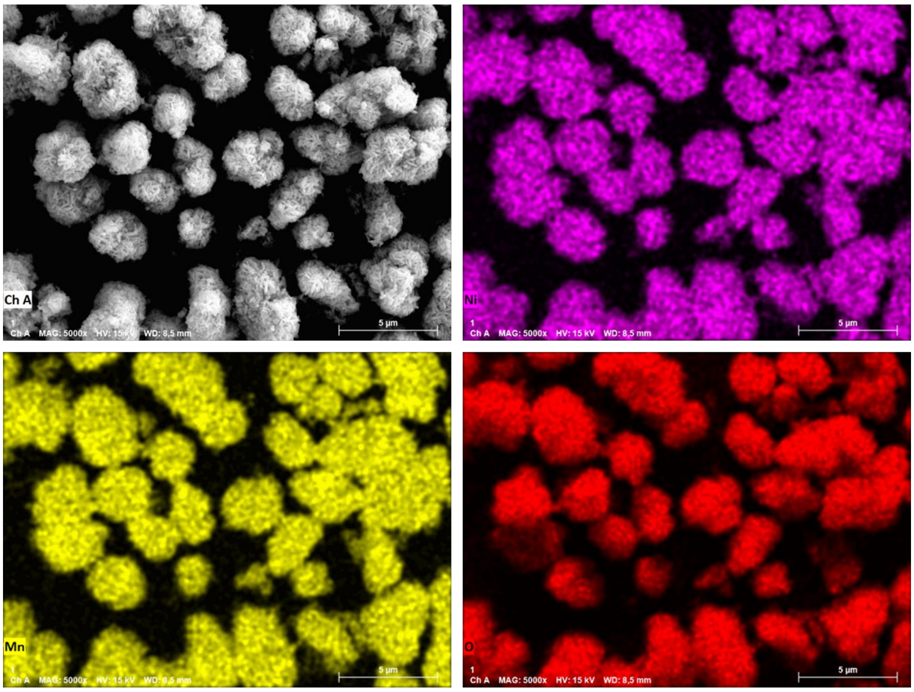

Figure 4.2 SEM mapping images of LN43 powder.

The $Li_{1.05}Ni_{0.43}Mn_{0.52}O_2$ (LN43) cathode was synthesized via solid-state reaction using a hydroxide $Ni_{0.45}Mn_{0.55}(OH)_2$ precursor and LiOH, with a Li/TM (where TM denotes transition metals) molar ratio of 1.1, under ambient air conditions. This composition was chosen for several reasons. First, a slightly Mn-rich content promotes the formation of honeycomb superstructure domains, triggering oxygen redox at high voltages and resulting in higher capacity. Second, the selected Li content ensures that Ni and Mn maintain valence states of +2 and +4, respectively. This maximizes the high-voltage redox activity of Ni while preventing the low-voltage redox activity of Mn, contributing to a higher energy density[106]. Scanning electron microscopy (SEM) images (**Figure 4.1**) reveal that the LN43 powder consists of polycrystalline spherical secondary particles approximately 5-6 μm in diameter. SEM mapping images (**Figure 4.2**) indicate uniform distribution of Ni, Mn, and O. Inductively coupled plasma-optical emission spectroscopy (ICP–OES) results (**Table A8**) confirm that the Li/TM molar ratio is 1.1, which is consistent with the design values.

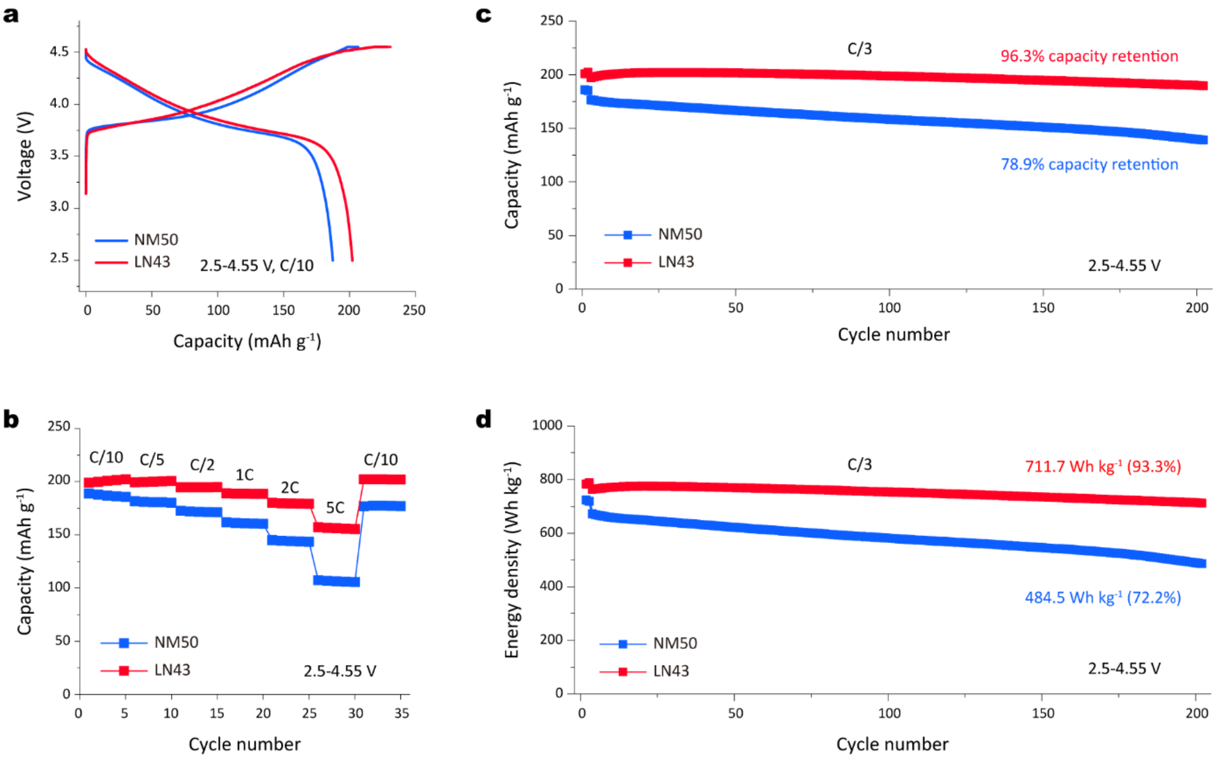

Figure 4.3 (a) Charge and discharge curves for NM50 and LN43 in the first cycle at C/10 within the voltage range of 2.5-4.55 V at 25 °C, where 1C corresponds to 200 mA g^{-1}. (b) The rate capability test conducted from C/10 to 5C. (c) Discharge capacity retention and (d) energy density retention over 200 cycles at C/3 within the voltage range of 2.5-4.55 V.

We first evaluated the electrochemical performance of LN43 and compared it with the low-Ni cathode $LiNi_{0.5}Mn_{0.5}O_2$ (NM50), as described in the Experimental section. **Figure 4.3a** shows the initial charge/discharge curves of both cathodes within the voltage range 2.5-4.55 V. LN43 delivers a discharge capacity of 202.2 mAh g^{-1} and an energy density of 782.8 Wh kg^{-1} at C/10, significantly outperforming NM50, which provides 187.4 mAh g^{-1} and 722.8 Wh kg^{-1} (**Figure**

4.3a and **Figure A7**). The differential capacity (dQ/dV) curves in **Figure A8** reveal a notable difference at approximately 4.5 V, typically attributed to oxygen redox activity, which will be discussed later. LN43 also demonstrates superior rate capability (**Figure 4.3b**), delivering a capacity of 157.1 mAh g^{-1} at 5C, while NM50 maintains only 107.4 mAh g^{-1} under the same conditions. Galvanostatic intermittent titration technique (GITT) measurements (**Figure A9**) indicate that LN43 exhibits significantly superior lithium-ion diffusion capabilities compared to NM50 during charging and discharging. **Figure 4.3c** illustrates the long-term cycling performance at a charge/discharge rate of C/3. LN43 achieves excellent stability, retaining 96.3% capacity retention after 200 cycles, far exceeding that of NM50 (78.9%). Additionally, LN43 retains a higher energy density of 711.7 Wh kg^{-1} with 93.3% retention, compared to 484.5 Wh kg^{-1} and 72.2% retention for NM50 (**Figure 4.3d**). Repeated measurements confirm the reproducibility of these results (**Figure A10**), ensuring the consistency and reliability of the findings.

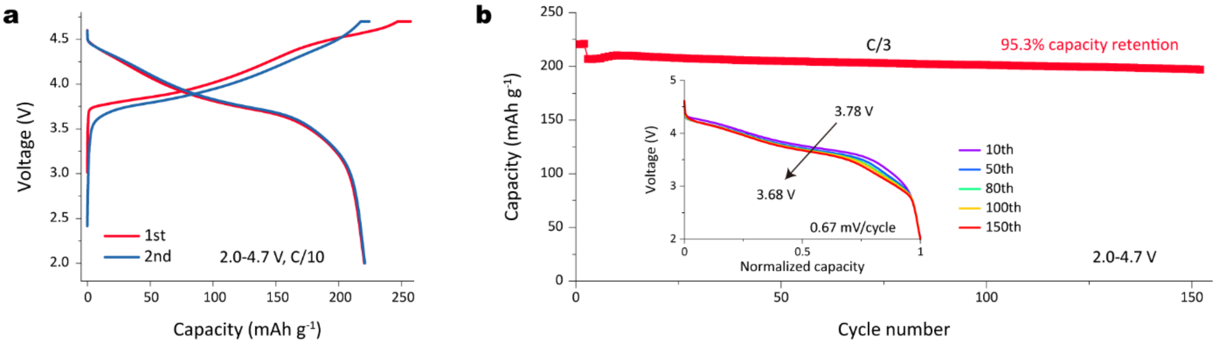

Figure 4.4 (a) Charge and discharge curves of LN43 in the voltage range of 2.0-4.7 V at C/10 at 25°C. (b) Discharge capacity retention of LN43 over 150 cycles at C/3 within the voltage range of 2.0-4.7 V. The inset presents the normalized capacity discharge curves.

We further evaluated the LN43 cathode over a wide voltage range (2.0-4.7 V). **Figure 4.4a** shows that LN43 delivers an impressive capacity of 220.5 mAh g^{-1} with an initial Coulombic efficiency of 85.7%. Furthermore, LN43 demonstrates exceptional rate capability, achieving 161.8 mAh g^{-1} at 5C (**Figure A11**). After 150 cycles at C/3, LN43 maintains a stable cycle life, retaining 95.3% of its capacity (**Figure 4.4b**). The normalized capacity curves (inset of **Figure 4.4b**) illustrate voltage stability, maintaining 3.68 V with minimal voltage decay of 0.67 mV per cycle.

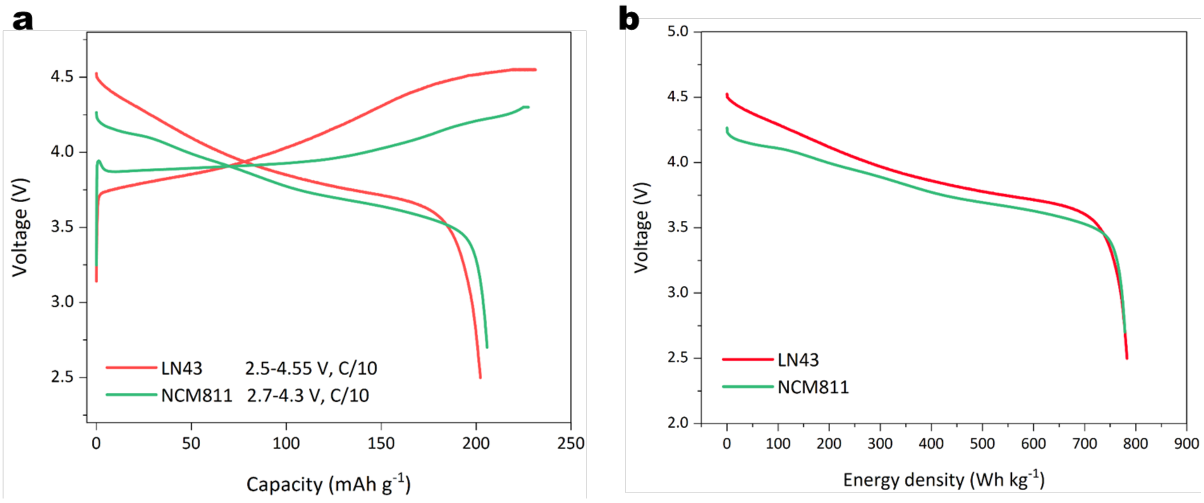

Figure 4.5 (a) Charge and discharge curves for LN43 and NCM811 in the first cycle at C/10 at 25 °C. The voltage range is 2.5-4.55 V for LN43 and 2.7-4.3 V for NCM811 cathode. (b) Energy density curves for both cathodes.

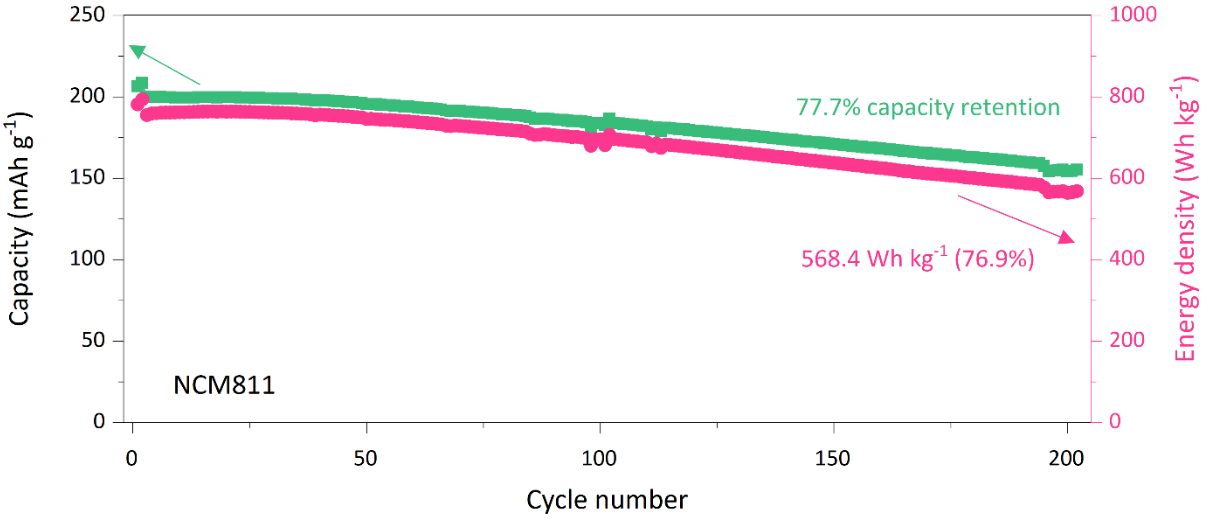

Figure 4.6 Discharge capacity retention (left axis) and energy density retention (right axis) over 200 cycles at C/3 within the voltage range of 2.7-4.3 V for NCM811.

For further comparison, we selected the commercial high-Ni cathode $LiNi_{0.8}Co_{0.1}Mn_{0.1}O_2$ (NCM811). Detailed information about NCM811 can be found in the Experimental section and **Figure A12**. Due to its poor thermal and chemo-mechanical stability at high voltages (4.55 V), we applied a cut-off voltage of 4.3 V. As shown in **Figure 4.5a**, NCM811 achieves a capacity of 205.8 mAh g^{-1}, slightly higher than LN43. Additionally, NCM811 delivers an energy density of 778.8 Wh kg^{-1}, comparable to LN43 (782.8 Wh kg^{-1}, **Figure 4.5b**). After 200 cycles at a C/3 rate, NCM811 retains 77.7% capacity retention and 76.9% energy density retention (**Figure 4.6**), which is significantly lower than the retention values of the LN43 cathode. These results demonstrate that LN43 not only matches the capacity of the NCM811 cathode but also exhibits superior cycle life. Overall, these electrochemical performance findings highlight the potential of the LN43 cathode for achieving both high energy density and stable cycle life, demonstrating its superiority over both low-Ni and high-Ni cathodes.

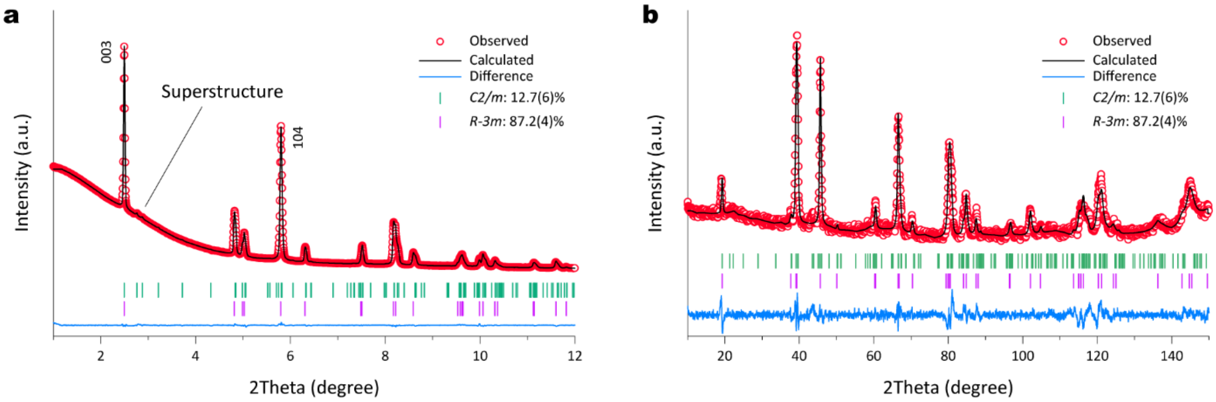

Figure 4.7 Combined Rietveld refinement results of SXRD (a) and NPD (b) for LN43 powder. The refinement was performed with a two-phase model with R-3m and C2/m layered structure. For SXRD and NPD, the wavelengths were 0.2073 and 1.595 Å, respectively.

To elucidate the origin of the exceptional electrochemical performance, we thoroughly investigated the structure of LN43. We first performed synchrotron X-ray powder diffraction (SXRD) and neutron powder diffraction (NPD) to investigate the crystal structure. As shown in **Figure 4.7a-b**, the primary Bragg reflections correspond to the layered rhombohedral (*R-3m*) structure. A smaller portion corresponds to the layered monoclinic (*C2/m*) structure, as indicated by the superstructure Li/Mn ordering[47] in the SXRD pattern at 2θ of 2.7-3.1°. To obtain detailed crystal structure information, a combined refinement of SXRD and NPD was conducted. The refinement results (**Table A9**) reveal phase fractions of 87.2(4) wt.% for *R-3m* and 12.7(6) wt.% for *C2/m*. Additionally, the LN43 cathode shows a Li/Ni mixing ratio of 11.1% in the *R-3m* phase, comparable to that of the low-Ni NM50 cathode[175]. Most importantly, in the *C2/m* phase, some nickel ions occupy the octahedral 2c and 4h sites within the Li layer, with a total fraction of 6.1(5) wt.%.

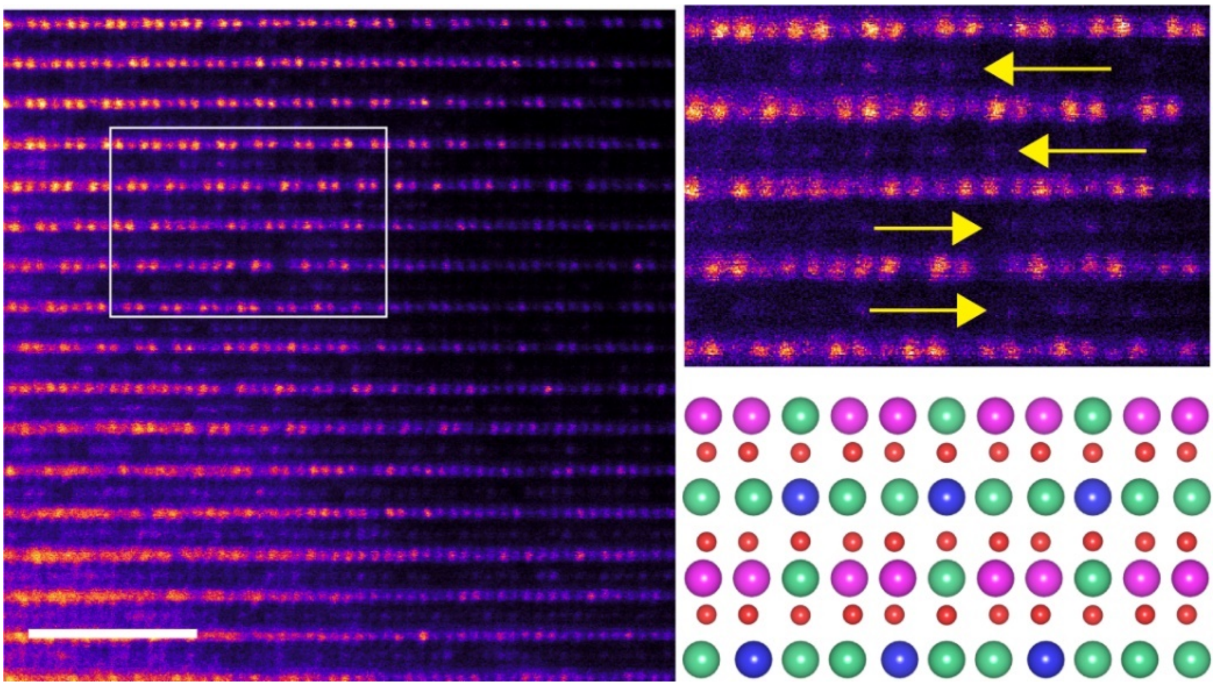

Figure 4.8 HAADF–STEM image along the [110] zone axis of LN43 powder. Schematic diagram illustrating atomic arrangement. Ni, Mn, Li and O are shown as blue, purple, green and red spheres, respectively.

To visualize the local atomic arrangement, high-angle annular dark-field scanning transmission electron microscopy (HAADF–STEM) was employed. As shown in **Figure 4.8** and **Figure A13**, the distinctive dumbbell-like superstructure (Li-Mn-Mn-Li) in the *C2/m* phase is clearly visible along the [110] zone axis. Some Li ions in the TM layer are replaced by TM ions, resulting in partial in-plane disorder[97,99]. Notably, bright dots indicated by the yellow arrows in **Figure 4.8** are observed in the Li layer, indicating the presence of heavy TM ions such as Ni or Mn ions. Atomic-scale energy-dispersive X-ray (EDX) mappings and line profile analysis (**Figure A14**) confirm that Mn ions are primarily located in the TM layers, while Ni ions are distributed in both the TM and Li layers. Therefore, these bright dots represent Ni rather than Mn ions. Based on the SXRD/NPD refinement results, we built a structural model illustrating this atomic arrangement (**Figure 4.8**). In this model, some Li ions (green) in the Li layer are replaced by Ni ions (blue), leading to the formation a Ni-pinned honeycomb structure. Previously, Luo et al.[102] designed a capped-honeycomb structure, where TM ions occupy Li layers, in an O2-type Li-rich cathode, achieving enhanced lattice oxygen activity and structural stability. We anticipate that our structural design will yield similar positive effects, which will be discussed latter.

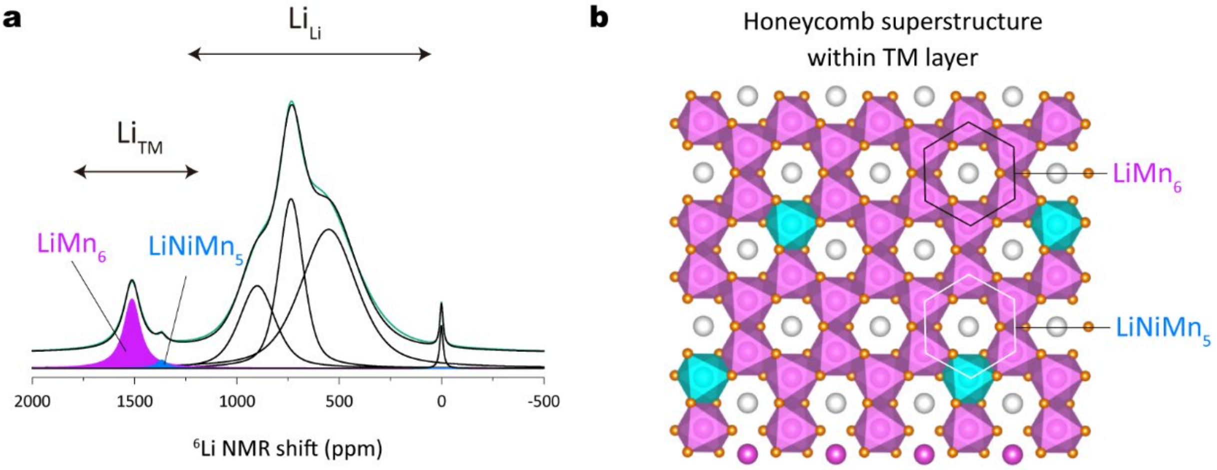

Figure 4.9 (a) ^{6}Li MAS NMR spectra and fitting results for LN43 powder and (b) the corresponding schematic of in-plane ordering of Li (gray) and Mn (purple octahedra) or Ni (blue octahedra) within TM layers forming LiMn$_6$ and LiNiMn$_5$ superstructure units.

We also conducted ^{6}Li solid-state nuclear magnetic resonance (NMR) spectroscopy to investigate the local Li environments. **Figure 4.9a** shows the ^{6}Li NMR patterns along with fitting results. The sharp peak at 0 ppm represents diamagnetic species such as LiOH, Li_2CO_3, and organic lithium salts[152,191]. Additionally, there are two groups of peaks, one at 500-1000 ppm and another at 1300-1500 ppm, indicating different Li environments in the layered structure. Specifically, the peaks at 500-1000 ppm correspond to Li in the Li layer (Li$_{Li}$), while those at 1300-1500 ppm correspond to Li in the TM layer (Li$_{TM}$)[153]. Peaks at approximately 1500 ppm and 1300 ppm correspond to honeycomb superstructure units for LiMn$_6$ (purple) and LiNiMn$_5$ (blue), respectively, consistent with previous literature[155,156] (**Figure 4.9b**). According to the fitting results (**Table A10**), the peak area fraction of Li$_{TM}$ (LiNiMn$_5$ and LiMn$_6$) is 8.61%. This value is slightly higher than the value obtained from the SXRD/NPD diffraction refinements, which indicate 12.7(6) wt.% *C2/m*, corresponding to 5.66% Li$_{TM}$. Given the complexity of these two phases in both local and average crystal structures, these differences are considered reasonable.

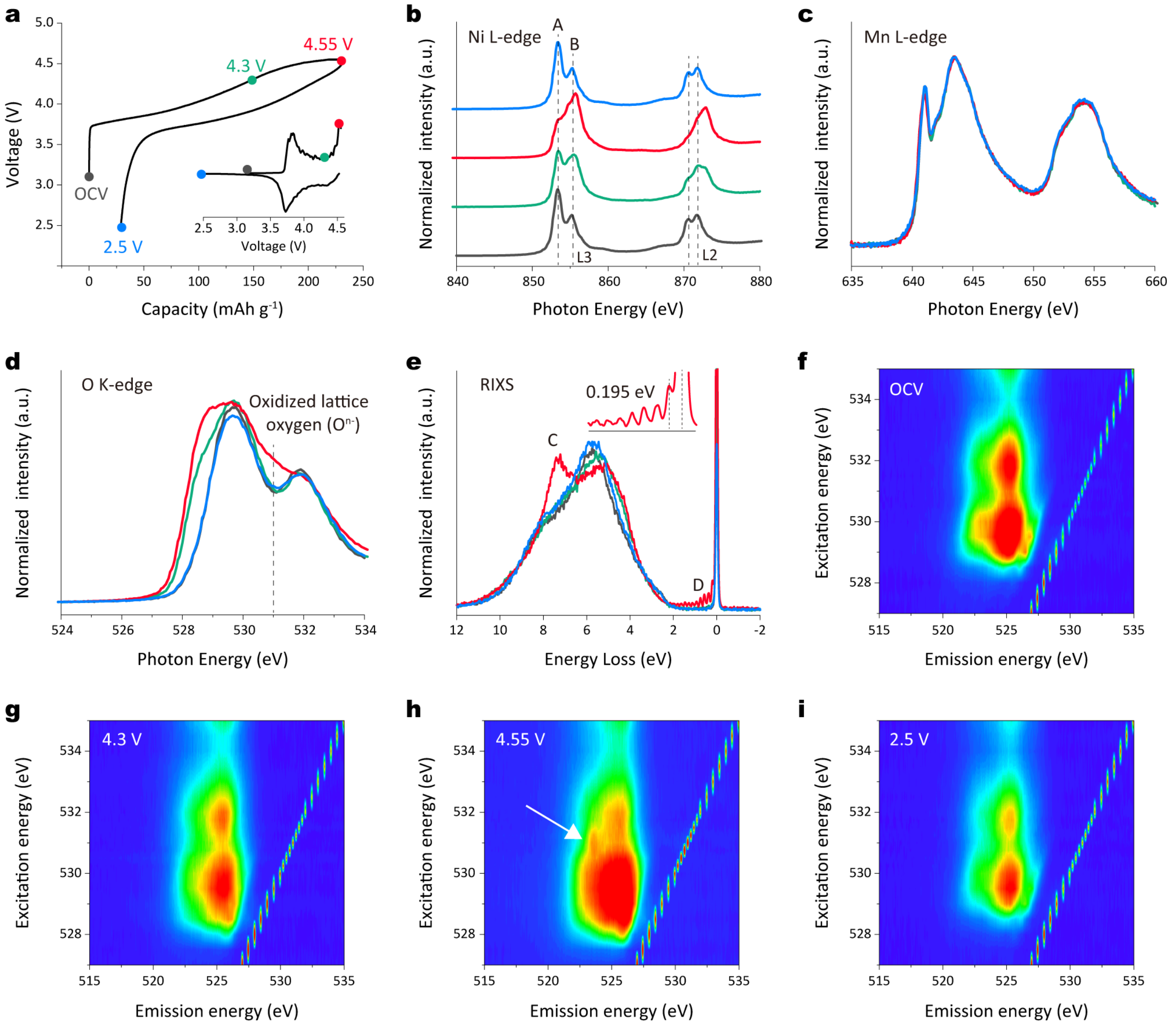

Figure 4.10 (a) Initial charge and discharge curves for LN43 with specific points marked for SXAS and RIXS measurements. Inset: dQ/dV curve with the corresponding crucial points taken for SXAS and RIXS. SXAS results for the (b) Ni L-edge, (c) Mn L-edge, and (d) O K-edge, collected at OCV, after charging to 4.3 V and 4.55 V, and after discharging to 2.5 V. Fluorescence yield (FY) mode was used for Ni and O, while inverse fluorescence yield (iFY) mode was used for Mn. (e) O K-edge RIXS spectra collected at an excitation energy of 531 eV at OCV, 4.3 V charge, 4.55 V charge, and 2.5 V discharge states. The inset provides an enlarged view of the elastic region (0-1 eV) at the 4.55 V charge state. (f-i) O K-edge RIXS mapping obtained with excitation energies ranging from 527 to 535 eV at OCV, 4.3 V charge, 4.55 V charge, and 2.5 V discharge states.

We then examined the redox mechanisms of the LN43 cathode using ex-situ soft X-ray absorption spectroscopy (XAS). Fluorescence yield (FY) mode was used for Ni and O, while inverse fluorescence yield (iFY) mode was used for Mn. As shown in in **Figure 4.10a-d**, several crucial states during the first cycle were selected to collect the Ni, Mn L-edge and O K-edge spectra. The Ni L3-edge spectra (dashed lines in **Figure 4.10b**) reveal significant changes in the intensity of peaks A (~852.9 eV) and B (~854.8 eV) during charging, indicating Ni oxidation[140,143]. While Ni oxidation in Ni-based layered oxides typically occurs at a cut-off voltage of 4.3 V[192], we observed continuous oxidation from 4.3 V to 4.55 V in the LN43 cathode, probably due to a different Ni environment. The Mn L-edge spectra (**Figure 4.10c**) remains unchanged throughout cycling, indicating the stability of Mn in an inactive Mn^{4+} valence state throughout the entire electrochemical process. Additionally, the O K-edge spectra (**Figure 4.10d**) show a gradual intensity increase at approximately 528.5 eV during charging, corresponding to Ni oxidation and Ni-O bond formation (hybridization)[142], which aligns with the Ni L-edge observations. Notably, a new peak emerges at about 531 eV (dashed lines) at the end of charge (4.55 V), which is attributed to oxidized lattice oxygen species (O^{n-})[79,144]. During discharge to 2.5 V, both the Ni L-edge and O K-edge spectra fully revert to their initial state at open-circuit voltage (OCV), confirming the high reversibility of the redox reactions.

To further investigate the nature of oxidized lattice oxygen, we conducted O K-edge resonant inelastic X-ray scattering (RIXS) measurements. As shown in **Figure 4.10e**, the charge state at 4.55 V exhibits a distinct inelastic peak C (around 7.8 eV) and a vibrational peak D near the elastic region (0 eV), both of which are absent in the OCV and 4.3 V charge states. A closer look at the vibrational peak in the inset of **Figure 4.10e** reveals a series of energy-loss peaks corresponding to vibrational frequencies of 1573 cm^{-1}, closely matching the O-O bond length in molecular O_2, consistent with previous studies[47,86,87,145]. Upon discharge, all molecular O_2 features disappear, indicating the reversible reduction of molecular O_2 to O^{2-} species. RIXS mappings in **Figure 4.10f-i** further support these observations. Specifically, **Figure 4.10h** shows distinct molecular O_2 characteristics at a charge of 4.55 V, around an excitation energy of 531 eV and an emission energy of 523.7 eV (highlighted by the white arrow), while these features are barely visible in other states. These results confirm the reversibility and stability of the oxygen redox process in the LN43 cathode.

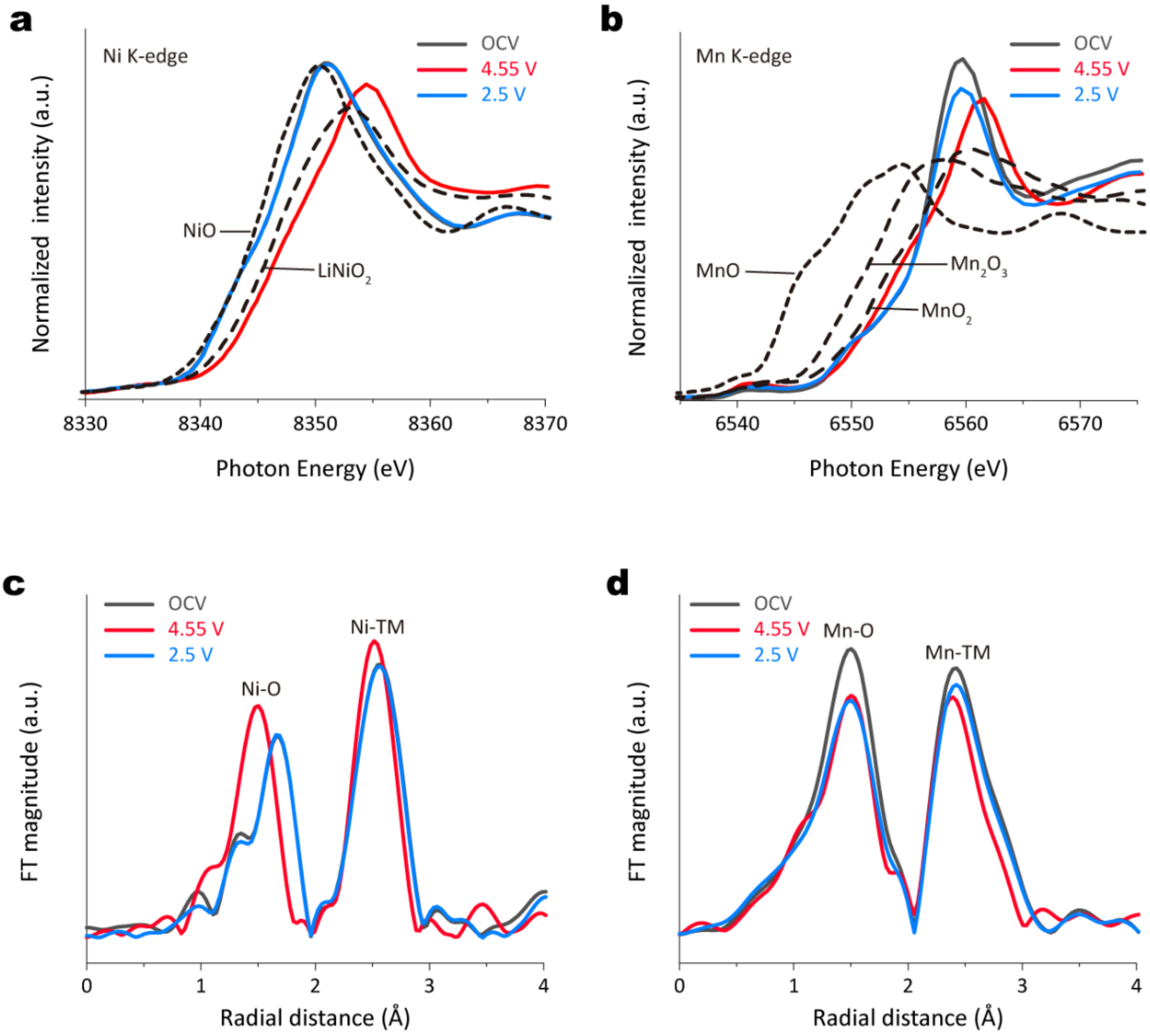

Figure 4.11 Normalized XAS Ni (a) and Mn (b) K-edge XANES of LN43 at OCV, charge to 4.55 V, and discharge to 2.5 V states. FT-EXAFS of Ni (c) and Mn (d) K-edge of LN43 at OCV, charge to 4.55 V, and discharge to 2.5 V states. The XAS data are collected in transmission mode.

To further understand the redox evolution of Ni and Mn, hard XAS measurements were conducted. The Ni K-edge X-ray absorption near-edge structure (XANES) spectra (**Figure 4.11a**) shift to higher energy during charging and return to their original position during discharge, indicating the redox activity of $Ni^{2+/3+/4+}$. In contrast, the Mn K-edge XANES spectra (**Figure 4.11b**) show more complex changes, with no significant edge shifts, suggesting alterations in the local coordination environment around Mn ions[193]. The valence state changes are further supported by Fourier transform extended X-ray absorption fine structure (FT-EXAFS) results (**Figure 4.11c-d**). These findings indicate that the primary redox activity in LN43 is driven by Ni, with a partial contribution from oxygen.

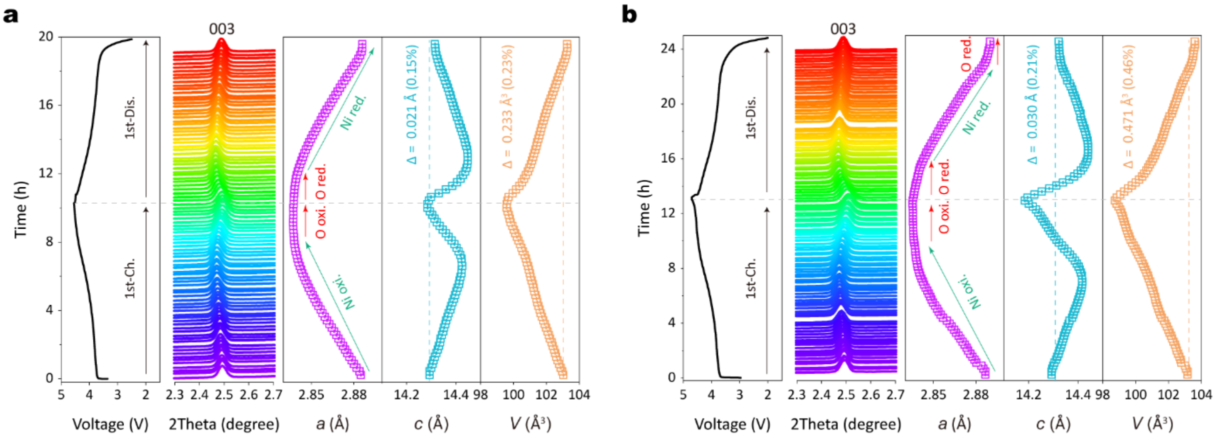

Figure 4.12 (a) In-situ SXRD of LM43 during the first cycles at C/10 in the voltage range of 2.5-4.55 V (a) and 2.0-4.7 V (b) at 25 °C. The corresponding lattice parameters and volume were obtained by Rietveld refinement. The wavelength was 0.2073 Å.

In-situ SXRD measurements were conducted to observe structural evolution of the LN43. **Figure 4.12a** presents the in-situ diffraction patterns and refinement results within the 2.5-4.55 V range. Initially, the 003 Bragg reflection shifts to lower angles during charging, indicating an increase in the lattice parameter *c*, which is due to increased electrostatic repulsion as Li ions are extracted from the Li layer[96]. Simultaneously, the lattice parameter *a* decrease linearly, primarily due to Ni oxidation (green arrows in **Figure 4.12a**), which shortens the TM-O bond length in the TMO_2 slab[107]. At the end of charging, the 003 Bragg reflection shifts in the opposite direction, indicating a shrinkage in the lattice parameter *c*. This change suggests the removal of Li ions from the TM layer[162]. The lattice parameter *a* shows minimal changes in this region, suggesting oxygen oxidation (red arrows in **Figure 4.12a**). During discharging, the lattice parameters *a* and *c* undergo reversible changes, corresponding to the reduction of oxygen and Ni, respectively (as indicated by the arrows). After one complete cycle, the LN43 cathode demonstrates minimal changes in parameter *c* and volume, with variations of only 0.021 Å (0.15%) and 0.233 Å^3 (0.23%), respectively. These results indicate superior structural reversibility and stability. Further structural evolution of the LN43 cathode was examined over a wide voltage range (2.0-4.7 V). As shown in **Figure 4.12b**, the cathode continues to exhibit reversible structural changes. Specifically, the lattice parameter *c* and volume varied by 0.030 Å (0.21%) and 0.471 Å^3 (0.46%), respectively. Additionally, the oxygen oxidation plateau increases with the cut-off voltage as indicated by the red arrows in the lattice parameter *a*. During discharge, beyond the reduction of oxygen and Ni at high potential, additional oxygen reduction[66,84] occurs at low potential, evidenced by minor changes in the lattice parameter *a* (red arrows). This phenomenon is mainly attributed to cationic-anionic redox inversion in Li-rich cathodes[140].

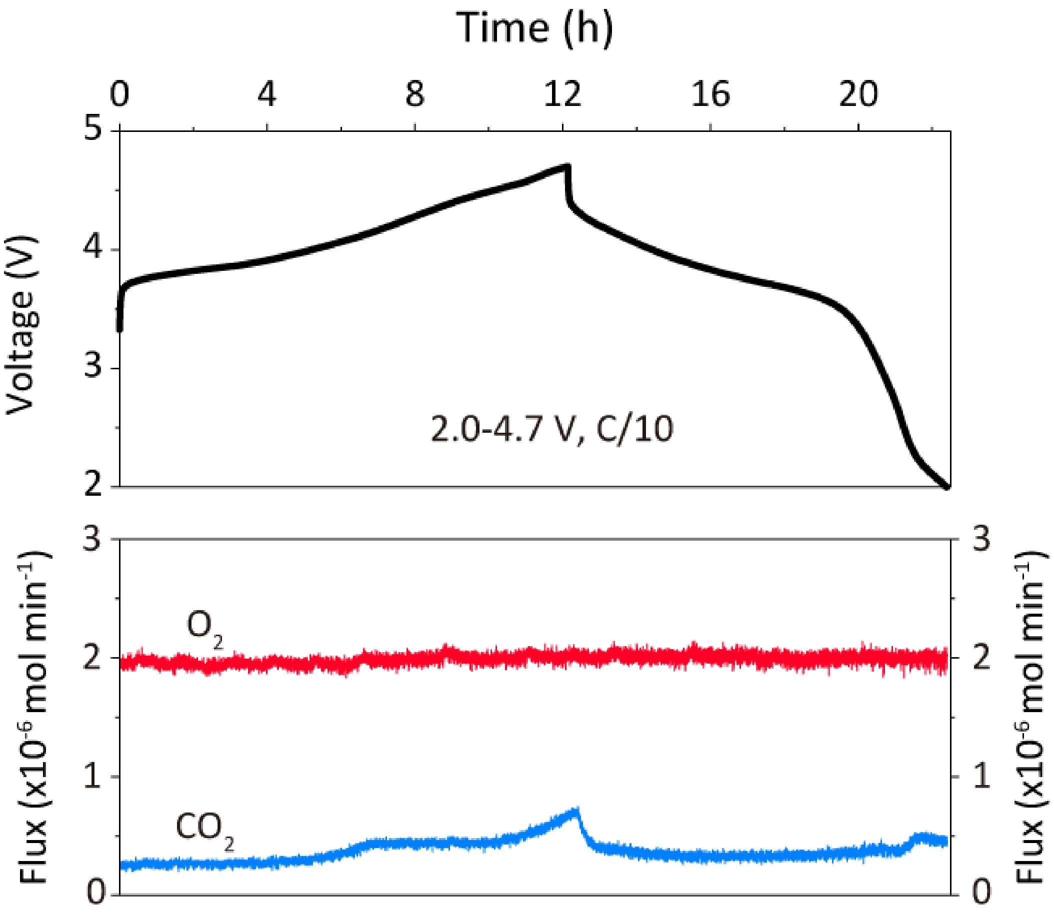

Figure 4.13 Gas evolution of LN43 cathode determined by operando DEMS in the voltage range of 2.0-4.7 V.

To monitor the gas release during battery operation, we performed operando differential electrochemical mass spectroscopy (DEMS) analysis across a wide voltage range of 2.0-4.7 V to thoroughly assess the cathode performance. As shown in **Figure 4.13**, the relatively stable background reflects a consistent argon flux (carrier gas, m/z = 40). Upon charging, only minimal CO_2 gas (*m*/*z* = 44) release is detected (blue line), mainly due to electrolyte decomposition at high voltage[149,194]. Importantly, no oxygen gas (m/z = 32) release is observed throughout the entire electrochemical process, indicating stable oxygen redox activity in the LN43 cathode.

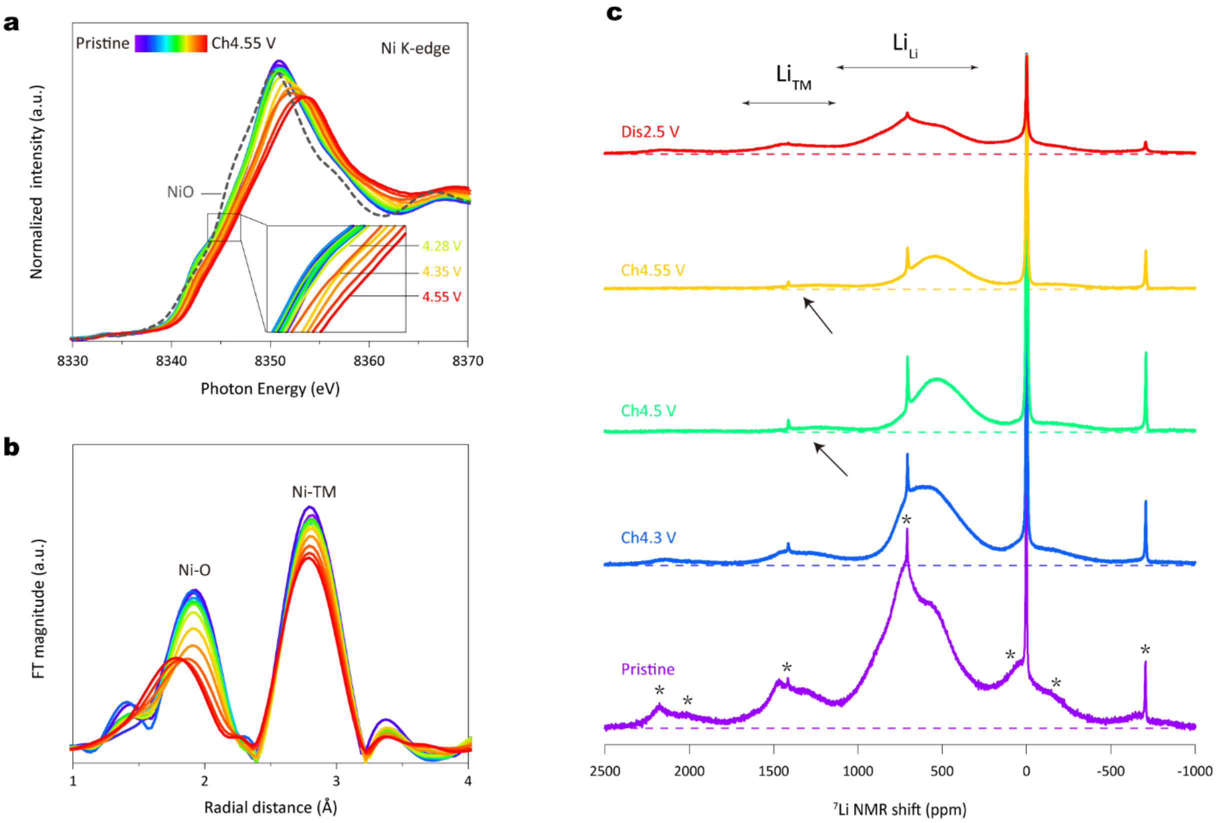

Figure 4.14 (a) In-situ Ni K-edge XANES spectra and (b) corresponding FT-EXAFS spectra during charging process at C/10 in the voltage range of 2.5-4.55 V at 25 °C. The XAS data are collected in transmission mode. (c) ^{7}Li MAS NMR spectra of LM43 electrode in the pristine state and after charging to 4.3, 4.5, and 4.55 V, and discharging to 2.0 V in the first cycle. Spinning sidebands are marked by an asterisk.

To capture the dynamic local structure changes, we conducted in-situ XAS measurements on the LN43 cathode. As shown in **Figure 4.14a**, the Ni K-edge XANES spectra shift to higher energy during charging, indicating the oxidation of Ni, consistent with earlier Ni L-edge SXAS findings. Notably, below 4.28 V, the Ni K-edge shifts gradually (inset of **Figure 4.14a**), but it shifts more rapidly above 4.28 V. These non-continuous changes are further confirmed by FT-EXAFS results (**Figure 4.14b**), showing minimal changes in the Ni-O distance below 4.28 V and significant changes above this voltage. Previous literature[195] suggests that these changes correspond to the gradual accumulation of Ni^{3+} and the rapid oxidation of Ni^{3+} to Ni^{4+}, potentially mitigating structural instability associated with the Jahn-Teller distortion of Ni^{3+}. During charging, the Mn K-edge XANES spectra (**Figure A15a**) remain unchanged, indicating the inactive state of Mn^{4+}, consistent with the Mn L-edge SXAS results. Additionally, the minimal changes in the Mn-O distance observed in the Mn FT-EXAFS spectra (**Figure A15b**) further support these findings.

Ex-situ ^{7}Li NMR spectroscopy were performed to track the evolution of Li local environments. **Figure 4.14c** shows the ^{7}Li NMR results for the pristine state that confirm the presence of honeycomb superstructure units in the LN43 cathode, consistent with the ^{6}Li NMR measurements described above. Upon charging, the NMR peak at 500-1000 ppm continuously shifts to lower ppm values, with a gradual decrease in intensity, indicating continuous Ni oxidation and the removal of Li ions from the Li layer. These findings align with the in-situ SXRD/XAS and ex-situ SXAS results described above. Additionally, the NMR peak in the 1300-1500 ppm range remains unchanged below 4.3 V but significantly decreases above this voltage (as indicated by arrows), suggesting the removal of Li ions from the TM layer at high voltage. During discharge, the intensity and shift of the NMR peak exhibit reversible changes, highlighting the excellent local structural stability of the LN43 cathode.

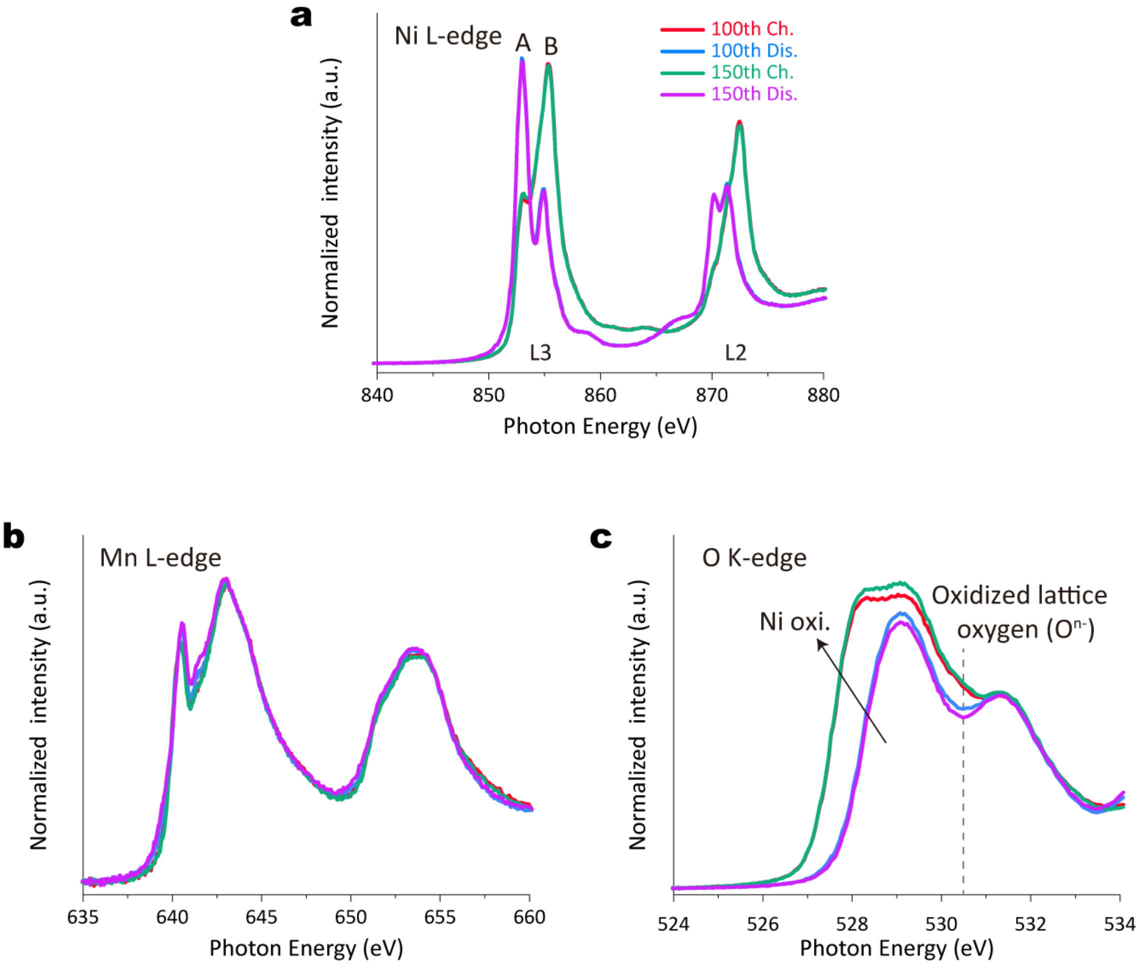

Figure 4.15 SXAS results of the Ni L-edge (a), Mn L-edge (b), and O K-edge (c) collected at charge to 4.55 V and discharge to 2.5 V states after 100 and 150 cycles. The FY mode was applied for Ni and O and the iFY mode was applied for Mn.

To assess redox reversibility and stability during extended cycling, we conducted ex-situ SXAS measurements after 100 and 150 cycles at C/3 in both fully charged (4.55 V) and discharged

(2.5 V) states. As shown in **Figure 4.15a**, the Ni L3-edge spectra reveal opposite changes in peak A (~852.9 eV) and B (~854.8 eV) during charging and discharging. Across different cycles and at the same states, the Ni L-edge spectra maintain nearly identical shape and energy shifts, indicating stable Ni redox activity throughout cycling. Since cathodes with oxygen redox often trigger Mn redox to offset reduced oxygen activity during cycling[93,106], it is essential to evaluate the stability of both Mn and oxygen redox processes. The Mn L-edge spectra (**Figure 4.15b**) show minimal changes in shape and shift, confirming that Mn remains inactive, retaining a Mn^{4+} valence state throughout the cycling process. In the charged state, both electrodes exhibit an intensity increase around 528 eV in the O K-edge spectra (as indicated by the arrow in **Figure 4.15c**), reflecting Ni oxidation, consistent with the Ni L-edge results. Notably, all charged electrodes display characteristic lattice oxidized oxygen features around 531 eV (indicated by dashed lines), underscoring the exceptional reversibility and stability of oxygen redox in LN43 during extended cycling.

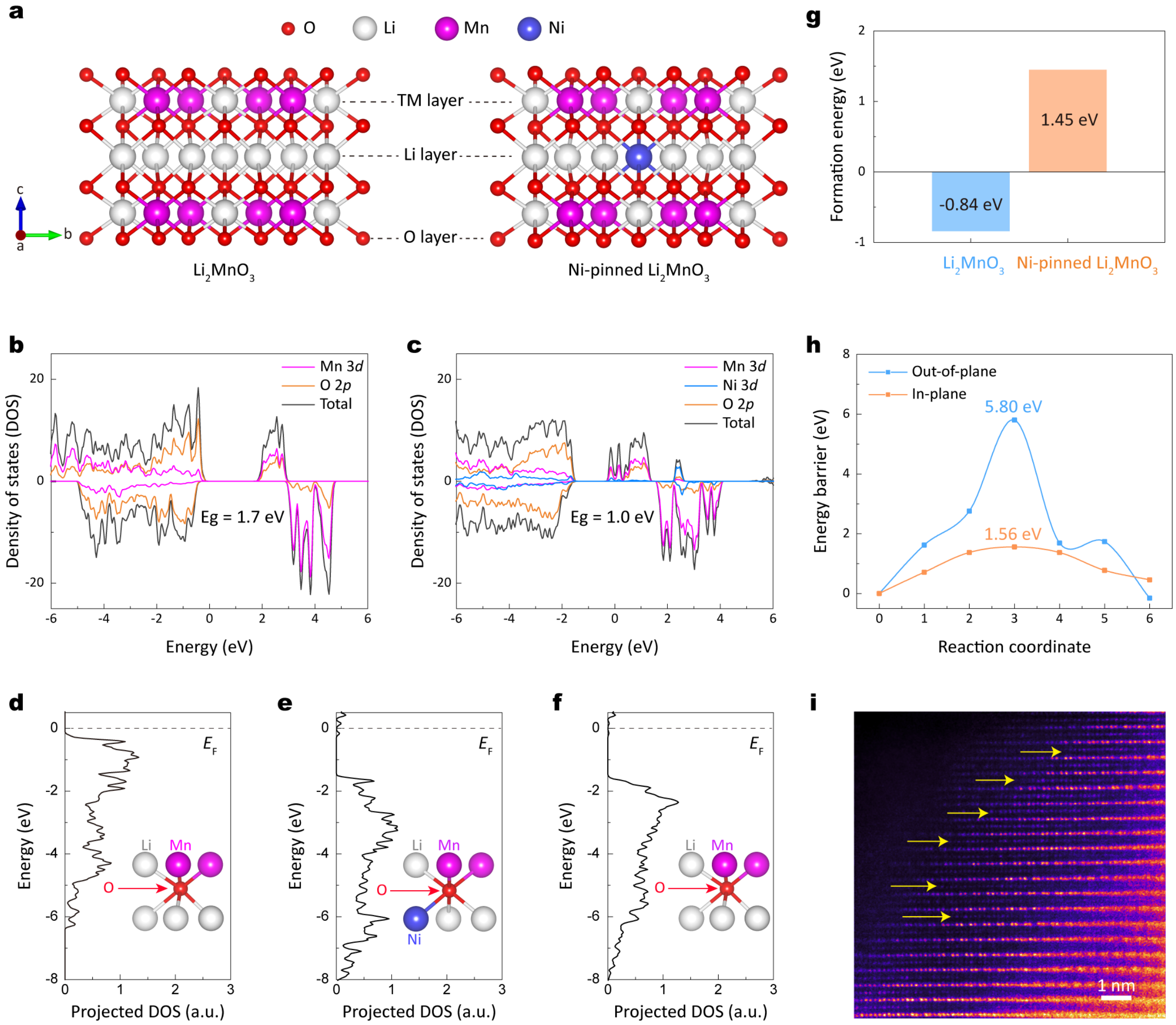

Figure 4.16 (a) Atomic structure models of Li_2MnO_3 (left) and Ni-pinned Li_2MnO_3 (right). The total density of states (DOS) and partial density of states (pDOS) for (b) Li_2MnO_3 and (c) Ni-pinned Li_2MnO_3. (d-f) Projected density of states (DOS) with schematic illustrations of the local environment: (d) lattice oxygen in Li_2MnO_3 coordinated by four Li and two Mn atoms, (e) lattice oxygen in Ni-pinned Li_2MnO_3 coordinated by three Li, one Ni and two Mn atoms, (f) lattice oxygen in Ni-pinned Li_2MnO_3 coordinated by four Li and two Mn atoms. (g) Oxygen vacancy formation energy for Li_2MnO_3 and Ni-pinned Li_2MnO_3. (h) Migration barrier for Ni ions within the plane and out-of-plane in Ni-pinned Li_2MnO_3. (i) HAADF–STEM image of the LN43 electrode, captured along the [110] zone axis after 100 cycles at a C/3 rate.

To explore how the Ni-pinned honeycomb structure improves structural and oxygen redox stability, we performed density functional theory (DFT) calculations. We used O3-type $Li_8Mn_4O_{12}$ (Li_2MnO_3) and $Li_7NiMn_4O_{12}$ (Ni-pinned Li_2MnO_3, with one Ni ion replacing a Li ion in the Li layer) as structural models (**Figure 4.16a**). The density of states (DOS) for both structures, depicted in **Figure 4.16b-c**, reveal that Ni-pinned Li_2MnO_3 has a reduced bandgap of 1.0 eV, compared to 1.7 eV for Li_2MnO_3. This reduction suggests improved electronic conductivity, which benefits rate capability[196]. As shown in the insets of **Figure 4.16d-f**, lattice oxygen in Li_2MnO_3 is coordinated by four Li and two Mn atoms. In contrast, in Ni-pinned Li_2MnO_3, lattice oxygen is coordinated either by three Li, one Ni, and two Mn atoms, or by four Li and two Mn atoms. The oxygen partial density of states (pDOS) in Ni-pinned Li_2MnO_3 is more uniformly distributed and further from the Fermi level compared to Li_2MnO_3, where it is concentrated closer to the Fermi level. This shift indicates a higher oxygen redox potential in Ni-pinned Li_2MnO_3, contributing to enhanced lattice oxygen and voltage stability[197]. Additionally, we calculated the oxygen vacancy formation energy in a highly de-lithiated state (**Figure 4.16g**). The formation energy in the Ni-pinned Li_2MnO_3 structure is 1.45 eV, significantly higher than that the -0.84 eV in Li_2MnO_3, confirming that the Ni-pinned honeycomb structure significantly improves lattice oxygen stability.

We also examined the thermodynamic stability of the Ni-pinned honeycomb structure under high voltage, particularly focusing on the migration behaviour of Ni ions in a highly de-lithiated state (where no Li ions remain in the Li layer, **Figure 4.16h**). For in-plane migration, where a Ni ion moves between octahedral sites via an intermediate tetrahedral site, the energy barrier is 1.56 eV. In contrast, out-of-plane migration, where Ni ion moves to the TM layer, has a significantly higher energy barrier of 5.80 eV. This indicates that at high voltage, the Ni ions in the Li layer are more likely to migrate within the plane, preserving the Ni-pinned honeycomb structure during cycling. To validate this, we performed HAADF–STEM measurements on electrodes after 100 cycles in the discharged state. As shown in **Figure 4.16i**, the distinctive dumbbell-like superstructure along the [110] zone axis remains visible, with bright spots in the Li layer (highlighted by yellow arrows) confirming the persistence of the Ni-pinned honeycomb structure. This stable local structure supports reversible and consistent oxygen redox activity, ensuring a long cycle life.

4.4 Conclusion

We have successfully developed a high-performance, cost-effective lithium-ion layered oxide cathode, $Li_{1.05}Ni_{0.43}Mn_{0.52}O_2$. Through the optimization of its chemical composition, 12.7(6) wt.% Ni-pinned honeycomb Li_2MnO_3-like domains are integrated into the material. The unique Ni-pinned honeycomb structures enable stable oxygen redox activity at high voltages without releasing oxygen gas, leading to a substantial improvement in capacity. Meanwhile, the high thermodynamic stability of the Ni-pinned honeycomb structure ensures structural integrity and supports a stable cycle life. As a result, this cathode achieves an impressive discharge capacity of 202.2 mAh g^{-1} at C/10 and demonstrates excellent cycling stability, retaining 96.3% capacity and 93.3% energy after 200 cycles at C/3, within a voltage range of 2.5-4.55 V. This electrochemical performance not only significantly surpasses that of the conventional low-Ni NM50 but also compares favourably to the commercial high-Ni NCM811 cathode. Additionally, the popular Li-rich cathodes are plagued by unstable oxygen redox activity, thus this work may also serve as a guide for future material design. Overall, this work offers a straightforward approach to designing high-energy-density, cost-effective cathodes for LIBs.

Chapter 5 Summary and Recommendations for future work

To develop high-energy-density cathode materials for LIBs, oxygen redox chemistry has attracted significant attention for its ability to provide additional capacity beyond traditional TM redox activity. However, to effectively harness the potential of oxygen redox processes, it is crucial to gain a comprehensive understanding of the relationship between local structure and oxygen redox activity. The objective of the present study is to elucidate this relationship while also exploring practical synthesis strategies for designing high-performance lithium-ion layered cathodes with stable oxygen redox capabilities. In the first part of this thesis (Chapter 3), we identify the types of honeycomb superstructure units and, for the first time, reveal the valence state of Ni associated with these superstructure units in layered Li-rich cathodes. Furthermore, we establish a strong correlation between these units and electrochemical behaviour, particularly regarding oxygen redox activity. These new insights enhance our understanding of how to achieve reversible oxygen redox activity in high-nickel Li-rich cathodes. Additionally, based on the mechanisms identified, we conduct experiments to further validate our findings. In the second part of this thesis (Chapter 4), building on the findings from the previous research, we design a lithium-ion cathode that achieves stable and reversible oxygen redox activity through chemical composition optimization. In this cathode, we meticulously eliminate the Ni-containing superstructure unit and successfully incorporate a unique local honeycomb superstructure. Benefitting from the stable TM and oxygen redox contributions, this cathode demonstrates enhanced capacity and improved cycle stability.

Leveraging oxygen redox chemistry to enhance the energy density of LIBs has been a long-standing objective that necessitates ongoing theoretical and experimental research to be further expanded and intensified. This study offers valuable insights into the effects of honeycomb superstructure unit types and local honeycomb design on oxygen redox activity in lithium-ion cathodes. Based on these findings, several recommendations for future research emerge. To design high-capacity high-nickel Li-rich cathodes, in addition to reducing lithium content during synthesis, various other modification strategies could provide potential solutions. These strategies include cation doping with high-valence ions (such as Ta^{5+}, Nb^{5+}, Mo^{6+}, and W^{6+}), anion doping with low-valence ions (like F^-), or the formation of oxygen vacancies to lower the nickel valence state. Therefore, future research efforts should consider exploring these approaches to achieve optimization and to facilitate the development of high-energy-density Li-rich layered oxides.

References

1. Fuso Nerini, F. *et al.* Mapping synergies and trade-offs between energy and the Sustainable Development Goals. *Nat. Energy* **3**, 10–15 (2017).
2. Frölicher, T. L., Fischer, E. M. & Gruber, N. Marine heatwaves under global warming. *Nature* **560**, 360–364 (2018).
3. Yu, Y.-S., Zhang, X., Liu, J.-W., Lee, Y. & Li, X.-S. Natural gas hydrate resources and hydrate technologies: a review and analysis of the associated energy and global warming challenges. *Energy Environ. Sci.* **14**, 5611–5668 (2021).
4. Dunn, B., Kamath, H. & Tarascon, J.-M. Electrical Energy Storage for the Grid: A Battery of Choices. *Science* **334**, 928–935 (2011).
5. Manthiram, A. A reflection on lithium-ion battery cathode chemistry. *Nat. Commun.* **11**, 1550 (2020).
6. Guyomard, D. & Tarascon, J.-M. Rocking-Chair or Lithium-Ion Rechargeable Lithium Batteries. *Adv. Mater.* **6**, 408–412 (1994).
7. Scrosati, B. Lithium Rocking Chair Batteries: An Old Concept? *J. Electrochem. Soc.* **139**, 2776–2781 (1992).
8. Dunn, B., Kamath, H. & Tarascon, J.-M. Electrical Energy Storage for the Grid: A Battery of Choices. *Science* **334**, 928–935 (2011).
9. Harper, G. *et al.* Recycling lithium-ion batteries from electric vehicles. *Nature* **575**, 75–86 (2019).
10. Goodenough, J. B. & Park, K.-S. The Li-Ion Rechargeable Battery: A Perspective. *J. Am. Chem. Soc.* **135**, 1167–1176 (2013).
11. Padhi, A. K., Nanjundaswamy, K. S. & Goodenough, J. B. Phospho-olivines as Positive-Electrode Materials for Rechargeable Lithium Batteries. *J. Electrochem. Soc.* **144**, 1188–1194 (1997).
12. Fisher, C. A. J., Hart Prieto, V. M. & Islam, M. S. Lithium Battery Materials $\mathrm{Li}M\mathrm{PO}_4$ (M = Mn, Fe, Co, and Ni): Insights into Defect Association, Transport Mechanisms, and Doping Behavior. *Chem. Mater.* **20**, 5907–5915 (2008).
13. Morgan, D., Van der Ven, A. & Ceder, G. Li Conductivity in $\mathrm{Li_xMPO_4}$ (M = Mn, Fe, Co, Ni) Olivine Materials. *Electrochem. Solid-State Lett.* **7**, A30–A32 (2004).
14. Islam, M. S., Driscoll, D. J., Fisher, C. A. J. & Slater, P. R. Atomic-Scale Investigation of Defects, Dopants, and Lithium Transport in the $\mathrm{LiFePO_4}$ Olivine-Type Battery Material. *Chem. Mater.* **17**, 5085–5092 (2005).
15. Nishimura, S. *et al.* Experimental visualization of lithium diffusion in $\mathrm{Li}_x\mathrm{FePO_4}$. *Nat. Mater.* **7**, 707–711 (2008).
16. Zhang, B. *et al.* Review: Phase transition mechanism and supercritical hydrothermal synthesis of nano lithium iron phosphate. *Ceram. Int.* **46**, 27922–27939 (2020).
17. Delmas, C., Maccario, M., Croguennec, L., Le Cras, F. & Weill, F. Lithium deintercalation in $\mathrm{LiFePO_4}$ nanoparticles via a domino-cascade model. *Nat. Mater.* **7**, 665–671 (2008).
18. Fleck, M., Federmann, H. & Pogorelov, E. Phase-field modeling of Li-insertion kinetics in single $\mathrm{LiFePO_4}$-nano-particles for rechargeable Li-ion battery application. *Comp. Mater. Sci.* **153**, 288–296 (2018).

19. Liu, C., Neale, Z. G. & Cao, G. Understanding electrochemical potentials of cathode materials in rechargeable batteries. *Materials Today* **19**, 109–123 (2016).
20. Delacourt, C., Laffont, L., Bouchet, R. & Wurm, C. Toward Understanding of Electrical Limitations (Electronic, Ionic) in $LiMPO_4$ (M = Fe, Mn) Electrode Materials. *J. Electrochem. Soc.* **152**, A193 (2005).
21. David, W. I. F., Thackeray, M. M., Bruce, P. G. & Goodenough, J. B. Lithium insertion into β-MnO_2 and the rutile-spinel transformation. *Mater. Res. Bull.* **19**, 99–106 (1984).
22. Chen, L., Huang, X., Kelder, E. & Schoonman, J. Diffusion enhancement in $Li_xMn_2O_4$. *Solid State Ionics* **76**, 91–96 (1995).
23. Barker, J., Pynenburg, R. & Koksbang, R. Determination of thermodynamic, kinetic and interfacial properties for the Li//$Li_xMn_2O_4$ system by electrochemical techniques. *J. Power Sources* **52**, 185–192 (1994).
24. Jang, D. H. & Oh, S. M. Electrolyte Effects on Spinel Dissolution and Cathodic Capacity Losses in 4 V Li/$Li_xMn_2O_4$ Rechargeable Cells. *J. Electrochem. Soc.* **144**, 3342–3348 (1997).
25. Amatucci, G. G. & Schmutz, C. N. Materials' effects on the elevated and room temperature performance of C/$LiMn_2O_4$ Li-ion batteries. *J. Power Sources* **69**, 11–25 (1997).
26. Gummow, R. J., De Kock, A. & Thackeray, M. M. Improved capacity retention in rechargeable 4 V lithium/lithium-manganese oxide (spinel) cells. *Solid State Ionics* **69**, 59–67 (1994).
27. Choi, W. & Manthiram, A. Comparison of Metal Ion Dissolutions from Lithium Ion Battery Cathodes. *J. Electrochem. Soc.* **153**, A1760 (2006).
28. Yoon, T. *et al.* Failure mechanisms of $LiNi_{0.5}Mn_{1.5}O_4$ electrode at elevated temperature. *J. Power Sources* **215**, 312–316 (2012).
29. Zhong, Q., Bonakdarpour, A., Zhang, M., Gao, Y. & Dahn, J. R. Synthesis and Electrochemistry of $LiNi_xMn_{2-x}O_4$. *J. Electrochem. Soc.* **144**, 205–213 (1997).
30. Ohzuku, T., Takeda, S. & Iwanaga, M. Solid-state redox potentials for $Li[Me_{1/2}Mn_{3/2}]O_4$ (Me: 3d-transition metal) having spinel-framework structures: a series of 5 volt materials for advanced lithium-ion batteries. *J. Power Sources* **81**, 90–94 (1999).
31. Tukamoto, H. & Yasuda, H. Preparation and electrochemical investigation of $LiMn_{2-x}Me_xO_4$ (Me: Ni, Fe, and x= 0.5, 1) cathode materials for secondary lithium batteries. *J. Power Sources* **68**, 604–608 (1997).
32. Amine, K., Tukamoto, H., Yasuda, H. & Fujita, Y. A New Three-Volt Spinel $Li_{1+x}Mn_{1.5}Ni_{0.5}O_4$ for Secondary Lithium Batteries. *J. Electrochem. Soc.* **143**, 1607–1613 (1996).
33. Song, J. *et al.* Role of Oxygen Vacancies on the Performance of $Li[Ni_{0.5-x}Mn_{1.5+x}]O_4$ ($x = 0$, 0.05, and 0.08) Spinel Cathodes for Lithium-Ion Batteries. *Chem. Mater.* **24**, 3101–3109 (2012).
34. McCalla, E., Rowe, A. W., Shunmugasundaram, R. & Dahn, J. R. Structural Study of the Li–Mn–Ni Oxide Pseudoternary System of Interest for Positive Electrodes of Li-Ion Batteries. *Chem. Mater.* **25**, 989–999 (2013).
35. Kim, J.-H., Myung, S.-T. & Sun, Y.-K. Comparative Study of $LiNi_{0.5}Mn_{1.5}O_{4-\delta}$ and $LiNi_{0.5}Mn_{1.5}O_4$ Cathodes Having Two Crystallographic Structures: *Fd-3m* and $P4_332$. *Chem. Mater.* **16**, 906–914 (2004).
36. Assat, G. & Tarascon, J.-M. Fundamental understanding and practical challenges of anionic redox activity in Li-ion batteries. *Nat. Energy* **3**, 373–386 (2018).

37. Mizushima, K., Jones, P. C., Wiseman, P. J. & Goodenough, J. B. Li_xCoO_2 (0<x<-1): A new cathode material for batteries of high energy density. *Mater. Res. Bull.* **15**, 783–789 (1980).
38. Amatucci, G. Cobalt dissolution in $LiCoO_2$-based non-aqueous rechargeable batteries. *Solid State Ionics* **83**, 167–173 (1996).
39. Chen, Z. & Dahn, J. R. Methods to obtain excellent capacity retention in $LiCoO_2$ cycled to 4.5 V. *Electrochim. Acta* **49**, 1079–1090 (2004).
40. Xu, Y. *et al.* In situ Visualization of State-of-Charge Heterogeneity within a $LiCoO_2$ Particle that Evolves upon Cycling at Different Rates. *ACS Energy Lett.* **2**, 1240–1245 (2017).
41. Zhang, W. *et al.* Collective Surface Enabling an Ultralong Life of $LiCoO_2$ at High Voltage and Elevated Temperature. *Adv. Funct. Mater.* **33**, 2304008 (2023).
42. Zhang, W. *et al.* Surface-interspersed nanoparticles induced cathode-electrolyte interphase enabling stable cycling of high-voltage $LiCoO_2$. *Nano Energy* **119**, 109031 (2024).
43. Li, W., Lee, S. & Manthiram, A. High-Nickel NMA: A Cobalt-Free Alternative to NMC and NCA Cathodes for Lithium-Ion Batteries. *Adv. Mater.* **32**, 2002718 (2020).
44. Liu, X. *et al.* Probing the Thermal-Driven Structural and Chemical Degradation of Ni-Rich Layered Cathodes by Co/Mn Exchange. *J. Am. Chem. Soc.* **142**, 19745–19753 (2020).
45. Noh, H.-J., Youn, S., Yoon, C. S. & Sun, Y.-K. Comparison of the structural and electrochemical properties of layered $Li[Ni_xCo_yMn_z]O_2$ (x = 1/3, 0.5, 0.6, 0.7, 0.8 and 0.85) cathode material for lithium-ion batteries. *J. Power Sources* **233**, 121–130 (2013).
46. Ryu, H.-H., Lim, H.-W., Lee, S. G. & Sun, Y.-K. Near-surface reconstruction in Ni-rich layered cathodes for high-performance lithium-ion batteries. *Nat. Energy* **9**, 47–56 (2023).
47. House, R. A. *et al.* First-cycle voltage hysteresis in Li-rich 3*d* cathodes associated with molecular O_2 trapped in the bulk. *Nat. Energy* **5**, 777–785 (2020).
48. Rossouw, M. H. & Thackeray, M. M. Lithium manganese oxides from Li_2MnO_3 for rechargeable lithium battery applications. *Mater. Res. Bull.* **26**, 463–473 (1991).
49. Lu, Z., MacNeil, D. D. & Dahn, J. R. Layered Cathode Materials $Li[Ni_xLi_{(1/3-2x/3)}Mn_{(2/3-x/3)}]O_2$ for Lithium-Ion Batteries. *Electrochem. Solid-State Lett.* **4**, A191–A194 (2001).
50. Numata, K., Sakaki, C. & Yamanaka, S. Synthesis of Solid Solutions in a System of $LiCoO_2$- Li_2MnO_3 for Cathode Materials of Secondary Lithium Batteries. *Chem. Lett.* **26**, 725–726 (1997).
51. Hua, W. *et al.* Lithium/Oxygen Incorporation and Microstructural Evolution during Synthesis of Li-Rich Layered $Li[Li_{0.2}Ni_{0.2}Mn_{0.6}]O_2$ Oxides. *Adv. Energy Mater.* **9**, 1803094 (2019).
52. Thackeray, M. M. *et al.* Li_2MnO_3-stabilized $LiMO_2$ (M = Mn, Ni, Co) electrodes for lithium-ion batteries. *J. Mater. Chem.* **17**, 3112 (2007).
53. Radin, M. D., Vinckeviciute, J., Seshadri, R. & Van Der Ven, A. Manganese oxidation as the origin of the anomalous capacity of Mn-containing Li-excess cathode materials. *Nat. Energy* **4**, 639–646 (2019).
54. Hy, S., Felix, F., Rick, J., Su, W.-N. & Hwang, B. J. Direct *In situ* Observation of Li_2O Evolution on Li-Rich High-Capacity Cathode Material, $Li[Ni_xLi_{(1-2x)/3}Mn_{(2-x)/3}]O_2$ ($0 \le x \le 0.5$). *J. Am. Chem. Soc.* **136**, 999–1007 (2014).
55. Muhammad, S. *et al.* Evidence of reversible oxygen participation in anomalously high capacity Li- and Mn-rich cathodes for Li-ion batteries. *Nano Energy* **21**, 172–184 (2016).

56. Yabuuchi, N., Yoshii, K., Myung, S.-T., Nakai, I. & Komaba, S. Detailed Studies of a High-Capacity Electrode Material for Rechargeable Batteries, $Li_2MnO_3-LiCo_{1/3}Ni_{1/3}Mn_{1/3}O_2$. *J. Am. Chem. Soc.* **133**, 4404–4419 (2011).
57. Koga, H. *et al.* Different oxygen redox participation for bulk and surface: A possible global explanation for the cycling mechanism of $Li_{1.20}Mn_{0.54}Co_{0.13}Ni_{0.13}O_2$. *J. Power Sources* **236**, 250–258 (2013).
58. Koga, H. *et al.* Reversible Oxygen Participation to the Redox Processes Revealed for $Li_{1.20}Mn_{0.54}Co_{0.13}Ni_{0.13}O_2$. *J. Electrochem. Soc.* **160**, A786–A792 (2013).
59. Sathiya, M. *et al.* Reversible anionic redox chemistry in high-capacity layered-oxide electrodes. *Nat. Mater.* **12**, 827–835 (2013).
60. Seo, D.-H. *et al.* The structural and chemical origin of the oxygen redox activity in layered and cation-disordered Li-excess cathode materials. *Nat. Chem.* **8**, 692–697 (2016).
61. Zuo, W. *et al.* Li-rich cathodes for rechargeable Li-based batteries: reaction mechanisms and advanced characterization techniques. *Energy Environ. Sci.* **13**, 4450–4497 (2020).
62. Li, B. & Xia, D. Anionic Redox in Rechargeable Lithium Batteries. *Adv. Mater.* **29**, 1701054 (2017).
63. Liu, S. *et al.* Reviving the lithium-manganese-based layered oxide cathodes for lithium-ion batteries. *Matter* **4**, 1511–1527 (2021).
64. Okubo, M. & Yamada, A. Molecular Orbital Principles of Oxygen-Redox Battery Electrodes. *ACS Appl. Mater. Interfaces* **9**, 36463–36472 (2017).
65. Lin, C. & Pan, F. Structural Understanding for High-Voltage Stabilization of Lithium Cobalt Oxide. *Adv. Mater.* **36**, 2307404 (2024).
66. Assat, G. *et al.* Fundamental interplay between anionic/cationic redox governing the kinetics and thermodynamics of lithium-rich cathodes. *Nat. Commun.* **8**, 2219 (2017).
67. Li, C., Zhang, N. & Gao, P. Lessons learned: how to report XPS data incorrectly about lead-halide perovskites. *Mater. Chem. Front.* **7**, 3797–3802 (2023).
68. Van Elp, J. *et al.* Electronic structure of CoO, Li-doped CoO, and $LiCoO_2$. *Phys. Rev. B* **44**, 6090–6103 (1991).
69. Dahéron, L. *et al.* Electron Transfer Mechanisms upon Lithium Deintercalation from $LiCoO_2$ to CoO_2 Investigated by XPS. *Chem. Mater.* **20**, 583–590 (2008).
70. Yang, W. & Devereaux, T. P. Anionic and cationic redox and interfaces in batteries: Advances from soft X-ray absorption spectroscopy to resonant inelastic scattering. *J. Power Sources* **389**, 188–197 (2018).
71. Smith, J. W. & Saykally, R. J. Soft X-ray Absorption Spectroscopy of Liquids and Solutions. *Chem. Rev.* **117**, 13909–13934 (2017).
72. Luo, K. *et al.* Charge-compensation in 3*d*-transition-metal-oxide intercalation cathodes through the generation of localized electron holes on oxygen. *Nat. Chem.* **8**, 684–691 (2016).
73. Chen, C.-H. *et al.* Soft X-ray absorption spectroscopy studies on the chemically delithiated commercial $LiCoO_2$ cathode material. *J. Power Sources* **174**, 938–943 (2007).
74. Yoon, W.-S. *et al.* Oxygen Contribution on Li-Ion Intercalation-Deintercalation in $LiAl_yCo_{1-y}O_2$ Investigated by O K-Edge and Co L-Edge X-Ray Absorption Spectroscopy. *J. Electrochem. Soc.* **149**, A1305–A1309 (2002).
75. Kim, M. G. *et al.* Ni and oxygen K-edge XAS investigation into the chemical bonding for lithiation of $LiyNi_{1-x}Al_xO_2$ cathode material. *Electrochim. Acta* **50**, 501–504 (2004).

76. Yoon, W.-S., Chung, K. Y., McBreen, J., Fischer, D. A. & Yang, X.-Q. Changes in electronic structure of the electrochemically Li-ion deintercalated $LiNiO_2$ system investigated by soft X-ray absorption spectroscopy. *J. Power Sources* **163**, 234–237 (2006).
77. Yoon, W.-S. *et al.* Investigation of the Charge Compensation Mechanism on the Electrochemically Li-Ion Deintercalated $Li_{1-x}Co_{1/3}Ni_{1/3}Mn_{1/3}O_2$ Electrode System by Combination of Soft and Hard X-ray Absorption Spectroscopy. *J. Am. Chem. Soc.* **127**, 17479–17487 (2005).
78. Oishi, M. *et al.* Charge compensation mechanisms in $Li_{1.16}Ni_{0.15}Co_{0.19}Mn_{0.50}O_2$ positive electrode material for Li-ion batteries analyzed by a combination of hard and soft X-ray absorption near edge structure. *J. Power Sources* **222**, 45–51 (2013).
79. Fan, Y. & Guo, Z. Stabilizing Cobalt-free Li-rich Layered Oxide Cathodes through Oxygen Lattice Regulation by Two-phase Ru Doping. *Angew. Chem. Int. Ed.* **62**, e202213806 (2023).
80. Zhu, Z. *et al.* Gradient Li-rich oxide cathode particles immunized against oxygen release by a molten salt treatment. *Nat. Energy* **4**, 1049–1058 (2019).
81. Zhao, E. *et al.* Local structure adaptability through multi cations for oxygen redox accommodation in Li-Rich layered oxides. *Energy Storage Mater.* **24**, 384–393 (2020).
82. Xu, J. *et al.* Elucidating anionic oxygen activity in lithium-rich layered oxides. *Nat. Commun.* **9**, 947 (2018).
83. House, R. A. *et al.* Superstructure control of first-cycle voltage hysteresis in oxygen-redox cathodes. *Nature* **577**, 502–508 (2020).
84. Gent, W. E. *et al.* Coupling between oxygen redox and cation migration explains unusual electrochemistry in lithium-rich layered oxides. *Nat. Commun.* **8**, 2091 (2017).
85. House, R. A. *et al.* Detection of trapped molecular O_2 in a charged Li-rich cathode by Neutron PDF. *Energy Environ. Sci.* **15**, 376–383 (2022).
86. Marie, J.-J. *et al.* Trapped O_2 and the origin of voltage fade in layered Li-rich cathodes. *Nat. Mater.* **23**, 818–825 (2024).
87. Århammar, C. *et al.* Unveiling the complex electronic structure of amorphous metal oxides. *Proc. Natl. Acad. Sci. U.S.A.* **108**, 6355–6360 (2011).
88. Juelsholt, M. *et al.* Does trapped O_2 form in the bulk of $LiNiO_2$ during charging? *Energy Environ. Sci.* **17**, 2530–2540 (2024).
89. Thackeray, M. M. *et al.* Li_2MnO_3-stabilized $LiMO_2$ (M = Mn, Ni, Co) electrodes for lithium-ion batteries. *J. Mater. Chem.* **17**, 3112 (2007).
90. Hua, W. *et al.* Structural insights into the formation and voltage degradation of lithium- and manganese-rich layered oxides. *Nat. Commun.* **10**, 5365 (2019).
91. Xu, S. *et al.* Multi-angle tracking synthetic kinetics of phase evolution in Li-rich Mn-based cathodes. *Energy Environ. Sci.* **17**, 3807–3818 (2024).
92. Perez, A. J. *et al.* Approaching the limits of cationic and anionic electrochemical activity with the Li-rich layered rocksalt Li_3IrO_4. *Nat. Energy* **2**, 954–962 (2017).
93. Hu, E. *et al.* Evolution of redox couples in Li- and Mn-rich cathode materials and mitigation of voltage fade by reducing oxygen release. *Nat. Energy* **3**, 690–698 (2018).
94. Hong, J. *et al.* Metal–oxygen decoordination stabilizes anion redox in Li-rich oxides. *Nat. Mater.* **18**, 256–265 (2019).
95. Sathiya, M. *et al.* Origin of voltage decay in high-capacity layered oxide electrodes. *Nat. Mater.* **14**, 230–238 (2015).

96. Liu, T. *et al.* Origin of structural degradation in Li-rich layered oxide cathode. *Nature* **606**, 305–312 (2022).
97. Guo, X. *et al.* Weak σ–π–σ interaction stabilizes oxygen redox towards high-performance Li–rich layered oxide cathodes. *Nano Energy* **123**, 109390 (2024).
98. Li, J. *et al.* Tuning Li_2MnO_3-Like Domain Size and Surface Structure Enables Highly-stabilized Li-Rich Layered Oxide Cathodes. *ACS Nano* **17**, 16827–16839 (2023).
99. Zhang, M. *et al.* Formulating Local Environment of Oxygen Mitigates Voltage Hysteresis in Li-Rich Materials. *Adv. Mater.* **36**, 2311814 (2024).
100. Paulsen, J. M., Thomas, C. L. & Dahn, J. R. Layered Li-Mn-Oxide with the O2 Structure: A Cathode Material for Li-Ion Cells Which Does Not Convert to Spinel. *J. Electrochem. Soc.* **146**, 3560–3565 (1999).
101. Eum, D. *et al.* Voltage decay and redox asymmetry mitigation by reversible cation migration in lithium-rich layered oxide electrodes. *Nat. Mater.* **19**, 419–427 (2020).
102. Luo, D. *et al.* A Li-rich layered oxide cathode with negligible voltage decay. *Nat. Energy* **8**, 1078–1087 (2023).
103. Wu, T. *et al.* Full Concentration Gradient-Tailored Li-Rich Layered Oxides for High-Energy Lithium-Ion Batteries. *Adv. Mater.* **33**, 2001358 (2021).
104. Ju, X. *et al.* The full gradient design in Li-rich cathode for high performance lithium ion batteries with reduced voltage decay. *J. Power Sources* **437**, 226902 (2019).
105. Shi, J.-L. *et al.* Mitigating Voltage Decay of Li-Rich Cathode Material via Increasing Ni Content for Lithium-Ion Batteries. *ACS Appl. Mater. Interfaces* **8**, 20138–20146 (2016).
106. Ku, K. *et al.* Suppression of Voltage Decay through Manganese Deactivation and Nickel Redox Buffering in High-Energy Layered Lithium-Rich Electrodes. *Adv. Energy Mater.* **8**, 1800606 (2018).
107. Li, B. *et al.* Decoupling the roles of Ni and Co in anionic redox activity of Li-rich NMC cathodes. *Nat. Mater.* **22**, 1370–1379 (2023).
108. Chong, S., Liu, Y., Yan, W. & Chen, Y. Effect of valence states of Ni and Mn on the structural and electrochemical properties of $Li_{1.2}Ni_xMn_{0.8-x}O_2$ cathode materials for lithium-ion batteries. *RSC Adv.* **6**, 53662–53668 (2016).
109. Guo, L. *et al.* Improved electrochemical activity of the Li_2MnO_3-like superstructure in high-nickel Li-rich layered oxide $Li_{1.2}Ni_{0.4}Mn_{0.4}O_2$ and its enhanced performances via tungsten doping. *Electrochim. Acta* **370**, 137808 (2021).
110. Knight, J. C. & Manthiram, A. Effect of nickel oxidation state on the structural and electrochemical characteristics of lithium-rich layered oxide cathodes. *J. Mater. Chem. A* **3**, 22199–22207 (2015).
111. Qi, G. *et al.* Impact of Ni Content on the Electrochemical Performance of the Co-Free, Li and Mn-Rich Layered Cathode Materials. *Electrochem* **4**, 21–30 (2023).
112. Dippel, A.-C. *et al.* Beamline P02.1 at PETRA III for high-resolution and high-energy powder diffraction. *J. Synchrotron Rad.* **22**, 675–687 (2015).
113. Schökel, A. *et al.* Multi-analyser detector (MAD) for high-resolution and high-energy powder X-ray diffraction. *J. Synchrotron Rad.* **28**, 146–157 (2021).
114. Basham, M. *et al. Data Analysis WorkbeNch* (*DAWN*). *J. Synchrotron Rad.* **22**, 853–858 (2015).
115. Rodríguez-Carvajal, J. Recent advances in magnetic structure determination by neutron powder diffraction. *Physica B: Condensed Matter* **192**, 55–69 (1993).

116. Farrow, C. L. *et al.* PDFfit2 and PDFgui: computer programs for studying nanostructure in crystals. *J. Phys.: Condens. Matter* **19**, 335219 (2007).
117. Momma, K. & Izumi, F. *VESTA 3* for three-dimensional visualization of crystal, volumetric and morphology data. *J. Appl. Crystallogr.* **44**, 1272–1276 (2011).
118. Ravel, B. & Newville, M. *ATHENA* , *ARTEMIS* , *HEPHAESTUS* : data analysis for X-ray absorption spectroscopy using *IFEFFIT*. *J. Synchrotron Rad.* **12**, 537–541 (2005).
119. Schulz, C. *et al.* Characterization of the soft X-ray spectrometer PEAXIS at BESSY II. *J. Synchrotron Rad.* **27**, 238–249 (2020).
120. Massiot, D., Fayon, F., Capron, M., King, I. & Lecalve, S. phanie. Modelling one- and two-dimensional solid-state NMR spectra. *J. Electrochem. Soc.* **40**, 70–76 (2002).
121. Kresse, G. & Hafner, J. *Ab initio* molecular dynamics for liquid metals. *Phys. Rev. B* **47**, 558–561 (1993).
122. Kresse, G. & Furthmüller, J. Efficiency of ab-initio total energy calculations for metals and semiconductors using a plane-wave basis set. *Comp. Mater. Sci.* **6**, 15–50 (1996).
123. Kresse, G. & Furthmüller, J. Efficient iterative schemes for *ab initio* total-energy calculations using a plane-wave basis set. *Phys. Rev. B* **54**, 11169–11186 (1996).
124. Kresse, G. & Joubert, D. From ultrasoft pseudopotentials to the projector augmented-wave method. *Phys. Rev. B* **59**, 1758–1775 (1999).
125. Furness, J. W., Kaplan, A. D., Ning, J., Perdew, J. P. & Sun, J. Accurate and Numerically Efficient r^2SCAN Meta-Generalized Gradient Approximation. *J. Phys. Chem. Lett.* **11**, 8208–8215 (2020).
126. Long, O. Y., Sai Gautam, G. & Carter, E. A. Evaluating optimal U for 3*d* transition-metal oxides within the SCAN+U framework. *Phys. Rev. Materials* **4**, 045401 (2020).
127. Caldeweyher, E., Bannwarth, C. & Grimme, S. Extension of the D3 dispersion coefficient model. *J. Chem. Phys.* **147**, 034112 (2017).
128. Dovesi, R. *et al.* Quantum-mechanical condensed matter simulations with CRYSTAL. *Wires. Comput. Mol. Sci.* **8**, e1360 (2018).
129. Bredow, T. & Gerson, A. R. Effect of exchange and correlation on bulk properties of MgO, NiO, and CoO. *Phys. Rev. B* **61**, 5194–5201 (2000).
130. Lumey, M.-W. & Dronskowski, R. The Electronic Structure of Tantalum Oxynitride and the Falsification ofα-TaON. *Z. Anorg. Allg. Chem.* **629**, 2173–2179 (2003).
131. Grimme, S., Antony, J., Ehrlich, S. & Krieg, H. A consistent and accurate *ab initio* parametrization of density functional dispersion correction (DFT-D) for the 94 elements H-Pu. *J. Chem. Phys.* **132**, 154104 (2010).
132. Grimme, S., Ehrlich, S. & Goerigk, L. Effect of the damping function in dispersion corrected density functional theory. *J. Comput. Chem.* **32**, 1456–1465 (2011).
133. Grimme, S., Hansen, A., Brandenburg, J. G. & Bannwarth, C. Dispersion-Corrected Mean-Field Electronic Structure Methods. *Chem. Rev.* **116**, 5105–5154 (2016).
134. Kunz, S. L. & Bredow, T. On the stability of *M*OPO_4 structure types with M: V, Mo, Nb, W, Ta, Sb. *J. Solid State Chem.* **312**, 123221 (2022).
135. Oliveira, D. V., Laun, J., Peintinger, M. F. & Bredow, T. BSSE-Correction Scheme for Consistent Gaussian Basis Sets of Double- and Triple-Zeta Valence with Polarization Quality for Solid-State Calculations. *J. Comput. Chem.* **40**, 2364–2376 (2019).

136. Peintinger, M. F., Oliveira, D. V. & Bredow, T. Consistent Gaussian Basis Sets of Triple-Zeta Valence with Polarization Quality for Solid-State Calculations. *J. Comput. Chem.* **34**, 451–459 (2013).

137. Pisani, C. & Aprà, M. Density matrix of crystalline systems. I. Long-range behavior and related computational problems. *Int. J. Quantum. Chem.* **38**, 395–417 (1990).

138. Okhotnikov, K., Charpentier, T. & Cadars, S. Supercell program: a combinatorial structure-generation approach for the local-level modeling of atomic substitutions and partial occupancies in crystals. *J. Cheminf.* **8**, 17 (2016).

139. Liu, Y. *et al.* Modulating the Surface Ligand Orientation for Stabilized Anionic Redox in Li-Rich Oxide Cathodes. *Adv. Energy Mater.* **11**, 2003479 (2021).

140. Li, B. *et al.* Capturing dynamic ligand-to-metal charge transfer with a long-lived cationic intermediate for anionic redox. *Nat. Mater.* **21**, 1370–1379 (2022).

141. Kleiner, K. *et al.* On the Origin of Reversible and Irreversible Reactions in $LiNi_xCo_{(1-x)/2}Mn_{(1-x)/2}O_2$. *J. Electrochem. Soc.* **168**, 120533 (2021).

142. Luo, K. *et al.* Anion Redox Chemistry in the Cobalt Free 3d Transition Metal Oxide Intercalation Electrode $Li[Li_{0.2}Ni_{0.2}Mn_{0.6}]O_2$. *J. Am. Chem. Soc.* **138**, 11211–11218 (2016).

143. Merz, M., Ying, B., Nagel, P., Schuppler, S. & Kleiner, K. Reversible and Irreversible Redox Processes in Li-Rich Layered Oxides. *Chem. Mater.* **33**, 9534–9545 (2021).

144. Zhao, E. *et al.* Local structure adaptability through multi cations for oxygen redox accommodation in Li-Rich layered oxides. *Energy Storage Mater.* **24**, 384–393 (2020).

145. House, R. A. *et al.* Covalency does not suppress O_2 formation in 4d and 5d Li-rich O-redox cathodes. *Nat. Commun.* **12**, 2975 (2021).

146. House, R. A. *et al.* The role of O_2 in O-redox cathodes for Li-ion batteries. *Nat. Energy* **6**, 781–789 (2021).

147. House, R. A. *et al.* Delocalized electron holes on oxygen in a battery cathode. *Nat. Energy* **8**, 351–360 (2023).

148. Li, Q. *et al.* Improving the oxygen redox reversibility of Li-rich battery cathode materials via Coulombic repulsive interactions strategy. *Nat. Commun.* **13**, 1123 (2022).

149. Maitra, U. *et al.* Oxygen redox chemistry without excess alkali-metal ions in $Na_{2/3}[Mg_{0.28}Mn_{0.72}]O_2$. *Nat. Chem.* **10**, 288–295 (2018).

150. Grey, C. P. & Dupré, N. NMR Studies of Cathode Materials for Lithium-Ion Rechargeable Batteries. *Chem. Rev.* **104**, 4493–4512 (2004).

151. Pecher, O., Carretero-González, J., Griffith, K. J. & Grey, C. P. Materials' Methods: NMR in Battery Research. *Chem. Mater.* **29**, 213–242 (2017).

152. Shimoda, K. *et al.* Sequential delithiation behavior and structural rearrangement of a nanoscale composite-structured $Li_{1.2}Ni_{0.2}Mn_{0.6}O_2$ during charge–discharge cycles. *Sci. Rep.* **10**, 10048 (2020).

153. Li, X. *et al.* Lithiation and Delithiation Dynamics of Different Li Sites in Li-Rich Battery Cathodes Studied by *Operando* Nuclear Magnetic Resonance. *Chem. Mater.* **29**, 8282–8291 (2017).

154. Dogan, F. *et al.* Solid State NMR Studies of Li_2MnO_3 and Li-Rich Cathode Materials: Proton Insertion, Local Structure, and Voltage Fade. *J. Electrochem. Soc.* **162**, A235–A243 (2015).

155. Zhang, B. *et al.* Role of Substitution Elements in Enhancing the Structural Stability of Li-Rich Layered Cathodes. *J. Am. Chem. Soc.* **145**, 8700–8713 (2023).

156. Yoon, W.-S. *et al.* Investigation of the Local Structure of the $LiNi_{0.5}Mn_{0.5}O_2$ Cathode Material during Electrochemical Cycling by X-Ray Absorption and NMR Spectroscopy. *Electrochem. Solid-State Lett.* **5**, A263–A266 (2002).

157. Bianchini, M. *et al.* From $LiNiO_2$ to Li_2NiO_3 : Synthesis, Structures and Electrochemical Mechanisms in Li-Rich Nickel Oxides. *Chem. Mater.* **32**, 9211–9227 (2020).

158. Pauling, L. The principles determining the structure of complex ionic crystals. *J. Am. Chem. Soc.* **51**, 1010–1026 (1929).

159. Yin, C. *et al.* Structural insights into composition design of Li-rich layered cathode materials for high-energy rechargeable battery. *Materials Today* **51**, 15–26 (2021).

160. Yang, Y. *et al.* Cation configuration in transition-metal layered oxides. *Matter* **5**, 3869–3882 (2022).

161. Kang, K., Meng, Y. S., Bréger, J., Grey, C. P. & Ceder, G. Electrodes with High Power and High Capacity for Rechargeable Lithium Batteries. *Science* **311**, 977–980 (2006).

162. Mohanty, D. Structural transformation of a lithium-rich $Li_{1.2}Co_{0.1}Mn_{0.55}Ni_{0.15}O_2$ cathode during high voltage cycling resolved by in situ X-ray diffraction. *J. Power Sources* **229**, 239–248 (2013).

163. Lin, F. *et al.* Surface reconstruction and chemical evolution of stoichiometric layered cathode materials for lithium-ion batteries. *Nat. Commun.* **5**, 3529 (2014).

164. Seo, J. H. *et al.* Electron Beam-Induced Effects on a Ni-Rich Layered Cathode Material: A Comprehensive Investigation Using STEM and EELS. *J. Phys. Chem. C* **128**, 9099–9104 (2024).

165. Goodenough, J. B. & Kim, Y. Challenges for Rechargeable Li Batteries. *Chem. Mater.* **22**, 587–603 (2010).

166. Manthiram, A. & Goodenough, J. B. Layered lithium cobalt oxide cathodes. *Nat. Energy* **6**, 323–323 (2021).

167. Goodenough, J. B. & Park, K.-S. The Li-Ion Rechargeable Battery: A Perspective. *J. Am. Chem. Soc.* **135**, 1167–1176 (2013).

168. Kim, J. & Cho, J. Prospect and Reality of Ni-Rich Cathode for Commercialization. *Adv. Energy Mater.* **8**, 1702028 (2018).

169. Jiang, M., Danilov, D. L., Eichel, R.-A. & Notten, P. H. L. A Review of Degradation Mechanisms and Recent Achievements for Ni-Rich Cathode-Based Li-Ion Batteries. *Adv. Energy Mater.* **11**, 2103005 (2021).

170. Jung, R. *et al.* Effect of Ambient Storage on the Degradation of Ni-Rich Positive Electrode Materials (NMC811) for Li-Ion Batteries. *J. Electrochem. Soc.* **165**, A132–A141 (2018).

171. Liu, H. *et al.* Enabling Superior Electrochemical Performance of Lithium-Rich $Li_{1.2}Ni_{0.2}Mn_{0.6}O_2$ Cathode Materials by Surface Integration. *Ind. Eng. Chem. Res.* **59**, 19312–19321 (2020).

172. Liu, T. *et al.* Insights into the enhanced cycling stability of cobalt-free single-crystal layered oxide cathodes at elevated voltage. *J. Mater. Chem. A* **12**, 12702–12711 (2024).

173. Chen, S. *et al.* Slightly Li-enriched chemistry enabling super stable $LiNi_{0.5}Mn_{0.5}O_2$ cathodes under extreme conditions. *Chem. Sci.* (2024) doi:10.1039/d4sc03805c.

174. Hinuma, Y., Meng, Y. S., Kang, K. & Ceder, G. Phase Transitions in the $LiNi_{0.5}Mn_{0.5}O_2$ System with Temperature. *Chem. Mater.* **19**, 1790–1800 (2007).

175. Bréger, J. *et al.* Effect of High Voltage on the Structure and Electrochemistry of $LiNi_{0.5}Mn_{0.5}O_2$: A Joint Experimental and Theoretical Study. *Chem. Mater.* **18**, 4768–4781 (2006).

176. Aiken, C. P. *et al.* $Li[Ni_{0.5}Mn_{0.3}Co_{0.2}]O_2$ as a Superior Alternative to $LiFePO_4$ for Long-Lived Low Voltage Li-Ion Cells. *J. Electrochem. Soc.* **169**, 050512 (2022).

177. Li, J. *et al.* Synthesis of Single Crystal $LiNi_{0.5}Mn_{0.3}Co_{0.2}O_2$ for Lithium Ion Batteries. *J. Electrochem. Soc.* **164**, A3529–A3537 (2017).

178. Jung, S. *et al.* Understanding the Degradation Mechanisms of $LiNi_{0.5}Co_{0.2}Mn_{0.3}O_2$ Cathode Material in Lithium Ion Batteries. *Adv. Energy Mater.* **4**, 1300787 (2014).

179. Liang, L. *et al.* Chemomechanically Stable Small Single-crystal Mo-doped $LiNi_{0.6}Co_{0.2}Mn_{0.2}O_2$ Cathodes for Practical 4.5 V-class Pouch-type Li-ion Batteries. *Angew. Chem. Int. Ed.* **62**, e202216155 (2023).

180. Bian, X., Zhang, R. & Yang, X. Effects of Structure and Magnetism on the Electrochemistry of the Layered $Li_{1+x}(Ni_{0.5}Mn_{0.5})_{1-x}O_2$ Cathode Material. *Inorg. Chem.* **59**, 17535–17543 (2020).

181. Yang, K., Fan, L.-Z., Guo, J. & Qu, X. Significant improvement of electrochemical properties of AlF_3-coated $LiNi_{0.5}Co_{0.2}Mn_{0.3}O_2$ cathode materials. *Electrochim. Acta* **63**, 363–368 (2012).

182. Zhang, R. *et al.* Long-life lithium-ion batteries realized by low-Ni, Co-free cathode chemistry. *Nat. Energy* **8**, 695–702 (2023).

183. Kresse, G. & Furthmüller, J. Efficiency of ab-initio total energy calculations for metals and semiconductors using a plane-wave basis set. *Comp. Mater. Sci.* **6**, 15–50 (1996).

184. Blöchl, P. E. Projector augmented-wave method. *Phys. Rev. B* **50**, 17953–17979 (1994).

185. Ernzerhof, M. & Scuseria, G. E. Assessment of the Perdew–Burke–Ernzerhof exchange-correlation functional. *J. Chem. Phys.* **110**, 5029–5036 (1999).

186. Grimme, S., Antony, J., Ehrlich, S. & Krieg, H. A consistent and accurate *ab initio* parametrization of density functional dispersion correction (DFT-D) for the 94 elements H-Pu. *J. Chem. Phys.* **132**, 154104 (2010).

187. Xu, H. Atomic-scale insights into the electrochemical mechanisms of aluminum-sulfur batteries: A first-principles study of Al-S clusters on graphene. *Chemical Physics Letters* **851**, 141492 (2024).

188. Xu, H. & Guan, D. Exceptional Anisotropic Noncovalent Interactions inUltrathin Nanorods: TheTerminal σ-Hole. *ACS Appl. Mater. Interfaces* **14**, 51190–51199 (2022).

189. Ji, X. *et al.* Suppressing oxygen vacancies on the surface of Li-rich material as a high-energy cathode via high oxygen affinity $Ca_{0.95}Bi_{0.05}MnO_3$ coating. *Electrochim. Acta* **421**, 140465 (2022).

190. Yang, T. *et al.* Ultrahigh-nickel layered cathode with cycling stability for sustainable lithium-ion batteries. *Nat. Sustain.* (2024) doi:10.1038/s41893-024-01402-x.

191. Dogan, F. *et al.* Solid State NMR Studies of Li_2MnO_3 and Li-Rich Cathode Materials: Proton Insertion, Local Structure, and Voltage Fade. *J. Electrochem. Soc.* **162**, A235–A243 (2015).

192. Ates, M. N., Mukerjee, S. & Abraham, K. M. A high rate Li-rich layered MNC cathode material for lithium-ion batteries. *RSC Adv.* **5**, 27375–27386 (2015).

193. Huang, W. *et al.* Unrecoverable lattice rotation governs structural degradation of single-crystalline cathodes. *Science* **384**, 912–919 (2024).
194. Li, N. *et al.* Layered-rocksalt intergrown cathode for high-capacity zero-strain battery operation. *Nat. Commun.* **12**, 2348 (2021).
195. Zhao, C. *et al.* Suppressing strain propagation in ultrahigh-Ni cathodes during fast charging via epitaxial entropy-assisted coating. *Nat. Energy* **9**, 345–356 (2024).
196. Song, J. & Xia, D. A High-Performance Li–Mn–O Li-rich Cathode Material with Rhombohedral Symmetry via Intralayer Li/Mn Disordering. *Adv. Mater.* **32**, 2000190 (2020).
197. Yoon, M. *et al.* Reactive boride infusion stabilizes Ni-rich cathodes for lithium-ion batteries. *Nat. Energy* **6**, 362–371 (2021).

Appendix

Anlage 5b

Versicherung gemäß § 13 Absatz 2 Satz 2 Ziffer 5 der Promotionsordnung des Karlsruher Instituts für Technologie (KIT) für die KIT-Fakultät für Chemie und Biowissenschaften

1. Einen erheblichen Verstoß gegen die Grundsätze guter wissenschaftlicher Praxis habe ich bislang nicht begangen.

2. Es gab bisher keine Promotionseignungsprüfung oder gleichwertige Prüfung an einer Universität oder dieser gleichgestellten Hochschule, an der ich erfolglos teilgenommen habe.

3. Diesem Promotionsverfahren gingen keine anderen Promotionsverfahren voran und ich bin in keinen weiteren Promotionsverfahren Kandidat/-in.

5. Ein entgeltliches Vertragsverhältnis, das eine gewerbliche Promotionsberatung zum Gegenstand hat und zur Unselbstständigkeit zumindest einer Promotionsleistung führen kann, besteht bzw. bestand nicht.

6. Die „Regeln zur Sicherung guter wissenschaftlicher Praxis am Karlsruher Institut für Technologie (KIT)“ habe ich beachtet.

7. In die Dissertation wurden Vorveröffentlichungen einbezogen, bei denen ich im Rahmen einer Mitautorenschaft jeweils einen signifikanten Teil selbstständig erbracht habe. Eine Aufstellung mit den Angaben:

Autoren/Autorinnen:

Titel der Vorveröffentlichung:

Veröffentlicht in:

Ausführliche Darlegung des selbstständig erbrachten, signifikanten Beitrages der Vorveröffentlichung oder der zur Veröffentlichung eingereichten Arbeit:

ist dieser Erklärung beigefügt. Die Aufstellung ist Bestandteil dieser Erklärung.

8. Die Dissertation oder Teile davon wurden nicht bei einer anderen Fakultät als Dissertation eingereicht.

9. Die Richtigkeit der vorstehenden Erklärungen bestätige ich.

Ort und Datum Unterschrift

Manuscript 1 – (Results and Discussion in Chapter 3)

Authors: Hao Liu, Weibo Hua, Sylvia Kunz, Matteo Bianchini, Hang Li, Jiali Peng, Jing Lin, Oleksandr Dolotko, Thomas Bergfeldt, Kai Wang, Christian Kübel, Peter Nagel, Stefan Schuppler, Michael Merz, Bixian Ying, Karin Kleiner, Stefan Mangold, Deniz Wong, Volodymyr Baran, Michael Knapp, Helmut Ehrenberg, and Sylvio Indris

Publication title: Tailoring superstructure units for improved oxygen redox activity in Li-rich layered oxide battery's positive electrodes

Published in: *Nature communications.* Accepted.

The co-authors listed in Table 1 were involved in the implementation and evaluation of some measurements.

Table 1: Statement of co-author contributions

Co-authors	Measurement method
Sylvia Kunz and Matteo Bianchini	Density functional theory calculations
Hang Li	Nuclear magnetic resonance spectroscopy
Jing Lin	Pair distribution function
Oleksandr Dolotko	In-situ X-ray diffraction
Thomas Bergfeldt	Inductively coupled plasma-optical emission spectroscopy
Kai Wang, Christian Kübel, and Weibo Hua	Transmission electron microscopy
Peter Nagel, Stefan Schuppler, Michael Merz, Bixian Ying, and Karin Kleiner	Soft X-ray absorption spectroscopy
Jiali Peng and Stefan Mangold	X-ray absorption spectroscopy
Deniz Wong	Resonant inelastic X-ray scattering
Michael Knapp and Volodymyr Baran	Synchrotron X-ray diffraction
Bijian Deng	Scanning electron microscopy

Other co-authors:

Sylvio Indris and Helmut Ehrenberg supervised the work and contributed to the completion of the manuscript.

Description of the contribution made independently:

Practical work:

This publication based on research focused on the relationship between oxygen redox activity and honeycomb superstructure units of Li-rich cathodes. I independently conducted the synthesis of the materials, assembled the batteries, and performed the electrochemical performance measurements. Additionally, I prepared all ex-situ electrodes for X-ray absorption spectroscopy, Synchrotron X-ray diffraction, Nuclear magnetic resonance spectroscopy, Resonant inelastic X-ray scattering, Transmission electron microscopy, and Pair distribution function measurements.

Measurements:

Sylvia Kunz and Matteo Bianchini performed the Density functional theory calculations. Hang Li performed Nuclear magnetic resonance spectroscopy measurements. Jing Lin performed Pair distribution function measurements. In-situ X-ray diffraction experiments were carried out by me with the help of Oleksandr Dolotko. Thomas Bergfeldt conducted Inductively coupled plasma-optical emission spectroscopy measurements. Kai Wang, Christian Kübel, and Weibo Hua performed Transmission electron microscopy measurements. Peter Nagel, Stefan Schuppler, Michael Merz conducted Soft X-ray absorption spectroscopy measurements and Bixian Ying and Karin Kleiner provide corresponding data analysis. Bijian Deng carried out the Scanning electron microscopy experiments. Stefan Mangold conducted X-ray absorption spectroscopy measurements. Deniz Wong performed Resonant inelastic X-ray scattering measurements. Volodymyr Baran carried out the Synchrotron X-ray diffraction measurements. Michael Knapp provided help for the Rietveld refinement. The evaluation and analysis of the measurements listed in Table 1 were coordinated by me and discussed together.

Creating the manuscript:

Essentially, I conceived the idea and wrote the draft with input from Sylvio Indris, Weibo Hua, and Helmut Ehrenberg. All co-authors contributed to interpreting the findings, reviewing, and revising the manuscript.

Manuscript 2 – (Results and Discussion in Chapter 4)

Authors: Hao Liu, Weibo Hua, Hang Li, Bixian Ying, Karin Kleiner, Jing Lin, Hang Xu, Bijian Deng, Deniz Wong, Thomas Bergfeldt, Stefan Mangold, Peter Nagel, Stefan Schuppler, Michael Merz, Volodymyr Baran, Clemens Ritter, Yongjian Li, Ning Li, Michael Knapp, Helmut Ehrenberg, and Sylvio Indris

Publication title: Integrating Ni-pinned honeycomb structures enables high-performance lithium-ion layered oxide cathodes

Published in: Submitted.

The co-authors listed in Table 2 were involved in the implementation and evaluation of some measurements.

Table 2: Statement of co-author contributions

Co-authors	Measurement method
Weibo Hua	In-situ X-ray absorption spectroscopy
Hang Li	Nuclear magnetic resonance spectroscopy
Jing Lin and Clemens Ritter	Neutron powder diffraction
Hang Xu	Differential electrochemical mass spectroscopy
Thomas Bergfeldt	Inductively coupled plasma-optical emission spectroscopy
Yongjian Li and Ning Li	Scanning transmission electron microscopy
Peter Nagel, Stefan Schuppler, Michael Merz, Bixian Ying, and Karin Kleiner	Soft X-ray absorption spectroscopy
Jiali Peng and Stefan Mangold	X-ray absorption spectroscopy
Deniz Wong	Resonant inelastic X-ray scattering
Michael Knapp and Volodymyr Baran	In-situ synchrotron X-ray diffraction
Bijian Deng	Scanning electron microscopy
Hengyue Xu	Density functional theory calculations

Other co-authors:

Sylvio Indris and Helmut Ehrenberg supervised the work and contributed to the completion of the manuscript.

Description of the contribution made independently:

Practical work:

This publication based on research focused on the design of high-performance lithium-ion layered oxide cathodes with stable oxygen redox chemistry. I independently conducted the synthesis of the materials, assembled the batteries, and performed the electrochemical performance measurements. Additionally, I prepared all ex-situ electrodes for X-ray absorption spectroscopy, scanning transmission electron microscopy, nuclear magnetic resonance spectroscopy, and resonant inelastic X-ray scattering measurements.

Measurements:

Hang Li performed Nuclear magnetic resonance spectroscopy measurements. Jing Lin and Clemens Ritter performed Neutron powder diffraction measurements. Peter Nagel, Stefan Schuppler, Michael Merz conducted Soft X-ray absorption spectroscopy measurements and Bixian Ying and Karin Kleiner provide corresponding data analysis. Hang Xu conducted Differential electrochemical mass spectroscopy measurements. Bijian Deng carried out the Scanning electron microscopy experiments. Deniz Wong performed Resonant inelastic X-ray scattering measurements. Thomas Bergfeldt conducted Inductively coupled plasma-optical emission spectroscopy measurements. Stefan Mangold conducted X-ray absorption spectroscopy measurements. In-situ X-ray diffraction experiments were carried out by me with the help of Volodymyr Baran. Yongjian Li and Ning Li conducted Scanning transmission electron microscopy measurements. Hengyue Xu performed the Density functional theory calculations. Michael Knapp and Weibo Hua provided help for the Rietveld refinement.

The evaluation and analysis of the measurements listed in Table 2 were coordinated by me and discussed together.

Creating the manuscript:

Essentially, I conceived the idea and wrote the draft with input from Sylvio Indris and Helmut Ehrenberg. All co-authors contributed to interpreting the findings, reviewing, and revising the manuscript.

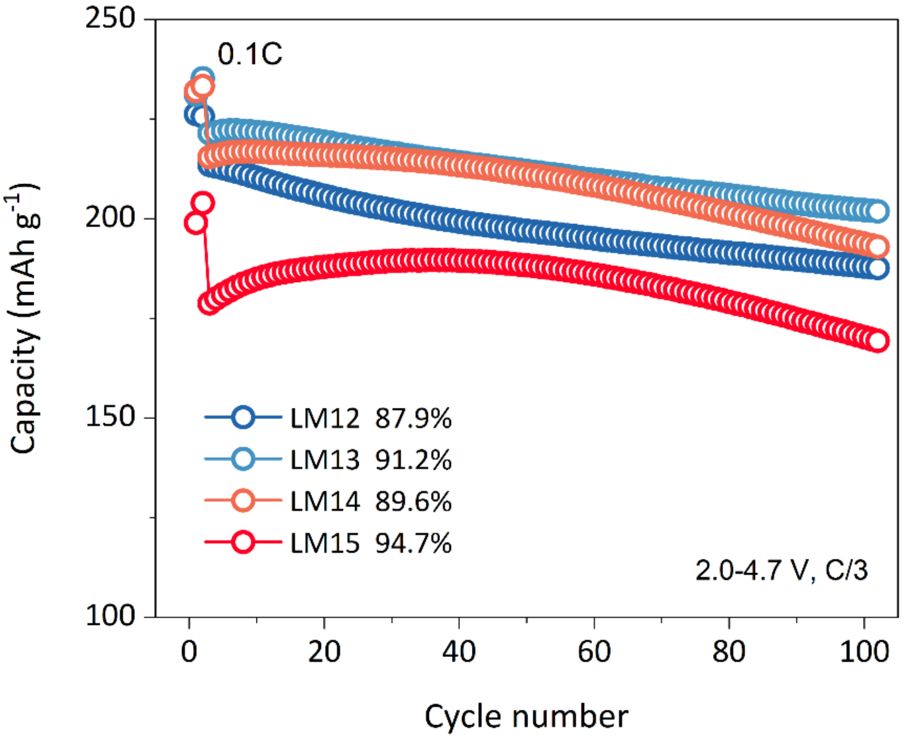

Figure A1 Cycling performance of LM12, LM13, LM14, and LM15 at C/3 (formation at C/10 for two cycles) in the voltage range of 2.0-4.7 V at 25°C.

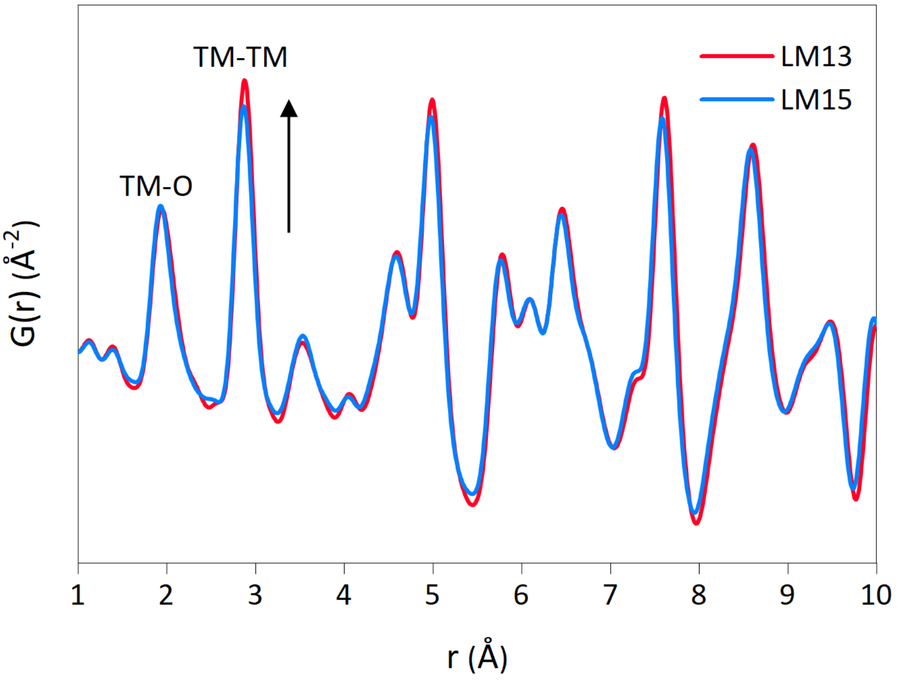

Figure A2 PDF patterns of LM15 and LM13.

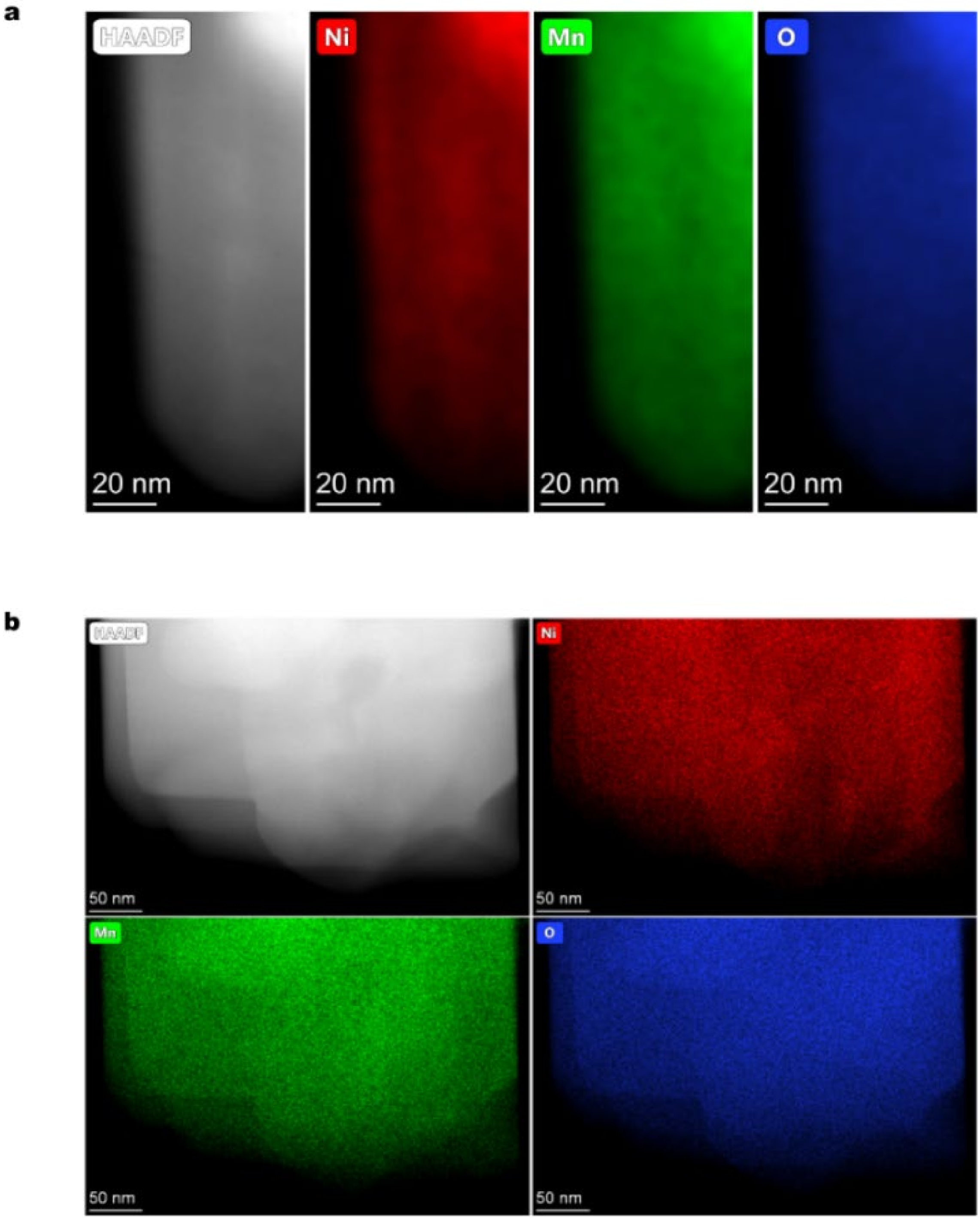

Figure A3 TEM-EDS mapping images of LM15 (a) and LM13 (b).

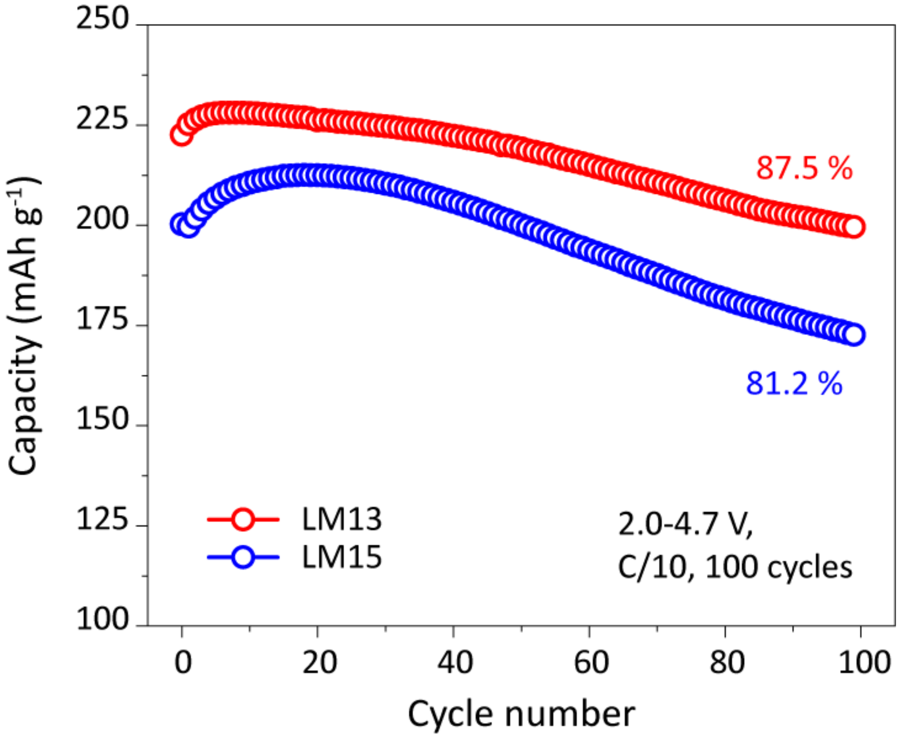

Figure A4 Cycling performance of LM13 and LM15 at C/10 (formation at C/10 for two cycles) in the voltage range of 2.0-4.7 V at 25°C.

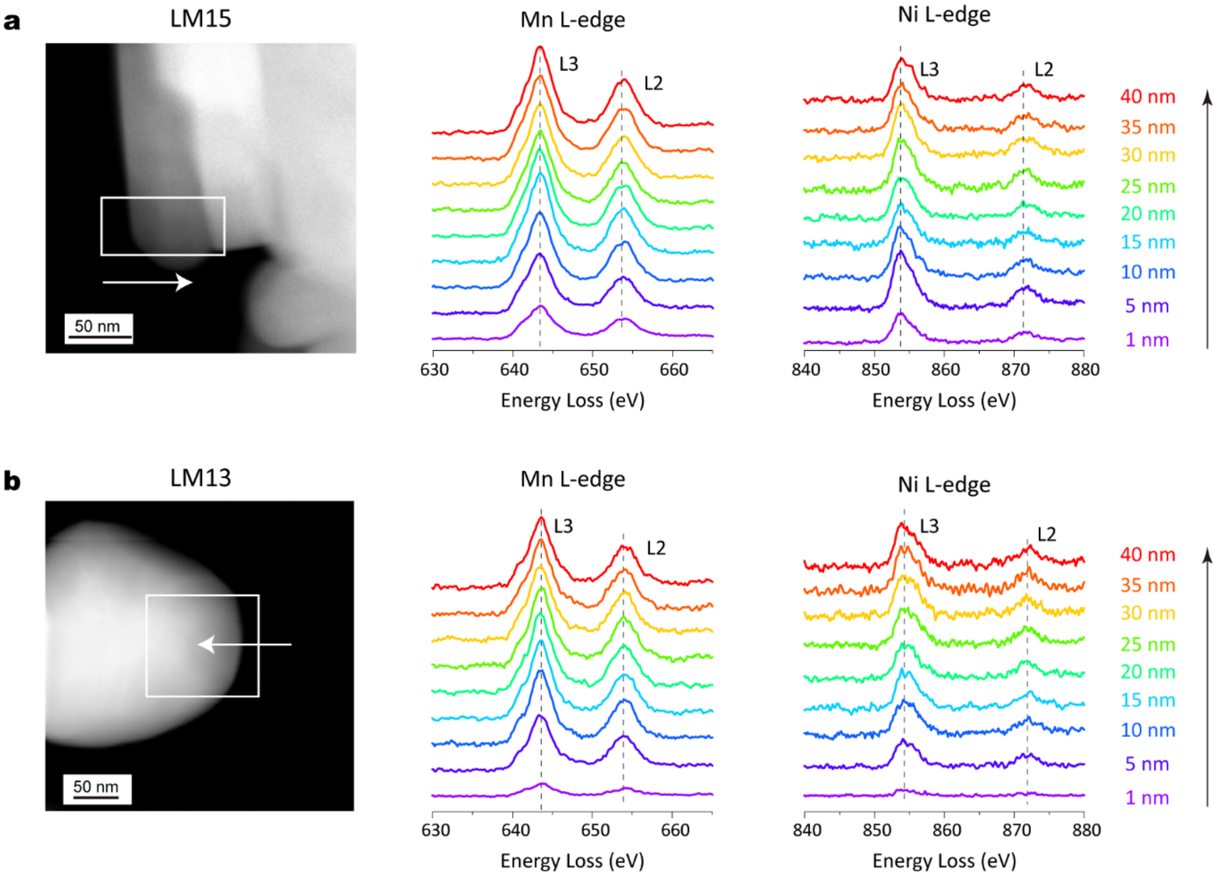

Figure A5 EELS line scans at particle surface in pristine LM15 (a) and LM13 (b).

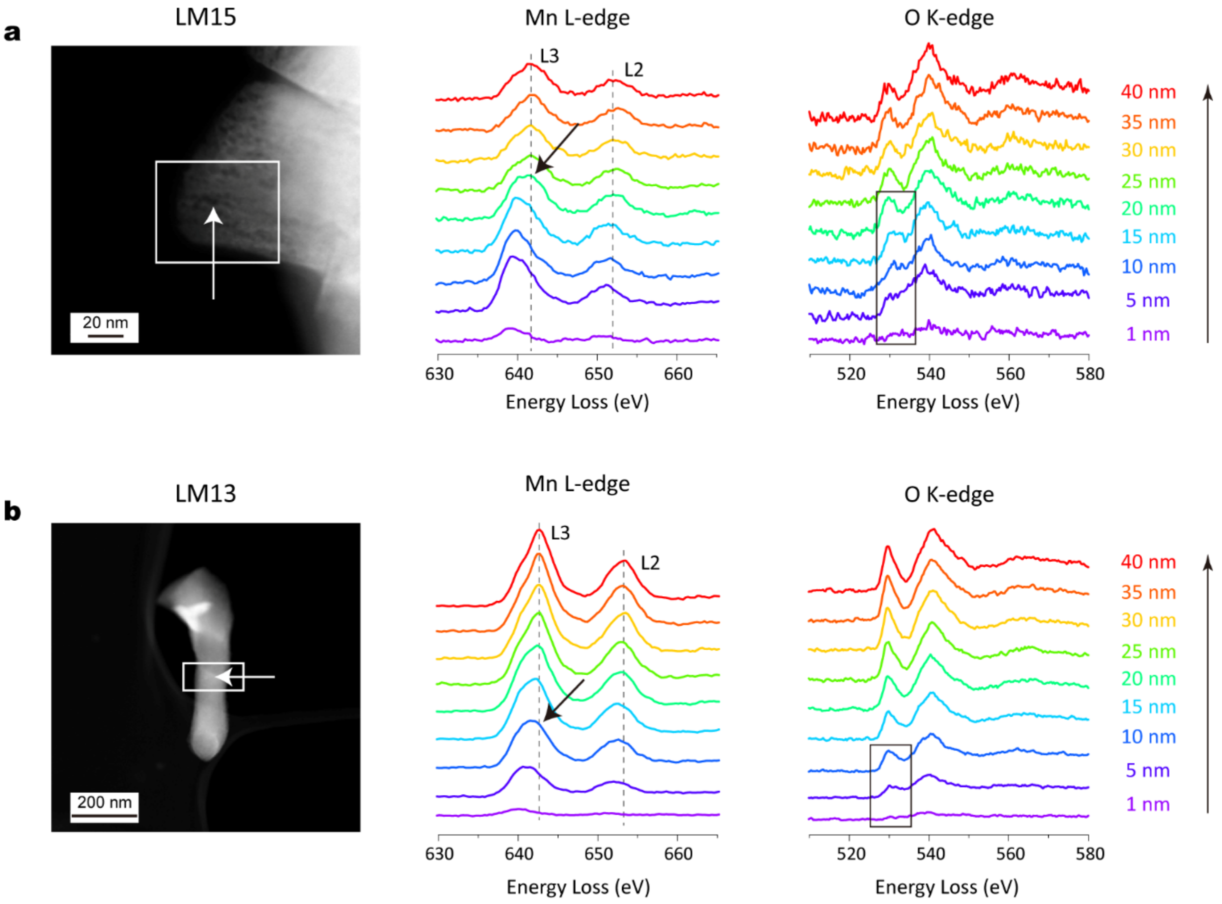

Figure A6 EELS line scans at particle surface LM15 (a) and LM13 (b) in the cycled electrode at C/3 after 200 cycles.

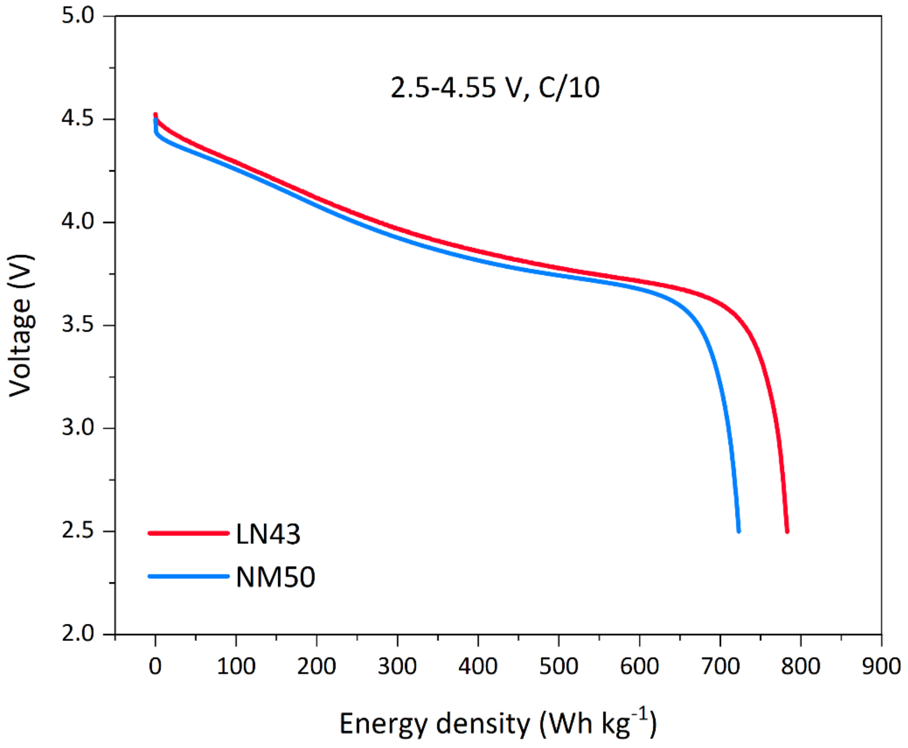

Figure A7 Energy density curves for both cathodes at C/10 within the voltage range of 2.5-4.55 V.

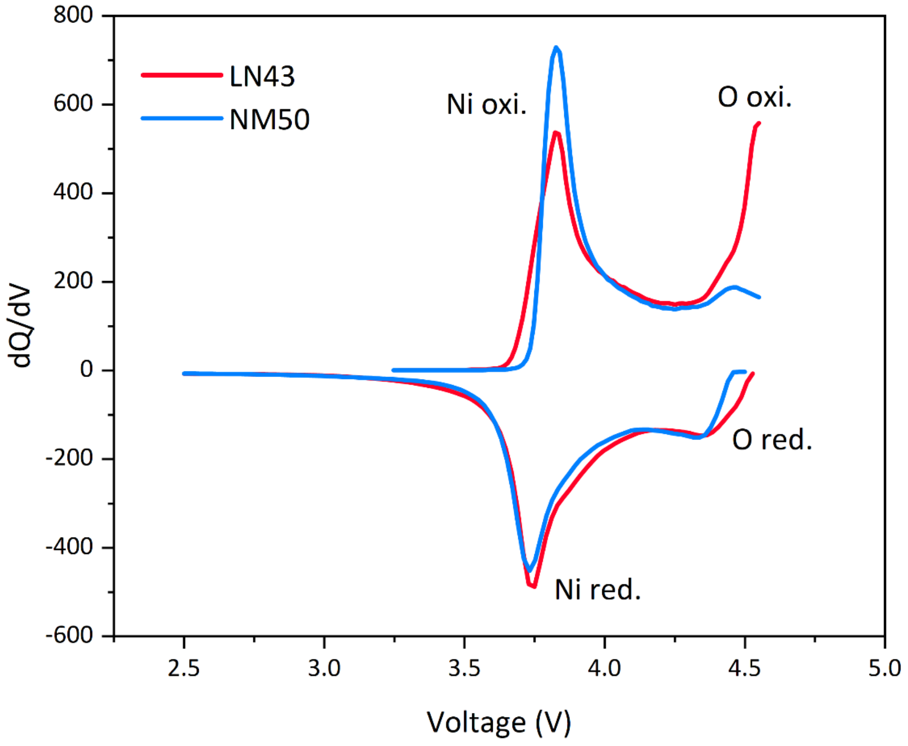

Figure A8 The dQ/dV curves for both cathodes at C/10 within the voltage range of 2.5-4.55 V.

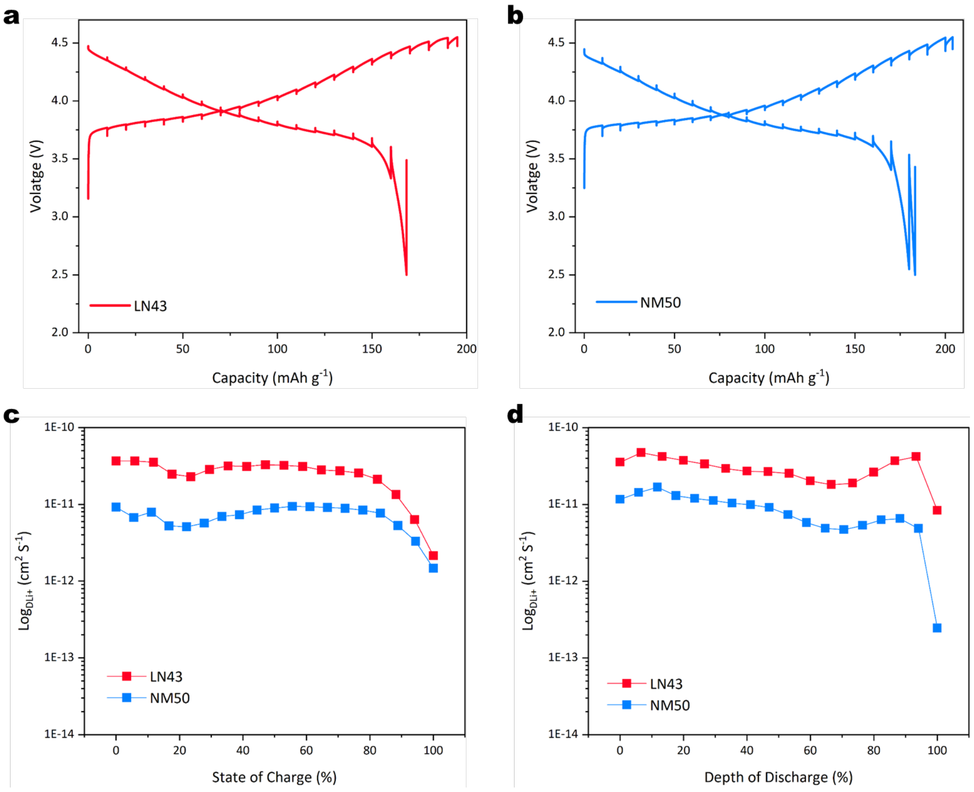

Figure A9 The GITT patterns and corresponding calculated Li$^+$ diffusion coefficient during charging/discharging for both cathodes.

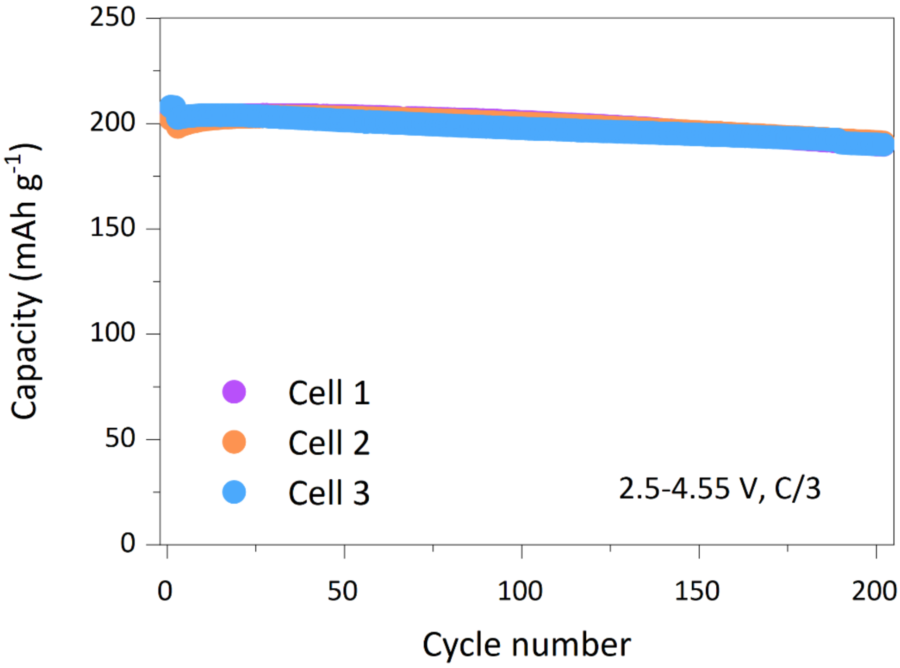

Figure A10 Repeated cycling performance of LN43 cathode over 200 cycles at C/3 within the voltage range of 2.5-4.55 V.

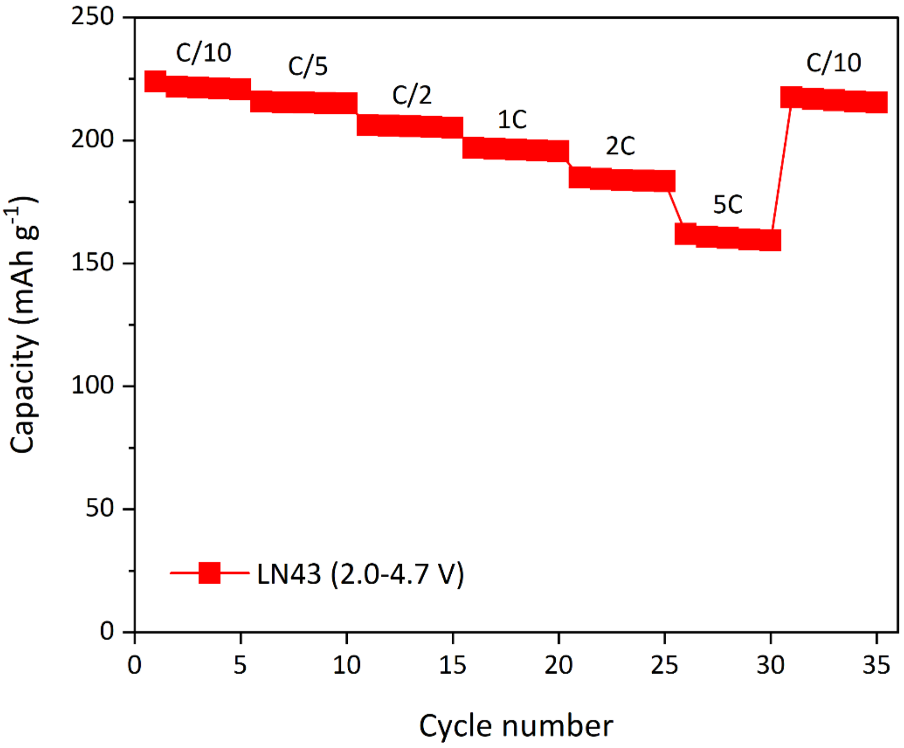

Figure A11 The rate capability test conducted from C/10 to 5C of LN43 cathode within the voltage range of 2.7-4.7 V.

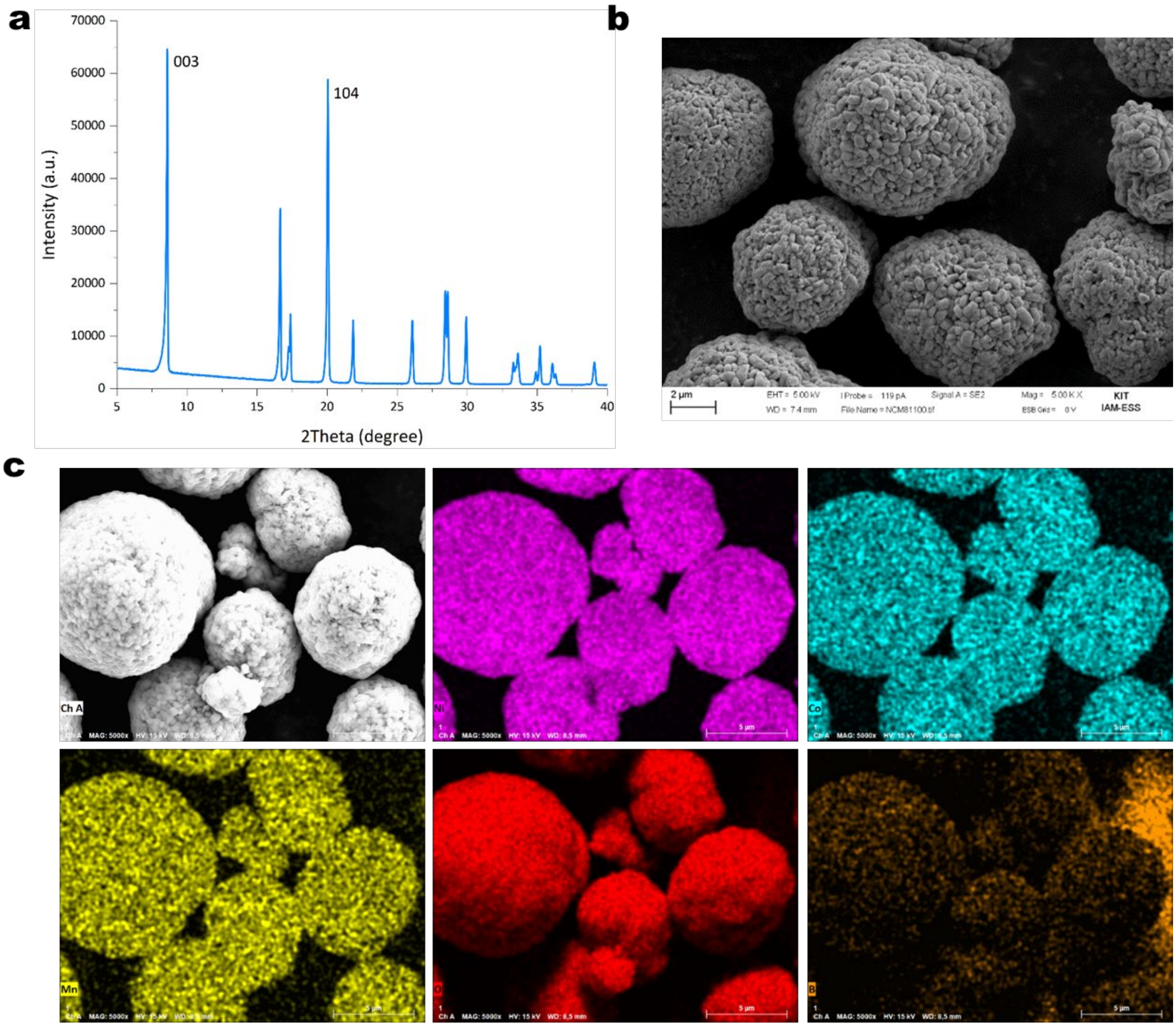

Figure A12 (a) XRD pattern for commercial NCM811 powder. (b) SEM images and (c) SEM mapping images of NCM811 powder. Boron was surface coated on NCM811 powder to lower the resistance and increase cycle life.

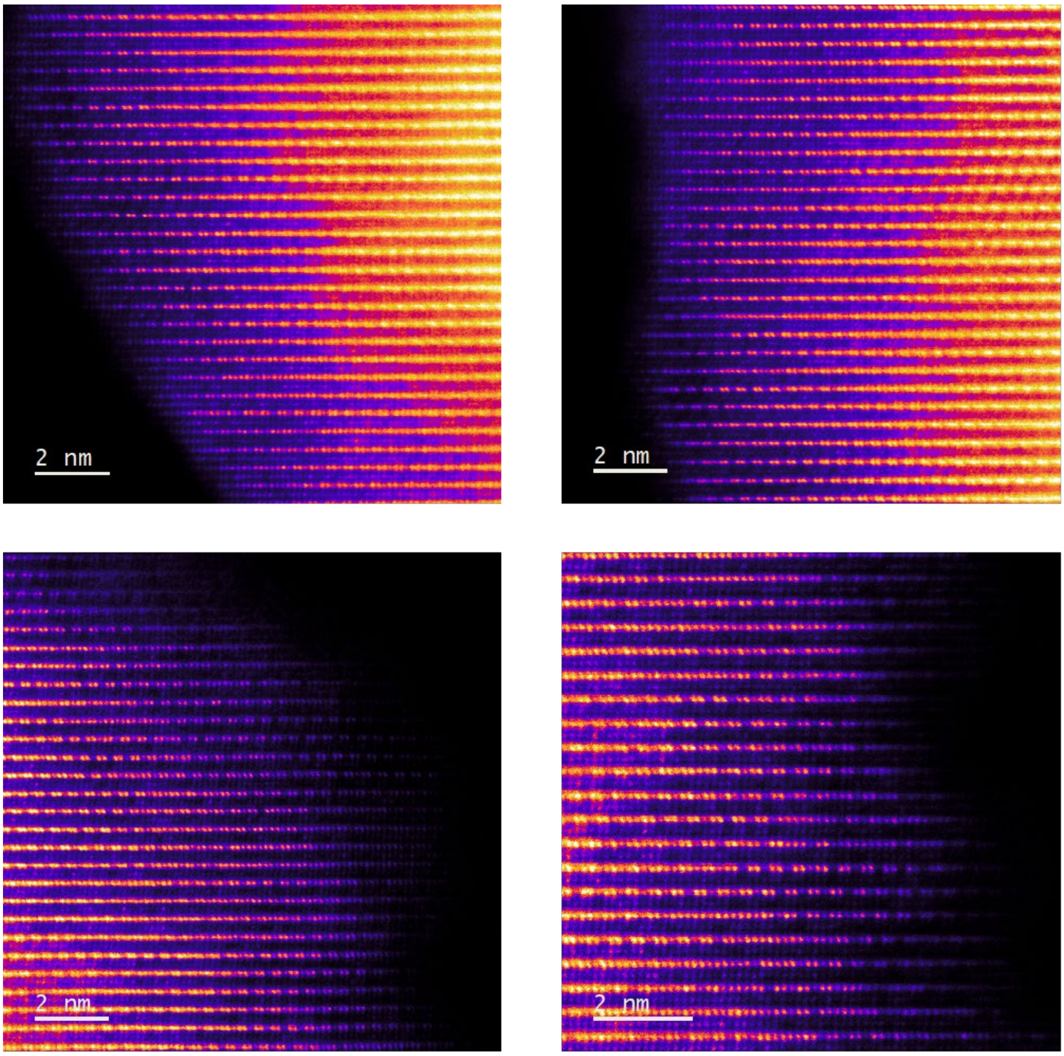

Figure A13 HAADF–STEM image along the [110] zone axis of LN43 cathode at different regions.

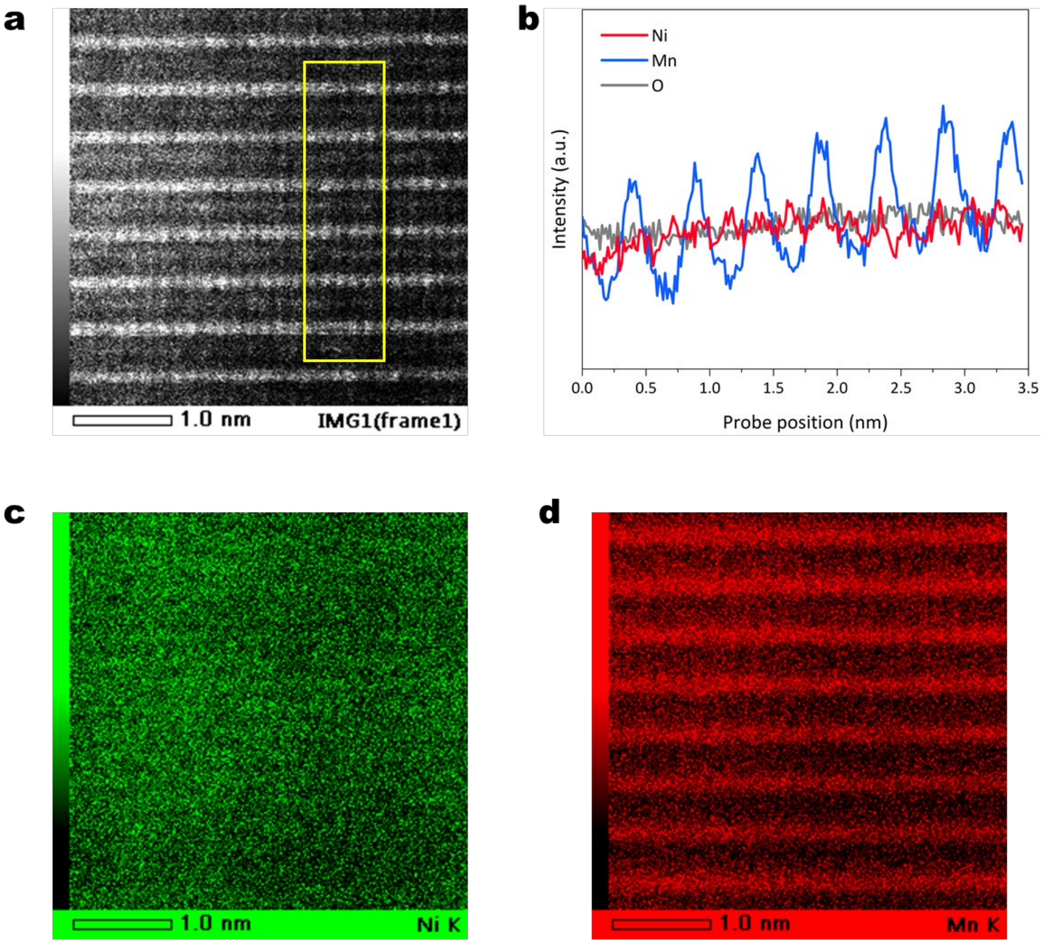

Figure A14 (a) HAADF–STEM image. (b) The corresponding line profile analysis and (c-d) atomic-scale EDX mappings of LN43 cathode.

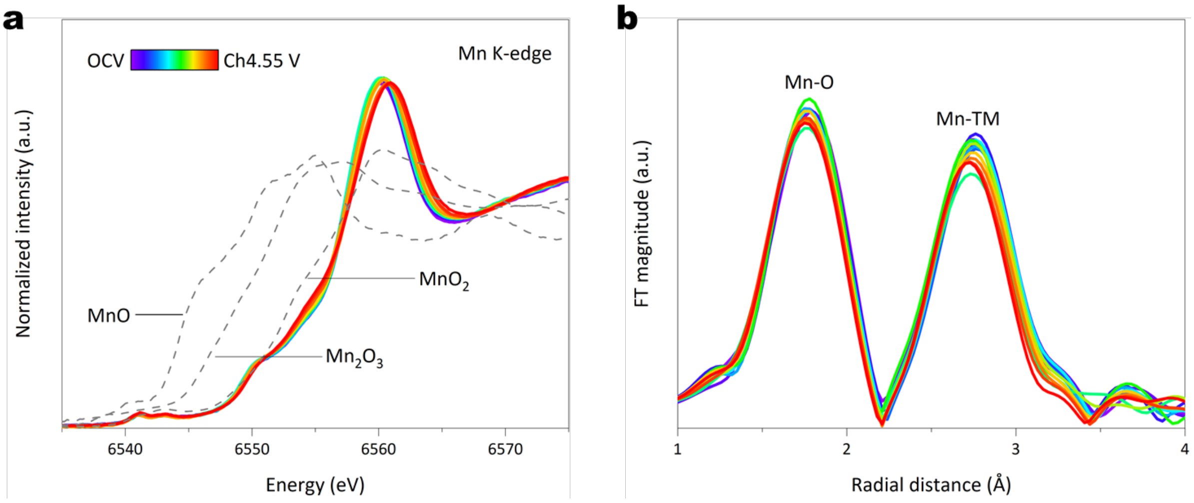

Figure A15 In-situ Mn K-edge XANES spectra (a) and corresponding FT-EXAFS spectra (b) during charging process at C/10 in the voltage range of 2.5-4.55 V at 25 °C.

Table A1 Crystallographic data of N28, N32, N36, and N40 obtained from Rietveld refinement of SXRD pattern.

Atom	Site	x	y	z	Occ
Li1/Ni1	3*b*	0	0	0.5	0.976(4)/0.024(4)
Li2/Ni2/Mn1	3*a*	0	0	0	0.224(4)/0.255(4)/0.520
O1	6*c*	0	0	0.2576(6)	1

$Li_{1.20}Ni_{0.28}Mn_{0.52}O_2$ (N28), Space group: *R-3m*
$a = b = 2.8598(1)$ Å, $c = 14.2362(14)$ Å
$R_{wp} = 1.78\%$, $R_p = 1.14\%$

Atom	Site	x	y	z	Occ
Li1/Ni1	3*b*	0	0	0.5	0.977(4)/0.023(4)
Li2/Ni2/Mn1	3*a*	0	0	0	0.223(4)/0.297(4)/0.480
O1	6*c*	0	0	0.2577(5)	1

$Li_{1.20}Ni_{0.32}Mn_{0.48}O_2$ (N32), Space group: *R-3m*
$a = b = 2.8602(1)$ Å, $c = 14.2345(9)$ Å
$R_{wp} = 2.00\%$, $R_p = 1.25\%$

Atom	Site	x	y	z	Occ
Li1/Ni1	3*b*	0	0	0.5	0.978(4)/0.022(4)
Li2/Ni2/Mn1	3*a*	0	0	0	0.222(4)/0.338(4)/0.440
O1	6*c*	0	0	0.2568(4)	1

$Li_{1.20}Ni_{0.36}Mn_{0.44}O_2$ (N36), Space group: *R-3m*
$a = b = 2.8611(1)$ Å, $c = 14.2300(8)$ Å
$R_{wp} = 2.44\%$, $R_p = 1.51\%$

Atom	Site	x	y	z	Occ
Li1/Ni1	3*b*	0	0	0.5	0.982(4)/0.018(4)
Li2/Ni2/Mn1	3*a*	0	0	0	0.218(3)/0.382(4)/0.400
O1	6*c*	0	0	0.2577(5)	1
$Li_{1.20}Ni_{0.40}Mn_{0.40}O_2$ (N40), Space group: *R-3m* $a = b = 2.8593(1)$ Å, $c = 14.2241(8)$ Å $R_{wp} = 2.11\%$, $R_p = 1.36\%$					

Table A2 ^{6}Li NMR fitting results for N28, N32, N36, and N40.

			N28			
Shift (ppm)	1.40	541.82	734.97	889.55	1330.58	1491.11
Area (%)	1.05	30.69	43.26	12.88	2.22	9.90

			N32			
Shift (ppm)	0.68	543.96	733.26	871.23	1316.23	1492.67
Area (%)	0.98	34.89	33.84	19.97	3.82	6.49

			N36			
Shift (ppm)	0.61	544.25	733.92	868.81	1306.3	1487.56
Area (%)	0.90	44.98	29.18	17.18	4.18	3.57

			N40			
Shift (ppm)	0.48	572.94	745.80	804.65	1304.38	1491.65
Area (%)	1.03	50.64	4.36	37.04	4.26	2.67

Table A3 Atomic coordinates of the INPUT for supercell (S.G.: P1) for the structure model development. The lattice parameters are a = 4.928 Å, b = 4.928 Å, c = 5.030 Å, α = 80.35°, β = 99.60° and γ = 60.11°. Based on this primitive cell a 3×2×2 supercell was built.

Atom	*x*	*Y*	*Z*	S.O.F
Mn1	0.167	0.167	0	0.5
Ni1	0.167	0.167	0	0.5
Mn2	-0.167	-0.167	0	0.5
Ni2	-0.167	-0.167	0	0.5
Li1	-0.5	-0.5	0.0	0.6
Mn3	-0.5	-0.5	0.0	0.4
Li2	0.0	0.0	0.5	1.0
Li3	0.34	0.34	0.5	1.0
Li4	-0.34	-0.34	0.5	1.0
O1	0.218	-0.218	0.227	1.0
O2	-0.218	0.218	-0.227	1.0
O3	-0.424	0.067	0.223	1.0
O4	0.067	-0.428	-0.223	1.0
O5	0.424	-0.067	-0.223	1.0
O6	-0.067	0.425	0.223	1.0

Table A4 Atomic coordinates of structure model ($Li_{44}Mn_{18}Ni_{10}O_{72}$, P1) after optimization with CRYSTAL17. The lattice parameters are a = 14.7077 Å, b = 9.8281 Å, c = 9.9263 Å, α = 80.67°, β = 99.44° and γ = 59.83°.

Atom	*x*	*y*	*z*
Li1	0.833154	0.749788	-0.000274
Li2	0.834210	0.745464	0.503517
Li3	0.833559	0.250052	-0.000407
Li4	0.833680	0.252563	0.497692
Li5	0.166770	0.750454	0.000146
Li6	0.166788	0.248908	-0.000227
Li7	0.499494	0.750013	0.000569
Li8	0.499828	0.249819	-0.000012
Li9	-0.004944	0.006427	0.245249
Li10	-0.000372	0.000792	0.747547
Li11	-0.003656	0.505299	0.246479

Li12	-0.000275	0.499319	0.748760
Li13	0.329497	0.007079	0.247461
Li14	0.337524	-0.005028	0.753369
Li15	0.331630	0.501406	0.251766
Li16	0.336444	0.494112	0.751160
Li17	0.665519	0.001507	0.249418
Li18	0.669461	-0.005897	0.752730
Li19	0.667222	0.501189	0.253557
Li20	0.669204	0.497519	0.750870
Li21	0.111020	0.172430	0.246076
Li22	0.110865	0.169348	0.755464
Li23	0.113288	0.667051	0.246529
Li24	0.111353	0.667347	0.753576
Li25	0.446299	0.165898	0.248652
Li26	0.445005	0.167877	0.750557
Li27	0.446590	0.666084	0.244472
Li28	0.446383	0.666304	0.750478
Li29	0.778746	0.172674	0.250492
Li30	0.780107	0.170799	0.751159
Li31	0.779423	0.668221	0.253774
Li32	0.781138	0.667404	0.746950
Li33	0.885919	0.828824	0.248989
Li34	0.886837	0.828317	0.749688
Li35	0.886924	0.330727	0.251009
Li36	0.885701	0.333606	0.748061
Li37	0.222215	0.829785	0.244661
Li38	0.220663	0.830310	0.755892
Li39	0.222670	0.331368	0.247913
Li40	0.219976	0.334699	0.749697
Li41	0.557157	0.828185	0.250856
Li42	0.553612	0.834527	0.752090
Li43	0.555229	0.332724	0.248072
Li44	0.553820	0.333478	0.752726
Mn1	0.167441	0.747949	0.501959
Mn2	0.166594	0.252433	0.496847
Mn3	0.500113	0.749925	0.500113
Mn4	0.499785	0.250024	0.500537

Mn5	0.056643	0.082318	-0.000762
Mn6	0.055365	0.583167	-0.000469
Mn7	0.388017	0.082030	0.000131
Mn8	0.388088	0.584985	-0.000116
Mn9	0.722346	0.083375	0.000677
Mn10	0.724801	0.081513	0.500683
Mn11	0.722380	0.583254	0.000487
Mn12	0.944451	0.916552	-0.000487
Mn13	0.942907	0.918872	0.500366
Mn14	0.944298	0.416422	-0.001179
Mn15	0.940969	0.417889	0.499620
Mn16	0.277936	0.416393	0.000136
Mn17	0.611293	0.916057	0.001018
Mn18	0.611176	0.416919	0.000526
Ni1	0.054162	0.084576	0.498094
Ni2	0.049995	0.587516	0.499579
Ni3	0.388777	0.084420	0.499717
Ni4	0.388239	0.582960	0.501192
Ni5	0.723708	0.581617	0.500723
Ni6	0.277645	0.916444	0.000138
Ni7	0.277191	0.918363	0.500357
Ni8	0.278764	0.415513	0.500127
Ni9	0.616530	0.910265	0.499843
Ni10	0.616063	0.414733	0.499762
O1	0.072712	0.891257	0.111929
O2	0.079160	0.872097	0.616200
O3	0.072528	0.391160	0.110958
O4	0.081299	0.371107	0.613913
O5	0.403697	0.891166	0.110455
O6	0.416212	0.868979	0.616243
O7	0.405849	0.392246	0.111460
O8	0.424597	0.363564	0.619951
O9	0.739840	0.890484	0.114493
O10	0.744894	0.887307	0.615546
O11	0.739888	0.390513	0.113872
O12	0.743465	0.390886	0.611291
O13	0.927590	0.108679	0.885239

O14	0.925769	0.110274	0.387976
O15	0.926885	0.609115	0.886472
O16	0.922893	0.612370	0.385314
O17	0.260112	0.105646	0.889491
O18	0.243348	0.133859	0.379733
O19	0.260184	0.608644	0.888255
O20	0.241878	0.637366	0.381055
O21	0.594349	0.108073	0.889410
O22	0.589231	0.123986	0.385829
O23	0.593818	0.608839	0.888678
O24	0.576776	0.631371	0.380579
O25	0.858574	0.034264	0.112768
O26	0.858620	0.034994	0.613629
O27	0.858616	0.533697	0.111666
O28	0.867965	0.527843	0.618591
O29	0.192441	0.033024	0.111192
O30	0.191401	0.047203	0.604588
O31	0.191507	0.534119	0.113122
O32	0.188404	0.555057	0.613367
O33	0.524534	0.033178	0.113805
O34	0.529422	0.048917	0.613724
O35	0.524825	0.534818	0.112709
O36	0.528148	0.550241	0.613642
O37	0.022942	0.786731	0.887490
O38	0.028416	0.796074	0.387191
O39	0.023524	0.285670	0.887140
O40	0.029624	0.296313	0.384158
O41	0.355025	0.789504	0.888995
O42	0.360841	0.800852	0.390610
O43	0.355498	0.286395	0.887098
O44	0.372326	0.288715	0.382135
O45	0.689638	0.786800	0.887912
O46	0.694433	0.778867	0.390839
O47	0.689761	0.286899	0.887383
O48	0.693885	0.282649	0.386429
O49	0.143871	0.963558	0.888104
O50	0.139454	0.952761	0.392112

O51	0.141730	0.464719	0.887199
O52	0.137913	0.450544	0.385761
O53	0.475188	0.965237	0.887125
O54	0.477668	0.945169	0.386236
O55	0.474533	0.467311	0.886723
O56	0.477894	0.445368	0.386933
O57	0.808429	0.965935	0.887674
O58	0.809153	0.965241	0.387165
O59	0.808192	0.465720	0.886874
O60	0.811744	0.461479	0.385037
O61	0.977979	0.211941	0.112454
O62	0.977982	0.209813	0.609229
O63	0.977058	0.713082	0.112741
O64	0.973702	0.716902	0.613296
O65	0.310460	0.212426	0.113015
O66	0.294563	0.210339	0.617713
O67	0.309732	0.715566	0.111895
O68	0.294065	0.713632	0.618235
O69	0.643479	0.213172	0.112524
O70	0.639486	0.204230	0.613290
O71	0.643825	0.712636	0.113110
O72	0.633203	0.708148	0.614206

Table A5 ICP–OES results for LM12, LM13, LM14, and LM15.

Sample	Li	Ni	Mn	Li/TM
LM12	0.960	0.360	0.440	1.200
LM13	1.028	0.360	0.440	1.285
LM14	1.105	0.360	0.440	1.381
LM15	1.161	0.361	0.439	1.451

Table A6 Crystallographic data of LM12, LM13, LM14, and LM15 obtained from Rietveld refinement of SXRD pattern.

Atom	Site	x	y	z	Occ
Li1/Ni1	3*b*	0	0	0.5	0.937(3)/0.063(3)

Li2/Ni2/Mn1	3*a*	0	0	0	0.153(3)/0.348(3)/0.500
O1	6*c*	0	0	0.2576(6)	1

$Li_{1.09}Ni_{0.41}Mn_{0.50}O_2$ (LM12), Space group: *R-3m*
a = *b* = 2.8787(1) Å, *c* = 14.2659(15) Å
R_{wp} = 4.02%, R_p = 2.11%

Atom	Site	x	y	z	Occ
Li1/Ni1	3*b*	0	0	0.5	0.954(6)/0.046(6)
Li2/Ni2/Mn1	3*a*	0	0	0	0.176(6)/0.344(6)/0.480
O1	6*c*	0	0	0.2574(11)	1

$Li_{1.13}Ni_{0.39}Mn_{0.48}O_2$ (LM13), Space group: *R-3m*
a = *b* = 2.8717(2) Å, *c* = 14.2519(24) Å
R_{wp} = 2.70%, R_p = 1.84%

Atom	Site	x	y	z	Occ
Li1/Ni1	3*b*	0	0	0.5	0.960(6)/0.040(6)
Li2/Ni2/Mn1	3*a*	0	0	0	0.210(6)/0.330(6)/0.460
O1	6*c*	0	0	0.2576(5)	1

$Li_{1.17}Ni_{0.37}Mn_{0.46}O_2$ (LM14), Space group: *R-3m*
a = *b* = 2.8649(1) Å, *c* = 14.2398(8) Å
R_{wp} = 3.75%, R_p = 1.94%

Atom	Site	x	y	z	Occ
Li1/Ni1	3*b*	0	0	0.5	0.982(4)/0.018(4)
Li2/Ni2/Mn1	3*a*	0	0	0	0.218(3)/0.382(4)/0.400
O1	6*c*	0	0	0.2577(5)	1

$Li_{1.20}Ni_{0.40}Mn_{0.40}O_2$ (LM15), Space group: *R-3m*
a = *b* = 2.8593(1) Å, *c* = 14.2241(8) Å
R_{wp} = 2.11%, R_p = 1.36%

Table A7 ^{6}Li NMR fitting results for LM13 and LM15.

			LM13			
Shift (ppm)	0.96	577.16	730.15	834.87	1332.84	1495.76
Area (%)	0.74	50.74	6.75	32.19	4.09	5.48

			LM15			
Shift (ppm)	0.62	566.71	737.76	802.65	1303.91	1488.68
Area (%)	0.96	49.48	6.49	34.28	5.11	3.67

Table A8 Table of ICP–OES results for LN43.

Sample	Li	Ni	Mn	Li/TM
LN43	1.07713	0.43949	0.54009	1.09958

Table A9 Crystallographic data of LN43 obtained from joint refinement of SXRD and NPD pattern.

R_{wp} = 0.49%, R_p = 0.80% for SXRD; R_{wp} = 5.84%, R_p = 4.35% for NPD					
Space group: *R-3m*, *a* = *b* = 2.8933(1) Å, *c* = 14.2934(8) Å, 87.2(4)% phase fractions					
Atom	Site	x	y	z	Occ
Li1	3*b*	0	0	0.5	0.889(0)
Ni1	3*b*	0	0	0.5	0.111(0)
Li2	3*a*	0	0	0	0.111(0)
Ni2	3*a*	0	0	0	0.389(0)
Mn1	3*a*	0	0	0	0.5
O1	6*c*	0	0	0.2575(6)	1

Space group: *C2/m*, *a* = 4.9928(8) Å, *b* = 8.6146(8) Å, *c* = 5.0459(4) Å, 12.7(6)% phase fractions					
Atom	Site	x	y	z	Occ

Li1	2*b*	0	0.5	0	0.335(8)
Mn1	2*b*	0	0.5	0	0.665(8)
Li2	2*c*	0	0	0.5	0.941(5)
Ni1	2*c*	0	0	0.5	0.059(5)
Li3	4*h*	0	0.6984(42)	0.5	0.937(6)
Ni2	4*h*	0	0.6984(42)	0.5	0.063(6)
Mn2	4*g*	0	0.1686(17)	0	1
O1	4*i*	0.2355(89)	0	0.2282(88)	1
O2	8*j*	0.2198(53)	0.3345(2)	0.2281(46)	1

Table A10 ^{6}Li NMR fitting results for LN43.

LN43						
Shift (ppm)	0.42	585.75	736.59	888.80	1366.40	1512.68
Area (%)	0.89	58.07	15.07	17.36	0.28	8.33

Publications

1. **Hao Liu**, Weibo Hua, Sylvia Kunz, Matteo Bianchini, Hang Li, Jiali Peng, Jing Lin, Oleksandr Dolotko, Thomas Bergfeldt, Kai Wang, Christian Kübel, Peter Nagel, Stefan Schuppler, Michael Merz, Bixian Ying, Karin Kleiner, Stefan Mangold, Deniz Wong, Volodymyr Baran, Michael Knapp, Helmut Ehrenberg, and Sylvio Indris. Tailoring superstructure units for improved oxygen redox activity in Li-rich layered oxide battery's positive electrodes. ***Nature Communications***, 2024, 15(1): 1-14.

2. Xiaoxia Yang, Kai Wang, Jilu Zhang, Hang Li, **Hao Liu**, Tian Zhao, Xinyue Zhai, Qin Wang, Chengjun Fan, Martin Etter, Sylvio Indris, Weibo Hua, Xiaoping Ouyang. Modulating Local Oxygen Coordination to Achieve Highly Reversible Anionic Redox and Negligible Voltage Decay in O2-Type Layered Cathodes for Li-Ion Batteries. ***Advanced Energy Materials***, 2404276.

3. Jiali Peng, Angelina Sarapulova, Qiang Fu, Hang Li, **Hao Liu**, Oleksandr Dolotko, Thomas Bergfeldt, Karin Kleiner, Bixian Ying, Yi Wu, Volodymyr Baran, Edmund Welter, Peter Nagel, Stefan Schuppler, Michael Merz, Michael Knapp, Helmut Ehrenberg, Sylvio Indris. Understanding the Electrochemical Reaction Mechanism of the Co/Ni Free Layered Cathode Material P2–$Na_{2/3}Mn_{7/12}Fe_{1/3}Ti_{1/12}O_2$ for Sodium-Ion Batteries. ***Chemistry of Materials***, 2024, 36, 4107-4120.

4. Shenyang Xu, Zhefeng Chen, Wenguang Zhao, Wenju Ren, Chenxin Hou, Jiajie Liu, Wu Wang, Chong Yin, Xinghua Tan, Xiaobing Lou, Xiangming Yao, Zhihai Gao, **Hao Liu**, Lu Wang, Zuwei Yin, Bao Qiu, Bingwen Hu, Tianyi Li, Cheng Dong, Feng Pan, Mingjian Zhang. Multi-Angle Tracking Synthetic Kinetics of Phase Evolution in Li-Rich Mn-Based Cathodes. ***Energy & Environmental Science***, 2024,17, 3807-3818.

5. Zhuangzhi Li, Lang Qiu, Ping Li, **Hao Liu**, Dong Wang, Weibo Hua, Ting Chen, Yang Song, Fang Wan, Benhe Zhong, Zhenguo Wu. Exposing the (002) active facet by reducing surface energy for a high-performance $Na_3V_2(PO_4)_2F_3$ cathode. ***Journal of Materials Chemistry A***, 2024, 12, 7777-7787.

6. Weibo Hua, Jilu Zhang, Suning Wang, Yi Cheng, Hang Li, Jochi Tseng, Zhonghua Wu, Chong-Heng Shen, Oleksandr Dolotko, **Hao Liu**, Sung-Fu Hung, Wei Tang, Mingtao Li, Michael Knapp, Helmut Ehrenberg, Sylvio Indris, Xiaodong Guo. Long-Range Cationic Disordering Induces two Distinct Degradation Pathways in Co-Free Ni-Rich Layered Cathodes. ***Angewandte Chemie***, 2023, 135(12): e202214880.

7. **Hao Liu**, Ruikai Yang, Wen Yang, Changjiang Bai, Yong-Chun Li, Gongke Wang, Yuxia Liu, Wei Xiang, Zhenguo Wu, Xiaodong Guo. Suppressing capacity fading and voltage decay of Ni-rich cathode material by dual-ion doping for lithium-ion batteries. ***Journal of materials science***, 2021, 56, 2347-2359.

8. Rong Li, Chang-Jiang Bai, **Hao Liu**, Li-Wen Yang, Yong Ming, Chun-Liu Xu, Zhou Wei, Yang Song, Gong-Ke Wang, Yu-Xia Liu, Ben-He Zhong, Yan-Jun Zhong, Zhen-Guo Wu, Xiao-Dong Guo. New insights into the mechanism of enhanced performance of $Li[Ni_{0.8}Co_{0.1}Mn_{0.1}]O_2$ with a polyacrylic acid-modified binder. ***ACS Applied Materials & Interfaces***, 2021, 13, 10064-10070.

9. **Hao Liu**, Wei Xiang, Changjiang Bai, Lang Qiu, Chen Wu, Gongke Wang, Yuxia Liu, Yang Song, Zhen-Guo Wu, Xiaodong Guo. Enabling superior electrochemical performance of lithium-rich $Li_{1.2}Ni_{0.2}Mn_{0.6}O_2$ cathode materials by surface integration. ***Industrial & Engineering Chemistry Research***, 2020, 59, 19312-19321.

10. **Hao Liu**, Bin He, Wei Xiang, Yong-Chun Li, Changjiang Bai, Yong-Peng Liu, Wei Zhou, Xianchun Chen, Yuxia Liu, Shuyan Gao, Xiaodong Guo. Synergistic effect of uniform lattice cation/anion doping to improve structural and electrochemical performance stability for Li-rich cathode materials. ***Nanotechnology***, 2020, 31, 455704.

11. Weibo Hua, Kai Wang, Michael Knapp, Björn Schwarz, Suning Wang, **Hao Liu**, Jing Lai, Marcus Müller, Alexander Schökel, Alexander Missyul, Dario Ferreira Sanchez, Xiaodong Guo, Joachim R. Binder, Jie Xiong, Sylvio Indris, Helmut Ehrenberg. Chemical and structural evolution during the synthesis of layered $Li(Ni,Co,Mn)O_2$ oxides. ***Chemistry of materials***, 2020, 32, 4984-4997.

12. Yongpeng Liu, Bin He, Qian Li, **Hao Liu**, Lang Qiu, Jie Liu, Wei Xiang, Yuxia Liu, Gongke Wang, Zhenguo Wu, Xiaodong Guo. Relieving capacity decay and voltage fading of $Li_{1.2}Ni_{0.13}Co_{0.13}Mn_{0.54}O_2$ by Mg^{2+} and PO_4^{3-} dual doping. ***Materials Research Bulletin,*** 2020, 130, 110923.

13. Dong Wang, Yihua Liu, Zhenguo Wu, Xiaohong Liu, Jie Qu, **Hao Liu**, Yong Ming, Yanjun Zhong, Benhe Zhong, Xiaodong Guo. A novel Mn-based P2/tunnel/O3' tri-phase composite cathode with enhanced sodium storage properties. ***Chemical Communications***, 2020, 56, 2921-2924.

Acknowledgements

I officially began my PhD work at the Department of Chemistry and Biosciences at the Karlsruhe Institute of Technology (KIT), specifically within the Institute for Applied Materials - Energy Storage Systems (IAM-ESS), in September 2021. I would like to express my sincere gratitude for the financial support provided by the China Scholarship Council (CSC, No. 202106240017). Additionally, I extend my heartfelt thanks to all those who have offered me assistance and encouragement throughout this journey.

Firstly, I am grateful to my supervisor Prof. Dr. Helmut Ehrenberg, who gave me the opportunity to work in IAM-ESS, for his great support, valuable guidance and thoughtful comments.

Secondly, I would like to express my sincere gratitude to my co-supervisor, Dr. Sylvio Indris, for his understanding, encouragement, and support throughout my studies at the KIT. He fostered a positive and stress-free research environment that allowed me to explore my research interests fully and to engage deeply with the topics I am passionate about. I feel fortunate to have had the opportunity to work with him, and the memories of this collaboration will be truly unforgettable. I am also grateful to Dr. Michael Knapp, Dr. Oleksandr Dolotko, Dr. Weibo Hua, and Dr. Holger Geßwein for their help on XRD/NPD data analysing; Dr. Anna-Lena Hansen and Dr. Ramon Zimmermanns for their help on PDF measurements and data analysing; Dr. Hang Li for NMR measurements and data fitting. I am also grateful to Dr. Valeriu Mereacre and Liuda Mereacre for providing support in the lab.

I am grateful the help from my colleagues at IAM-ESS, Dr. Qiang Fu, Dr. Xinyang Liu-Theato, Dr. Xianlin Luo, Dr. Tianzhu Liu, Dr. Jiali Peng, Bijian Deng, Kun Tang, Shuaiwei Liu, Xinyue Zhang, Liwen Yang, Yiran Guo, Cedric Müller, Felix Bauer, Marius Ast, Mrs. Almut Kriese (administrative support), Mr. Heinz-Robert Goebel (equipment support), Mr. Luis Martin Sanchez Neudeck (IT support), Mr. Philip Richter (purchase support). I would like to thank Dr. Volodymyr Baran (P02.1 beamline at PETRA III, Hamburg) and Dr. Aleksandr Missiul (MSPD beamline at ALBA, Barcelona) for SXRD experiments; Dr. Stefan Mangold (XAS beamline at KIT, Karlsruhe) and Dr. Wolfgang Caliebe (P64 beamline at PETRA III, Hamburg) for XAS measurements; Dr. Deniz Wong (PEAXIS beamline at BESSY, Berlin) for RIXS measurements; Dr. Peter Nagel and Dr. Stefan Schuppler (SXAS beamline at KIT, Karlsruhe) for SXAS measurements; Dr. Sylvia Kunz, Prof. Dr. Matteo Bianchini, and Hengyue Xu for DFT calculations; Dr. Thomas Bergfeldt for ICP–OES measurements; Jing Lin for PDF, NPD, XAS measurements; Hang Xu for DEMS measurements; Dr. Kai Wang, Prof. Dr. Christian Kübel, Dr. Yongjian Li, and Dr. Ning Li for STEM measurements; Dr. Björn Schwarz for magnetic measurements.

Finally, I would like to express my deep gratitude to my parents for their consistent support and understanding during my years of study abroad. Their love has brought me joy and given me the confidence to confront challenges fearlessly. I wish them lasting happiness and good health. I would also like to express my heartfelt gratitude to my dear wife, Lei Zeng. Despite the physical distance between us, you have provided me with unwavering understanding, supported me through difficult times, and inspired me to persevere. May our love remain ever youthful.

Declaration

Ich versichere hiermit, dass ich die vorliegende Dissertation selbständig und ohne unzulässige fremde Hilfe erbracht habe. Ich habe keine anderen als die angegeben Quellen und Hilfsmittel benutzt, sowie wörtliche und sinngemäße Zitate kenntlich gemacht. Die Dissertation wurde bisher an keiner anderen Hochschule oder Universität eingereicht.

Karlsruhe, den 25.10.2024

M. Sc. Hao Liu

I hereby declare that I have made this work independently and used no other than the specified sources and tools, as well as, whether verbatim or with regards to content, indicated all citations as such and I have paid attention to the statute of the Karlsruhe Institute of Technology (KIT) in the current version to ensure good scientific practice.

Karlsruhe, 25.10.2024

M. Sc. Hao Liu